Small Scale Maximum Power Point Tracking Power Converter for Developing Country Application

Parash Acharya

A thesis submitted in partial fulfilment
of the requirements for the degree of
Master of Engineering
in
Electrical and Computer Engineering
at the
University of Canterbury,
Christchurch, New Zealand.

2013

ABSTRACT

This thesis begins with providing a basic introduction of electricity requirements for small developing country communities serviced by small scale generating units (focussing mainly on small wind turbine, small Photo Voltaic system and Micro-Hydro Power Plants). Scenarios of these small scale units around the world are presented. Companies manufacturing different size wind turbines are surveyed in order to propose a design that suits the most abundantly available and affordable turbines.

Different Maximum Power Point Tracking (MPPT) algorithms normally employed for these small scale generating units are listed along with their working principles. Most of these algorithms for MPPT do not require any mechanical sensors in order to sense the control parameters like wind speed and rotor speed (for small wind turbines), temperature and irradiation (for PV systems), and water flow and water head (for Micro-Hydro). Models for all three of these systems were developed in order to generate Maximum Power Point (MPP) curves. Similarly, a model for Permanent Magnet Synchronous Generators (PMSGs) has been developed in the d-q reference frame. A boost rectifier which enables active Power Factor Correction (PFC) and has a DC regulated output voltage is proposed before implementing a MPPT algorithm. The proposed boost rectifier works on the principle of Direct Power Control Space Vector Modulation (DPC-SVM) which is based on instantaneous active and reactive power control loops. In this technique, the switching states are determined according to the errors between commanded and estimated values of active and reactive powers.

The PMSG and Wind Turbine behaviour are simulated at various wind speeds. Similarly, simulation of the proposed PFC boost rectifier is performed in matlab/simulink. The output of these models are observed for the variable wind speeds which identifies PFC and boosted constant DC output voltage is obtained. A buck converter that employs the MPPT algorithm is proposed and modeled. The model of a complete system that consists of a variable speed small wind turbine, PMSG, DPC-SVM boost rectifier, and buck converter implementing MPPT algorithm is developed. The proposed MPPT algorithm is based upon the principle of adjusting the duty ratio of the buck converter in order reach the MPP for different wind speeds (for small wind

turbines) and different water flow rates (Micro-Hydro).

Finally, a prototype DPC-SVM boost rectifier and buck converter was designed and built for a turbine with an output power ranging from 50 W-1 kW. Inductors for the boost rectifier and buck DC-DC converter were designed and built for these output power ranges. A microcontroller was programmed in order to generate three switching signals for the PFC boost rectifier and one switching signal for the MPPT buck converter. Three phase voltages and currents were sensed to determine active and reactive power. The voltage vectors were divided into 12 sectors and a switching algorithm based on the DPC-SVM boost rectifier model was implemented in order to minimize the errors between commanded and estimated values of active and reactive power.

The system was designed for charging 48 V battery bank. The generator three phase voltage is boosted to a constant 80 V DC. Simulation results of the DPC-SVM based rectifier shows that the output power could be varied by varying the DC load maintaining UPF and constant boosted DC voltage. A buck DC-DC converter is proposed after the boost rectifier stage in order to charge the 48 V battery bank. Duty ratio of the buck converter is varied for varying the output power in order to reach the MPP. The controller prototype was designed and developed. A laboratory setup connecting 4 kW induction motor (behaving as a wind turbine) with 1kW PMSG was built. Speed-torque characteristic of the induction motor is initially determined. The torque out of the motor varies with the motor speed at various motor supply voltages. At a particular supply voltage, the motor torque reaches peak power at a certain turbine speed. Hence, the control algorithm is tested to reach this power point. Although the prototype of the entire system was built, complete results were not obtained due to various time constraints. Results from the boost rectifier showed that the appropriate switching were performed according to the digitized signals of the active and reactive power errors for different voltage sectors.
Simulation results showed that for various wind speed, a constant DC voltage of 80 V DC is achieved along with UPF. MPPT control algorithm was tested for induction motor and PMSG combination. Results showed that the MPPT could be achieved by varying the buck converter duty ratio with UPF achieved at various wind speeds.

PUBLICATION

A paper entitled"Direct Power Control Space Vector Modulation Technique Suitable for small Wind Turbines" has been sent for the review in the conference " 5th International Conference on Power and Energy Systems Advances in Power Systems October 28 - 30, 2013, Kathmandu, Nepal" as a outcome of this thesis.

ACKNOWLEDGEMENTS

There are many people around, who were of great help throughout my thesis. Without all of your help and support my thesis would not have been completed. I thank you all with my deepest gratitude.

A special thanks to my supervisor Paul Gaynor, all your support, knowledge and guidance was really invaluable. I would like to acknowledge Professor Pat Bodger for including me in the Solar project in Tonga during my second year of studies. This was a great experience which I will cherish throughout my life. A huge thanks to all technical staff especially David Healy for helping me to build the test rig, Ken Smart for letting me use the space in machines lab and lending me all the equipment throughout my tests, Philip Hoff for advice on microcontroller programming, Nick Smith for etching my PCBs and offering advice on good PCB design, Jac Woudberg for taking care of all the component orders and Edsel Villa for the help in the Power Electronics Lab.

I would like to take an opportunity to thank two special friends of mine Lance Frater and Blair Bonnett who were very supportive when I was doing my experiments. A big thanks to all my other Postgraduate friends especially Shreejan Pandey, Dr. Andrew Lapthorn, Bhabha Das, Michael Hwang, Kalyan Malla, Alejandro Castellanos Escamilla, Yanosh Irani and Rabia Nazir.

I am really grateful to New Zealand Aid for their scholarship which funded not only my studies but also my stay in New Zealand. I would like to thank all my Nepalese friends from Nepal New Zealand Friendship Society who never let me miss my friends and family back in home.

Finally, I would like to thank my wife Nisha Gyawali and family back in Nepal especially Mom and Dad. Thank you for all your love, care and especially believing on me.

CONTENTS

LIST OF FIGURES

LIST OF TABLES

GLOSSARY

NOMENCLATURE

ω_{ropt}	Optimum rotor speed
$\triangle\omega$	change in generator speed
$\triangle p$	change in output power
V_{dc}	dc output voltage
T_{opt}	dc Optimum torque out of the wind turbine
T_t	Actual torque out of the wind turbine
$\triangle T$	Error between an optimal and measured torque
T-ω	Torque-speed
V_{dcref}	reference dc output voltage
$\frac{dp}{dV_{dc}}$	Change in power with respect to change in output dc voltage
P(k)	Power at k sampling time
K_t	Reference for the change in rotor speed
$\triangle P(k)$	Change in power in k sampling time
V_b	Battery voltage
V_{th}	Battery threshold voltage
I_{avg}	Average inductor current
f	Switching frequency
L	Inductance
d_1	Charging period of an inductor
D	dc/dc converter duty cycle
V_{MPP}	Maximum power point voltage
I_{MPP}	Maximum power point current
V_{PV}	PV array voltage
I_{PV}	PV array current
E	Error
$\triangle E$	PV array voltage
$\triangle D$	Change in duty ratio

c_p	Power coefficient of wind turbine
λ	Blade tip speed ratio
β	Blade pitch angle
ρ_a	Density of air
V_w	Wind Velocity
V_{tip}	Speed of the blade tip
J	System inertia
F	Viscous friction
T_m	Torque developed by the turbine
T_L	Torque due to load
P_{hyd}	Power available from a hydraulic turbine
ρ_w	Specific density of water
A_w	Area swept by the wind turbine rotor blades
Q	Water flow rate
H	water net head
η_h	Hydraulic turbine efficiency
g	Gravitational acceleration
P_m	Mechanical power
F_d	d axis quantities
F_q	q axis quantities
F_a, F_b and F_c	a, b and c phase quantities
v_{ds}	d axis stator voltage
v_{qs}	q axis stator voltage
i_{ds}	d axis stator current
i_{qs}	q axis stator current
L_d	stator d axis self inductance
L_q	stator q axis self inductance
L_{dm}	stator d axis magnetizing inductance
L_{qm}	stator q axis magnetizing inductance
L_{ls}	stator leakage inductance
T_e	Electromagnetic Torque
N_{pp}	Number of generator pole pairs
I_{pc}	Photocurrent of the PV module
I_D	Diode current of the PV module
I_0	Diode saturation current of PV module
V_T	Terminal potential of a module
n	Ideal constant of a diode
k	Boltzmann's constant
q	Electric charge magnitude of the electron

m	Number of PV cells connected in series
μ	Solar Insolation
K_i	Cell's short-circuit temperature coefficient of PV cell
I_{RS}	PV cell's reverse saturation current
E_G	Band-gap energy of the semicondutor used in the PV cell
A_{PV}	Ideal factor dependent on the PV technology
N_p	PV array module connected in parallel
N_s	PV array module connected in series
I_q	Quadrature component of I
I_a, I_b, I_c	Three phase line currents
P_{ref}	Active power reference of I
Q_{ref}	Reactive power reference
I_q	Quadrature component of I
P	Instantaneous active power
Q	Instantaneous reactive power
E_α, E_β	Two phase stationary voltage representation of three phase voltages
I_α, I_β	Two phase stationary current representation of three phase currents
E_a, E_b, E_c	Three phase voltages from generator
E_{ab}, E_{bc}, E_{ca}	Line voltages from generator
S_a, S_b, S_c	Switching states of each phase of three phase rectifier
L	Line Inductance of three phase rectifier
V_{DC}	DC bus voltage
d_P	digitized output signal of active power
d_Q	digitized output signal of reactive power
H_P	Hysteresis control band of active power
H_Q	Hysteresis control band of reactive power
D_k	Duty cycle of buck converter at k iteration
ω_e	Generator phase voltage angular speed
I_P	Maximum primary current of LEM current transducer
I_{PN}	Nominal primary current of LEM current transducer
C_G	MOSFET gate capacitance
V_{DD}	Supply voltage of MOSFET driver
I_{QH}	Quiescent current of the driver with the input in the high state
I_{QL}	Quiescent current of the driver with the input in the low state
CC	Crossover constant
A_c	Area of the inductor core
W_a	Window area of the inductor core
K_u	Fraction area filled by copper inside inductor core
K_g	Core geometry

μ_e	Magnetic permiability of core material
MLT	Magnetic path length
μ_0	Magnetic permiability of air
B_{pk}	Peak flux density
R_c	Magnetic core reluctance
R_g	Air gap Reluctance
R_t	Total magnetic reluctance
g	Air gap between two cores
δ	Skin depth
W_d	Copper wire diameter

ABBREVIATIONS

LED	Light Emitting Diode
CFL	Compact Fluorescent Lamp
KAPEG	Kathmandu Alternative Power and Energy Group
PMSG	Permanent Magnet Synchronous Generator
WECS	Wind Energy Conversion System
PV	Photo-Voltaic
MPP	Maximum Power Point
MPPT	Maximum Power Point Tracking
kW	Kilo Watt
HAWT	Horizontal Axis Wind Turbine
VAWT	Vertical Axis Wind Turbine
WWEA	World Wind Energy Association
MW	Mega Watt
SWTs	Small Wind Turbines
GW	Giga Watt
TWh	Tera Watt-hour
SHS	Solar Home System
I-V	Current Voltage
P&O	Perturb and Observe
PSF	Power Signal Feedback
TSR	Tip Speed Ratio
HCS	Hill Climb Search
MHPP	Micro Hydro Power Plant
AHCS	Advanced Hill Climb Search
PCM	Pulsating Current Mode
CVM	Constant Voltage Mode

DCM	Discontinuous Conduction Mode
CCM	Continuous Conduction Mode
WG	Wind Generator
DFIG	Doubly Fed Induction Generator
SCIG	Squirrel Cage Induction Generator
CV	Constant Voltage
DFIG	Doubly Fed Induction Generator
IC	Incremental Conductance
SCC	Short Circuit Current
OCV	Open Circuit Voltage
IncCond	Incremental Conductance
NB	Negative Big
PB	Positive Big
NS	Negative Small
PS	Positive Small
ZE	Zero Error
RCC	Ripple Correlation Control
RPM	Revolution Per Minute
PFC	Power Factor Correction
PWM	Pulse Width Modulation
ALC	Active Line Conditioner
UPF	Unity Power Factor
VOC	Voltage Oriented Control
DPC	Direct Power Control
V-DPC	Voltage based Direct Power Control
VF-DPC	Virtual Flux based Direct Power Control
PI	Proportional Integral
MOSET	Metal Oxide Seemiconductor Field Effect Transistor
nF	nano Farad
nC	nano Coulomb
SVM	Space Vector Modulation
DPC-SVM	Direct Power Control Space Vector Modulation
DTC	Dead Time Control

Chapter 1

INTRODUCTION

1.1 ELECTRICITY NEEDS FOR ISOLATED POPULATION IN DEVELOPING COUNTRIES

Access to electricity is now a basic requirement of mankind. There are still many places around the world which have no access to electricity. International agencies report that 1.5 billion people have no access to electricity, which is more than 20% of world's population [Energy 2009]. Even though many of these places might have substantial potential for energy generation, the resources are not properly identified and/or utilized. Hence, people have to pay at high rates, if they have the financial resources, for the standard energy sources to fulfill their basic energy requirements such as lighting, charging small equipment like radios and mobile phones, and even heating. In many remote places, people often burn kerosene and even wood for basic lighting and heating. Burning these fuels not only deteriorates the environment but also has an adverse effect on people's health. Fumes produced from traditional lighting methods are somewhat toxic and can lead to chronic lung problems, especially when children are exposed. Using these dimmer sources of light for studying or handicraft production can strain the eyes and cause long-term vision problems. Studying after dark to dim, flickering candle light and kerosene lamps is difficult for children, and businesses usually cannot continue operating after dark. These traditional lights might even have a fire risk.

Generation of electricity through renewable energy sources such as solar, wind, and micro-hydro could be potential options for these remote places. For an isolated, off-grid and stand-alone system, the energy needs to be stored whenever available from these sources and then supplied if required. In hilly and remote regions where renewable energy potential is high, large scale generating systems could also be an option, but due to the complex geography and difficult infrastructure, small scale systems might seem more feasible. For basic lighting loads in these regions, small LED (Light Emitting Diode) lamps might be used which consume less power per lumens compared to other lighting loads such as incandescent, halogen lamp and CFL (Compact Fluorescent Lamp). Hence if LED lamps are used, the basic lighting loads could be fed from these small scale generating systems to the maximum number of consumers.

In a country like Nepal, where there is either no, or limited, access to remote places in hilly regions, small wind turbines and/or small hydro turbines might be promising options to fulfill the basic electrical load requirements. Rather than importing expensive systems, small turbines could be locally manufactured. It has been identified that wooden materials could be used for small wind turbine blade construction [Silwal *et al.* 2012]. Materials research at KAPEG (Kathmandu Alternative Power and Energy Group) shows that the local Pine and Lakuri timbers available in the hilly regions of Nepal have good mechanical properties such as nature of elasticity, breaking strength, strain and hardness. Hence these timbers could be used for blade construction at local furniture factories if the blade template is provided [Silwal *et al.* 2012]. Similarly, direct driven axial flux permanent magnet synchronous generators (PMSGs) has been found to be very popular in small wind turbines, mainly because of their effective design and relatively low constructional complexities. Hence the overall system could be even build by a person with minimal technical background.

The energy from these renewable/natural sources tend to vary throughout the day and hence optimizing the energy capture is a necessity. For a wind turbines, Photo-Voltaic (PV) arrays, and micro-hydro turbines, the output power is determined by the wind speed, irradiation and water flow respectively. Hence, the control of these systems needs to behave appropriately according to the variation of these parameters. For example, the turbine speed for wind and micro-hydro needs to be adjusted for different wind speeds or water flow such that the generated power available is optimized and the system runs at Maximum Power Point (MPP). Similarly, the output DC voltage and current of the PV array systems need to be adjusted in order to run them at MPP. The major objective of this thesis is to identify, design, model, build and test a low-cost, simple and flexible system that optimizes the power generation from all of these renewable sources. The system is also to be designed in such a way that the load demand of these remote areas is provided with high reliability.

The thesis will be focusing mainly on a MPPT controlled power converter development for a stand-alone small wind turbine where a battery bank system is used to store energy. Even so, the design will assume the same system could be used for similar power range micro-hydro and PV systems with some small adjustments. The power converter is to be developed such that the same unit could be used for power ranging from 50 W to 1kW power output. For the initial prototype, a commercially available wind turbine (explained in section 1.2) of a representative nominal power is identified and intended for use in the testing of the developed controller.

1.2 COMMONLY AVAILABLE SMALL WIND TURBINES

Small wind turbines can be as small as 50 Watts. These are used in boats, caravans, or miniature refrigeration units [Bartmann 2008]. Other small scale residential wind turbines are also gener-

Figure 1.1 A remote village in Nepal with small wind turbine

ally available that normally range from 300 W to 10,000 W, with a blade diameter from 2.1 m to 7.6 m respectively [Bartmann 2008]. The majority of the small wind turbines are Horizontal Axis Wind Turbines (HAWT) but Vertical Axis Wind Turbines (VAWT) are also equally growing in the small wind energy markets [Bartmann 2008]. According to the World Wind Energy Association (WWEA) 2013 report, the total number of installed small wind turbines reached up to 730,000 units at of the end of year 2011, compared to 656,000 units in 2010, 521,000 units in 2009 and 460,000 units in 2008.

The WWEA 2013 report also states that the largest share of small wind turbines are found in two major countries; China (5,00,000 units with total of 225 MW capacity) and USA (151,000 units with total of 198 MW capacity) followed by UK, Canada, Germany, Spain, Poland, Japan and Italy with 2000-22,000 units with total of 5 to 50 MW capacity.

Almost 500 small wind turbine manufacturing companies are identified to date among which 350 (nearly 62%) manufacture turbines up to 2kW in size, 80 (14%) manufacture 2-4 kW units, 70 (12%) manufacture 4-6 kW units, 10 (2%) are producing 6-8 kW size and almost 50 (9%) companies manufacture wind turbines ranging between 8-10 kW in size as shown in Figure 1.2.

Despite the attention given to multi-megawatt wind farms, the markets for autonomous electrical systems and distributed generation using small wind turbines can be attractive if prices for conventional electricity and fossil fuels are sufficiently high, or as in many developing countries, where many people live without access to electricity. Small wind turbines differ from large turbines in many ways, demonstrating their greater versatility. While large turbines require mature

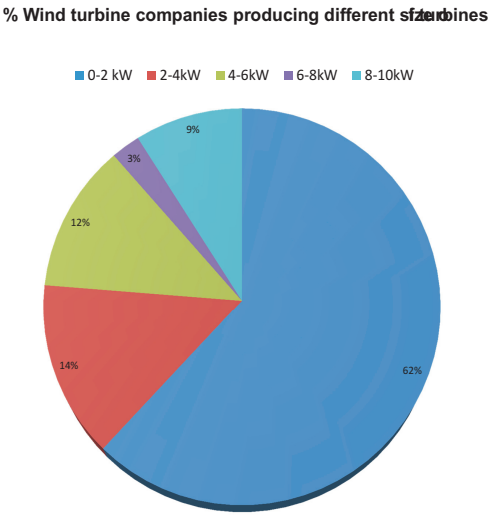

Figure 1.2 Number of Manufacturing companies producing different size of small wind turbines

power grids, small turbines have application both on and off existing power grids, as a result of their size and energy output. However, in spite of maturity reached on the development of the large and medium sized wind technology for wind farms, the state of the art for small wind turbines is far from technological maturity and economical competitiveness [Iuga].

The technology of small wind turbines (SWTs) is different from that used in large wind turbines which affects most of the subsystems: mainly the control, electrical system and design of the rotor blades. Most of the SWTs existing on the market are machines that have developed in an almost "hand crafted" way, with lower maturity compared to that achieved by large wind turbines[Iuga].

In spite of all these barriers, the market in developed countries is promising for grid-connected and off-grid applications due to promotion policies (such as capital cost buy-down, fed in tariffs and net metering), and even more so for developing countries because of the continuing decrease in specific costs and the increasing need for energy [Iuga].

1.3 PICO HYDRO SYSTEMS

Small scale hydro does not have any internationally agreed definition although the upper limit varies from 2.5 MW to 25 MW. Turbines upto 10 MW are normally accepted but in some literature turbine till 25 MW are also regarded as small scale [Paish 2002] while mini-hydro normally refers to the scheme below 2 MW, micro-hydro below 500 kW and Pico-hydro below 10 kW [Paish 2002].

Micro-hydro is "run of river" type where any dam or barrage is relatively small, usually just a

weir, and generally little or no water is stored. Therefore, run-of-river installations do not have the similar kinds of adverse effect on the local environment as large hydro.

According to the data published by "World Atlas, Hydropower and Dams", the planet has a hydro-generation potential of almost 14,605 TWh/year, out of which 8,772 TWh/year is economically feasible and only 3,356 TWh/year is exploited [Aquamedia Publications 2009]. This shows that more than 50% of the global economically feasible hydro is still not exploited. Figure 1.3 shows that Europe and North America have highest levels of exploited hydro potential, while huge resources still remain in Asia, Africa and South America. Currently, hydro power is the largest source of utilized renewable electricity, providing almost 16% of the world's electricity (3356 TWh in 2009), most of which comes from large hydro.

In 1995, global micro-hydro capacity in the world was estimated at 28 GW, supplying about 115 TWh of electricity. About 60% of this capacity was in the developed world, with 40% in developing areas [Awards 2009]. The main micro-hydro programmes in the developing world are in mountainous countries, such as Nepal (around 2,000 schemes, including both mechanical and electrical power generation) and other countries in the Himalayas [Awards 2009]. A typical micro-hydro system used for grinding maize in the rural village of Nepal is as shown in Figure 1.4.

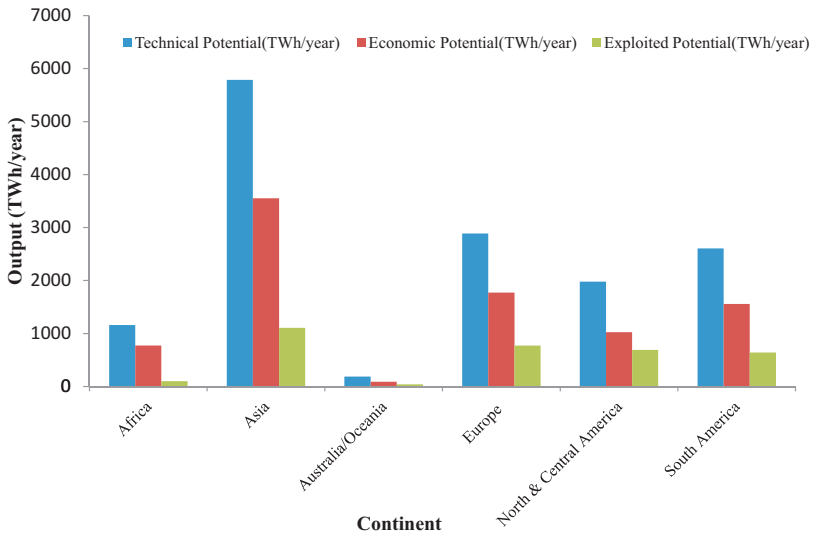

Figure 1.3 Exploited Hydro Potential by Continent

Figure 1.4 Grinding Maize with water mill in Nepal

1.4 SMALL SCALE PV SYSTEMS

Within small scale PV systems, Solar Home Systems (SHS) have been mostly employed by organizations working for rural electrification using PV. The size of SHS varies from 5-50 watts and consists of mounting structure, a rechargeable battery (normally lead acid battery), charge controller, one or more LED lights, an outlet for TV/radio loads, interconnects/switches and wiring [Aulich 1996]. It has been found that SHSs can compete with the cost of a local grid provided by the large diesel generators and monthly payment for SHSs is lower than the that for kerosene or kerosene/battery-systems [Aulich 1996]. A typical SHS system with a solar panel, battery, lights and charge controller is as shown in the Figure 1.5.

Figure 1.5 A complete Solar Home System (SHS)

The target market for this particular application of SHS generally includes individuals living in rural villages of developing countries who are not connected to the grid and without a sustainable or reliable source of electricity. solar solution will need to be customized depending on the village, available materials, need, and income of the potential customer.

1.5 RESEARCH OBJECTIVES

The major objective of this research is to develop a robust and low cost MPPT controlled power converter suitable for most of these small scale renewable energy systems, such as wind turbines, micro-hydro and PV (focussing mainly on the small wind turbine). Additionally, in order to draw sinusoidal current out of the generator side a PFC boost converter is simulated, designed and built. Similarly, a DC-DC buck converter is also designed and built such that it is suitable for charging a battery bank with MPPT properties. Different MPPT algorithms suitable for these small scale systems are initially identified and then the most suitable is implemented using a micro-controller.

1.6 THESIS OUTLINE

Different MPPT algorithms developed so far suitable for small wind turbine, PV arrays and micro-hydro are summarized in chapter 2. MPP modeling for these systems is done in Chapter 3 while Chapter 4 summarizes the simulation results of the controller systems, especially focusing on the PFC boost rectifier and DC-DC converter. Chapter 5 focusses on the hardware development process, component selections, PCB design and hardware results when connected to a representative wind turbine. Chapter 6 provide conclusions and the future works.

Chapter 2

BACKGROUND

2.1 INTRODUCTION

The energy that can be extracted from renewable energy sources like Wind Energy Conversion Systems (WECS), Photo-Voltaic (PV), and water (hydro-electric) varies throughout the day and is dependent on the geographical location. For a particular wind velocity (for WECS), irradiation and temperature (for PV) and water flow rate (for hydro), there is always a point at which maximum power out of these systems can be extracted. The output power that can be extracted depends upon the accuracy at which peak power points are tracked by the implementation of a Maximum Power Point Tracking (MPPT) controller.

The Current-Voltage (I-V) characteristic of a solar cell is a nonlinear curve and changes with irradiation and temperature. In general, there is an optimum point on the I-V or P-V (Power-Voltage) curve at which the entire PV system operates at maximum efficiency. Similarly, output power from WECS as a function of rotor speed changes with the variation of wind speed. There is always an optimum rotor speed (ω_{ropt}) of WECS for a particular wind speed at which maximum power could be extracted out of the system. The location of the Maximum Power Point (MPP) is not known but could be located, either through calculation models or through search algorithms. The amount of output power from these systems depend upon the accuracy with which the peak power points are tracked by MPPT controllers. Hence MPPT techniques are used to maintain either the PV array's, wind turbine's or hydro-turbines operating point at the MPP.

Different MPPT techniques found in the literature for WECS, PV and micro-hydro systems are discussed in this chapter. Perturb and Observe (P&O) [Xiao and Dunford 2004] [Al Amoudi and L 1996] [Hua and Lin 2001] [Femia *et al.* 2005], Incremental Conductance (IC) [Femia *et al.* 2005] , Artificial Neural [Hiyama *et al.* 1995] [Ro and Rahman 1998] [Hussein *et al.* 2002] [Sun *et al.* 2002] [Zhang *et al.* 2002] and fuzzy logic methods [Veerachary *et al.* 2003] are a few MPPT techniques that have been used for PV systems. Similarly, different MPPT controllers for WECS can be classified into three major control systems namely Tip Speed Ratio (TSR) Control [Thongam and Ouhrouche 2012], Power Signal Feedback (PSF) control [Thongam and Ouhrouche 2012] and Hill Climb Search (HCS) [Wang and Chang 2004] control. HCS (or P&O)

iteration method is normally used for MPPT control for Micro Hydro Power Plants (MHPPs) systems.

2.2 DIFFERENT MPPT CONTROL ALGORITHMS FOR WIND ENERGY CONVERSION SYSTEMS

MPPT algorithms for WECS researched so far are mainly classified into three categories. Namely Tip Speed Ratio (TSR) control, Power Signal Feedback (PSF) control and Hill-Climb Search (HCS) Control.
The TSR control method regulates the rotational speed of the generator in order to maintain TSR (the ratio between blade tip speed to the wind speed) at the optimum value in order to extract maximum power out of the turbine. This method requires knowledge of the optimum TSR, wind speed, and turbine speed in order to extract maximum power point. A general block diagram of WECS with TSR control is as shown in the Figure 2.1 [Thongam and Ouhrouche 2012]. Note that the combination of the turbine and generator systems is often refered to as the "Wind Generator" (WG).

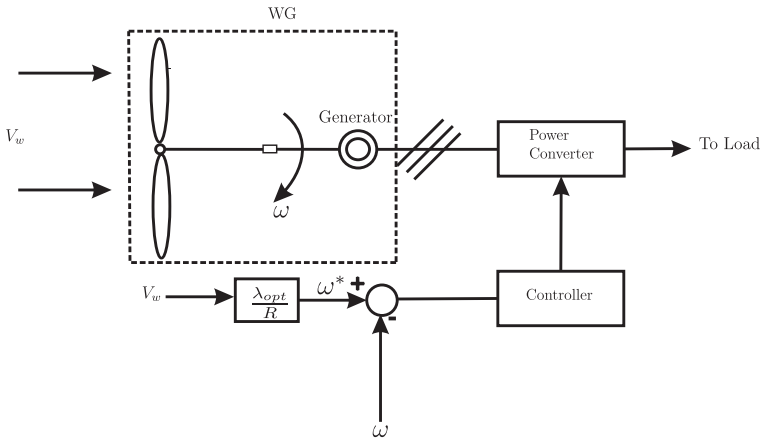

Figure 2.1 TSR Control of WECS
[Thongam and Ouhrouche 2012]

In PSF control, knowledge of the maximum power curve of the wind turbine is required, which is obtained through the control mechanism. Using wind speed or rotor speed as an input, the reference power is generated either using the recorded maximum power curve or using the mechanical power equation. Figure 2.2 shows WECS with PSF control for maximum power extraction [Thongam and Ouhrouche 2012].

The HCS control (or Perturb & Observe) algorithm continuously searches for the peak power of the wind turbine. Depending upon location of an operating point and the relation between changes in power and speed, the tracking algorithm computes the optimum control signal in

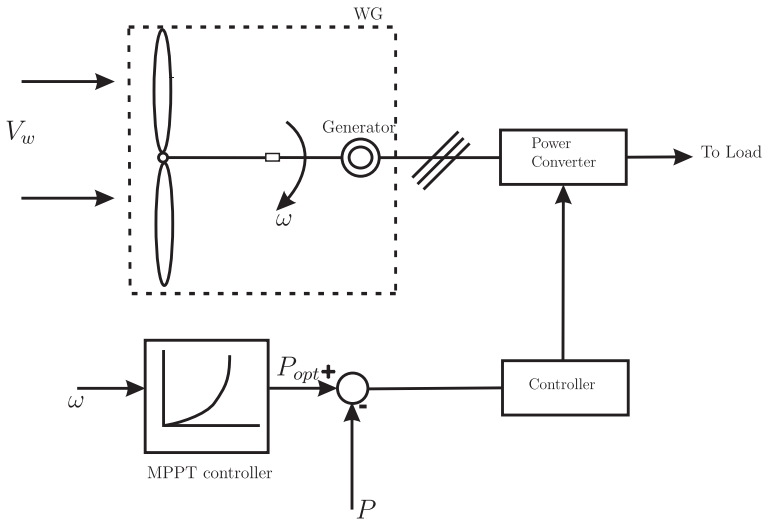

Figure 2.2 Power Signal Feedback Control of WECS
[Thongam and Ouhrouche 2012]

order to drive the system to the point of maximum power. This control system is normally based on perturbing the turbine shaft speed in small steps and observing the change in turbine mechanical power.

In the HCS method, signs of change in generator speed ($\triangle\omega$) and the change in output power with respect to generator speed ($\triangle p/\triangle\omega$) are computed. The shaft speed is either incremented (if $\triangle\omega > 0$) in small steps as long as $\triangle p/\triangle\omega > 0$ or decremented (if $\triangle\omega < 0$) in small steps for $\triangle p/\triangle\omega < 0$. This is continued until the MPP is reached (i.e. $\triangle p/\triangle\omega$=0). If incrementing the turbine speed results in the $\triangle p/\triangle\omega < 0$ and decrementing the turbine speed results in the $\triangle p/\triangle\omega > 0$ then the direction of turbine speed change must be reversed.

The main advantage of HCS control over TSR and PSF control is that it neither requires knowledge of the maximum power nor the wind velocity to determine MPP. This method is usually suitable for systems with small inertia (small turbine speed changes time constant) [Wang and Chang 2004] [Koutoulis *et al.* 2001]. Since turbine speed cannot follow wind speed changes quickly for medium and large inertia wind turbines, the HCS method without any other controller will not be able to control the wind turbine system properly [Thongam and Ouhrouche 2012]. HCS deteriorates in performance under rapidly changing wind conditions because of two serious problems. Namely speed-efficiency tradeoff and incorrect directionality. A larger perturbation size increases the speed of convergence but deteriorates the efficiency of MPPT by amplifying the oscillations around the MPP. Efficiency can be boosted with smaller step size but convergence speed becomes slower and therefore the controller might become incapable of tracking MPP for rapidly changing wind conditions. Hence, for conventional HCS control, there is always a tradeoff between the tracking speed and control efficiency.

2.2.1 Review of Existing Research for HCS MPPT of WECS with Permanent Magnet Synchronous Generators

Permanent Magnet Synchronous Generators (PMSGs) are mostly applicable for small wind turbines because of their higher efficiency, high power density, availability of high-energy permanent magnet material at a reasonable price, and possibility of smaller turbine diameter in their direct driven applications [Thongam and Ouhrouche 2012].
Among different HCS algorithms for PMSGs, the one proposed by Wang and Chang [Wang and Chang 2004] uses the principle of a search-remember-reuse technique. This method uses memory for storing peak power points obtained during training the process, which are used later for tracking MPPs. The algorithm starts from an empty intelligent memory with a relatively poor initial performance. The training mode uses the searched data by an advanced hill-climb search to gradually train the intelligent memory to record training experience during an execution period. The algorithm reuses the recorded data in an application mode for fast execution. The search-remember-reuse repeats itself until an accurate memory of system characteristics is established. Hence, after the algorithm is adequately trained, its power extraction performance is optimized. In this Advanced Hill Climb Search (AHCS) method as shown in the Figure 2.3, an intelligent memory is trained on-line during system operation. Every execution cycle starts with sampling of V_{dc} (output DC voltage) and P_o (output power) and calculation of their first derivative. The mode switch rule directs the control into one of the three execution modes, namely, initial mode, training mode, and application mode. The inverter current demand (I_{dm}) is calculated in that mode and fed to the inverter to regulate the system power output. I_{dm} is defined as the requested peak value of the sinusoidal inverter output current . The Maximum Power Error Driven (MPED) mechanism provides the system with a preliminary optimized operating point when the intelligent memory is empty. The reference signal for MPED mechanism is P_{max} which can only be reached when wind speed is sufficiently high. The intelligent memory records the system maximum power points and the corresponding control variables at different operating conditions. The Direct Current Demand Control (DCDC) utilizes the optimized relationship between the V_{dc} and I_{dm} recorded by the intelligent memory and generates I_{dm} based on the present value of V_{dc}.

Disturbance injection based HCS is proposed by Wang et al. [Wang *et al.* 2009]. In this control algorithm, a sinusoidal perturbation signal to the chopper (DC-DC Voltage Converter) is injected and then the system output power is sampled at $\pi/2$ and $3\pi/2$ of each cycle, the difference of which determines the next perturbation. This method does not require wind speed or rotor speed sensing.
The HCS method as proposed by Wai et al. [Wai *et al.* 2007] controls output power as well as the electrical torque which indirectly controls the speed of the generator. Finally, an optimum

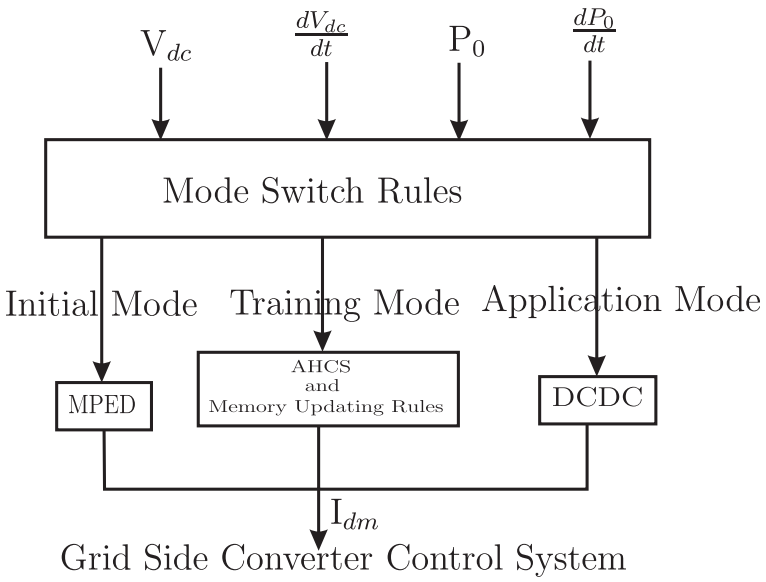

Figure 2.3 Advanced HCS Structure

speed for driving power to the MPP is obtained. The maximum power error driven mechanism operates like a traditional hill-climbing method and drives the output power by gradually increasing to its maximum value by regulating the direction of the current command according to the power variation trend. The maximum power differential speed control produces an additional step of current command based on the instantaneous difference of generator speed, so that it can prevent the wind turbine from stalling at suddenly dropping wind speed, and achieve the maximum power extraction. It adds a faster control index into the control value which is proposed to be an exponential function of the differential of the generator speed and therefore it causes sharp increase or decrease in speed. The controller generates a current command for controlling the grid side converter and does not require wind speed measurement.

A variable tracking step for MPPT is proposed by Yaoqin et al.[Yaoqin *et al.* 2002]. In this type of controller, the constant step size used in the conventional controllers is replaced with a scaled measure of the slope of the power with respect to perturbed generator speed $\triangle P/\triangle\omega$. A larger step size is used when an operating point is far away from the peak due to a larger magnitude of P-ω slope and as the peak gets nearer, the step size should automatically approach to zero.

An adaptive control algorithm for MPPT is proposed by Hui and Bakhshai [Hui and Bakhshai 2008] in which the MPP is tracked under fluctuating wind conditions. The algorithm initiates TSR control with an approximate optimal TSR value. When the measured wind velocity is found to be stable, the algorithm switches to HCS to obtain the actual optimal point. When the true peak power is reached, a memory table of an optimum generator speed versus the corresponding wind velocity is updated and then the TSR is corrected. When the wind speed varies, the rotor speed reference for MPP is applied from the memory if a recorded data at current wind speed is present and if not it is calculated using TSR. This method requires both wind speed and rotor speed measurements.

A MPPT controller for PMSG WECS via a DC-DC boost converter is proposed by Molina and Mercado [Molina and Mercado 2008] in which the duty cycle of the converter is adjusted according to the result of the comparison of successive output power measurements from the turbine. The MPPT algorithm operates by continuously perturbing the rectified dc output voltage (V_{dc}) via the dc-dc converter duty cycle and comparing the current output power with previous perturbation sample. If the power is increasing, the perturbation will be continued in the same direction such that rotor speed is increased otherwise the perturbation direction is inverted. When the optimal speed of the rotor for a specific wind velocity is reached, the HCS algorithm will have tracked the MPP and hence will settle at or around this point.
Tafticht et al.[Tafticht *et al.* 2006] details how a buck-boost converter is used to achieve maximum power control of the wind turbine for PMSG driven WECS.The PMSG is controlled according to generator speed such that the turbine power settles down to the MPP. The DC link power is used as an input for the controller and output is adjusted via the buck-boost converter duty cycle.
The MPPT controller as used by Patisons et al. [Patsios *et al.* 2008] combines two commonly used methods; (1) The tracking method based on an optimum power versus speed characteristic, and (2) The HCS method. The algorithm measures generator speed and computes an optimum torque (T_{opt}, the torque which maximizes the power) and an actual torque (T_t). For a small error between an optimal and measured torque ($\triangle T$), the perturb and observe method is performed based on the actual power calculation, overlooking the use of an optimum T-ω characteristic. However, if $\triangle T$ exceeds a certain limit, the duty cycle is adjusted according to the optimum characteristic. As such, the system tracks MPP through perturb and observe process under normal circumstances, however, it uses a predefined T-ω characteristic in case the perturb and observe algorithm is thrown off due to heavy disturbances created by sudden wind speed changes or improper initialization.
In [Kesraoui *et al.* 2011], a MPPT algorithm is designed for a system that consists of a diode bridge rectifier, a dc-dc boost converter and a current controlled voltage source inverter. In this system, a reference voltage (V_{dcref}) is generated (which corresponds to maximum power out of the generator) through Newton-Raphson method. The step change of reference voltage is obtained using the change in power with respect to change in voltage (i.e $\frac{dp}{dV_{dc}}$). The change in power is given by the equation 2.1[Kesraoui *et al.* 2011].

$$\triangle V_{dc} = \frac{P(k) - P(k-1)}{slope(k) - slope(k-1)} \tag{2.1}$$

where, $P(k)$ and $P(k-1)$ are the powers at k and k-1 sampling times respectively. slope(k) could be determined as in the equation 2.2.

$$slope(k) = \frac{dP}{dV_{dc}} = \frac{P(k) - p(k-1)}{V_{dc}(k) - V_{dc}(k-1)} \tag{2.2}$$

where,$V_{dc}(k)$ and $V_{dc}(k-1)$ are the dc voltages in k and k-1 sampling times respectively.

Faster convergence towards the MPP with less power oscillation could be achieved using the method of variable step [Kesraoui *et al.* 2011]. If the power is very close to MPP, small $\triangle V$ is imposed whereas for the power lying far from MPP large $\triangle V$ is applied.
In [Datta and Ranganathan 2003], a MPPT controller is proposed which dynamically adjusts the generator speed according to the magnitude and direction of active power and finally reaching to the point where $\frac{dP}{d\omega} = 0$. The magnitude in the speed reference is determined by an incremental change in power multiplied with some constant as given by the equation 2.3 [Datta and Ranganathan 2003].

$$|(\triangle\omega)^*(k)| = |\triangle P(k).K_t| \tag{2.3}$$

where, K_t is a factor which determines a reference for the change in rotor speed and normally depends upon the slope of the $P-\omega$ curves of a particular turbine. In order to avoid overshooting of an optimum operating point (which results in the oscillation about the peak power point), the maximum value of K_t should be below the lowest value of $\frac{\triangle\omega(t)}{\triangle P}$.
Similarly, the sign of the $\triangle\omega^*(k)$ is determined by the change in the previous speed reference ($\triangle\omega^*$ (k-1)) and the change in power ($\triangle P$) as given below [Datta and Ranganathan 2003].

$if \triangle\omega^*(k-1) = 0$
$S = Sign[\triangle P(k)]$,
$else$
$S = sign(\triangle P(k)).Sign(\triangle\omega(k-1))$
$\triangle\omega^*(k) = S.|\triangle P(k).K_t$

The reference generator speed is not changed if the magnitude of $\triangle P(k)$ is within a small defined band otherwise it is changed by $\triangle\omega(k)$ as defined by an algorithm below.

$if \triangle P(k) <= P_{band}$
$\omega^*(K) = \omega^*(K-1)$
$else$
$\omega^*(K) = \omega^*(K-1) + \triangle\omega^*(k)$

In [Lo and Chen 2011], a buck type power converter suitable for battery charging with MPPT capability for a small wind turbine is proposed in which two battery charging modes are considered. Namely Pulsating Current Mode (PCM) and Constant Voltage Mode (CVM). A PCM is operated when battery voltage (V_b) is below threshold voltage (V_{th}) and CVM is operated if V_b is above V_{th}. During PCM operation, the charger is operated in Discontinuous Conduction Mode (DCM) with constant on-time control generating pulsating current for battery charging. The average power for charging the battery during one switching cycle is as given by equation 2.4 [Lo and Chen 2011].

$$P_0 = I_{avg} V_b = \frac{d_1^2}{2fL}(V_{in}^2 - V_b V_{in}) \tag{2.4}$$

where, I_{avg} is the average inductor current, f is the switching frequency, L is inductance and d_1 is the energizing period of an inductor. The equation 2.4 shows that the average power to the battery is a second order polynomial which is similar to that of MPP curve. Hence, by appropriately selecting the parameters f, L, V_b and d_1 according to the turbine characteristic makes the battery charging power equal to MPP of the wind turbine [Lo and Chen 2011]. The charger is operated in the Continuous Conduction Mode (CCM) if an input DC voltage(V_{in}) is equal to $\frac{V_b}{d_1}$.

The MPPT control as proposed by Koutroulis and Kalaitzakis [Koutroulis and Kalaitzakis 2006] is based on directly adjusting the dc/dc converter duty cycle, D, according to the result of the comparison of successive Wind Generator (WG) output power measurements. Although the variation of wind speed with time is large, power absorbed by the WG varies relatively slowly because of the slow dynamics of the turbine-generator system. The problem of maximizing the WG output power using the converter duty cycle as a control variable is effectively solved using the steepest ascent method given by the equation 2.5.

$$D_k = D_{k-1} + C_1 \frac{\triangle P_{k-1}}{\triangle D_{k-1}} \tag{2.5}$$

where, D_k and D_{k-1} are the duty cycle values at k and $k-1$ sampling time and C_1 is the step change in the duty cycle. This method is based on the fact that at MPP $\frac{dP}{d\omega}$ and hence $\frac{dP}{dD}$ (D being dc-dc converter duty cycle) is equal to zero.

Power as a function of the duty cycle has a extremum point which coincides with MPP of the wind turbine. Hence adjusting duty cycle according to the equation 2.5 ensures that MPP of the wind turbine is achieved at any wind conditions.

Some of the other MPPT algorithms for different types of wind turbines (both horizontal and vertical axis) with different types of generator (Doubly Fed Induction Generators (DFIG), Squirrel Cage Induction Generator (SCIG) and Permanent Magnet Synchronous Generator (PMSG)) are briefly explained by Thongam and Ouhrouche in [Thongam and Ouhrouche 2012].

2.3 COMMON MPPT CONTROL ALGORITHMS FOR PV SYSTEMS

Among different MPPT methods for PV systems discussed in various literature; the most widely used techniques are described in the following sections starting from the simplest method.

2.3.1 Constant Voltage MPPT Method

The Constant Voltage (CV) algorithm is the simplest MPPT control algorithm in which an operating point of a PV array is always kept near MPP by regulating the array voltage and matching it to a fixed reference voltage (V_{ref}), which is equal to the V_{MPP} of the characteristic PV module, or another pre-calculated best voltage value [Carvalho *et al.* 2004]. The CV method assumes that temperature variation and insulation on the array has an insignificant effect on V_{MPP} and the constant reference voltage is an adequate approximation of real MPP [Yu *et al.* 2002]. Hence, the operating point is never at true MPP and different data have to be adopted for different geographical regions. The general flow chart for the CV method is as shown in the Figure 2.4 . In order to setup the duty cycle (D) of the DC/DC converter, the PV array voltage (V_{PV}) needs to be measured. For low insulation conditions, the CV algorithm is more effective than P&O and IC methods, and because of this CV is generally combined together with other MPPT techniques [Yu *et al.* 2002].

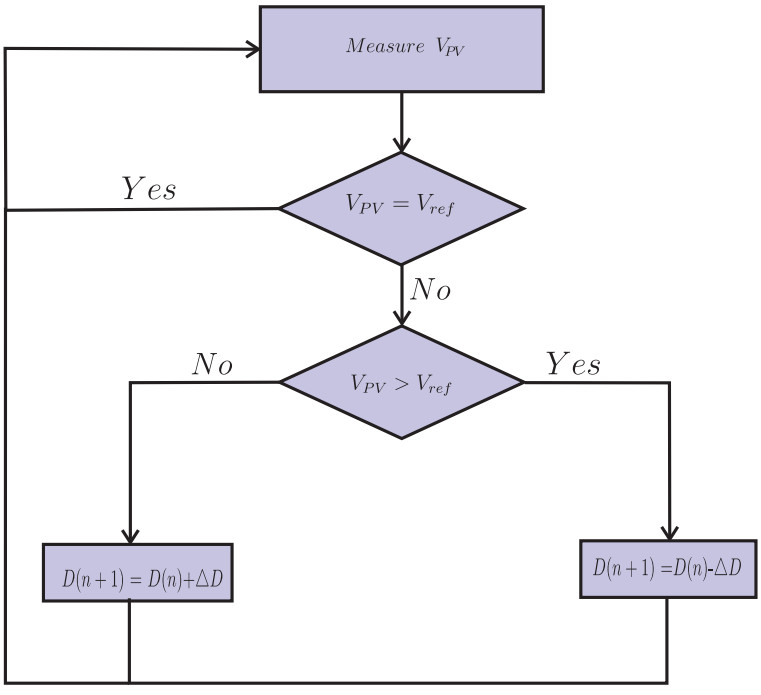

Figure 2.4 Flowchart of the CV method

2.3.2 Short Circuit Current Pulse Method

In this method, the MPP is achieved by using reference current (I_{ref}) for the Power converter controller. The optimum operating current for maximum output power is proportional to the short-circuit current (I_{SC})under various condition of irradiance level S as shown in Equation 2.6 [Noguchi *et al.* 2002a].

$$I_{ref} = K_1 I_{SC}(S) \tag{2.6}$$

where K_1 is a proportionality constant which is dependent on the PV characteristics being used and needs to be computed beforehand by empirically determining V_{MPP} and I_{SC} at different irradiance and temperature. The value of K_1 is usually taken between 0.78 to 0.92 [Noguchi *et al.* 2002a].
In order to measure the I_{SC}, a static switch in parallel with the PV system is connected to create the short circuit condition. Consequently, the array current is also measured in order to set up the duty cycle of DC/DC converter. The overall flowchart for this method is as shown in the Figure 2.5.

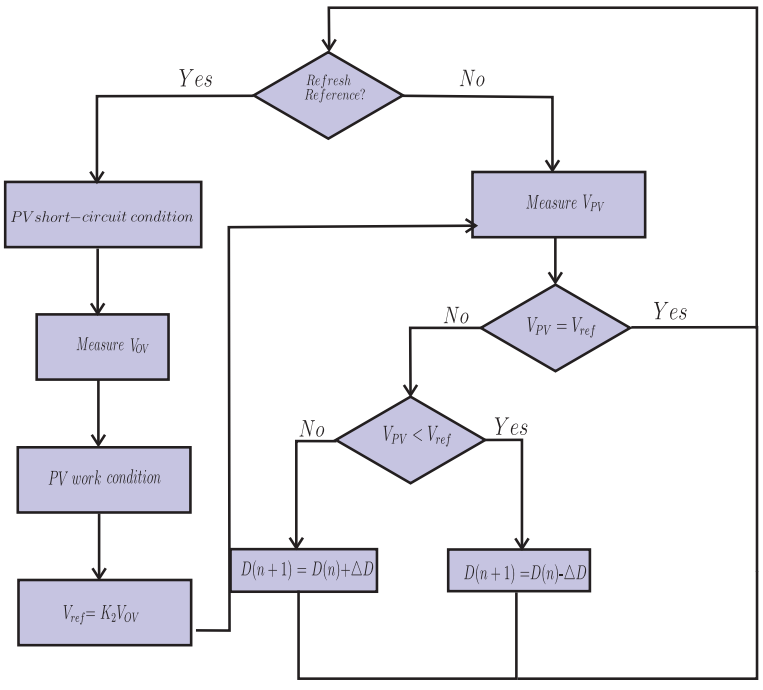

Figure 2.5 Flowchart of the SCC method

2.3.3 Open Circuit Voltage Method

This MPPT method considers that the maximum power point voltage (V_{MPP}) is always close to the fixed percentage of the open-circuit voltage (V_{OC}). V_{OC} depends upon the characteristics of the solar cell. It has been found that production spread, temperature and solar insulation levels changes the position of MPP within a ± 2% tolerance band [Dolara *et al.* 2009]. A commonly used ratio of V_{MPP} and V_{OC} is normally taken as 0.76 and is described by equation 2.7 [Kumari and Babu 2011].

$$V_{MPP} = K_2 V_{OC}(S) \tag{2.7}$$

where K_2 is a proportional constant always less than 1. Its value is normally taken between 0.71 to 0.8, the commonly used value is 0.76 [Kumari and Babu 2011]. Hence, the algorithm is also called the 76% algorithm. This algorithm requires the measurement of V_{OC} when the circuit is actually open circuited. Because of this, a static switch needs to be connected which is used to open circuit the PV array. For an open-circuit, I_{PV} is equal to zero hence no power is supplied by PV panels and consequently no power is generated. The PV array voltage (V_{PV}) is also measured in order to change the duty cycle of the power converter as identified in the flowchart shown in Figure 2.6. Although this system has simplicity and good starting characteristic, it is often combined with other MPPT techniques due to its poor performance with changing external environment conditions [Go *et al.* 2011].

2.3.4 Perturb and Observe Methods

The P & O method is one of the most commonly used MPPT methods in practice. This method operates by periodically perturbing (i.e. either incrementing or decrementing) the array terminal voltage and comparing PV output power with that of the previous perturbation cycle. If the PV array change in voltage increases power, the control system moves the operating point in same direction. Otherwise, the operating point is changed to the opposite direction. In the next perturbation cycle the algorithm continues in the same way.

The major problem with this method is that an array terminal voltage is perturbed every MPPT cycle and hence when MPP is reached, the output power oscillates around the maximum, resulting in the reduction of output power. It sometime fails to reach MPP under continuously increasing or decreasing irradiation conditions.

Among different P & O methods, the classic P & O technique, an optimized, and three points P & O methods are normally used. In the classic P & O technique (P & Oa), the perturbations of PV operating point have a fixed magnitude as shown in Figure 2.7.

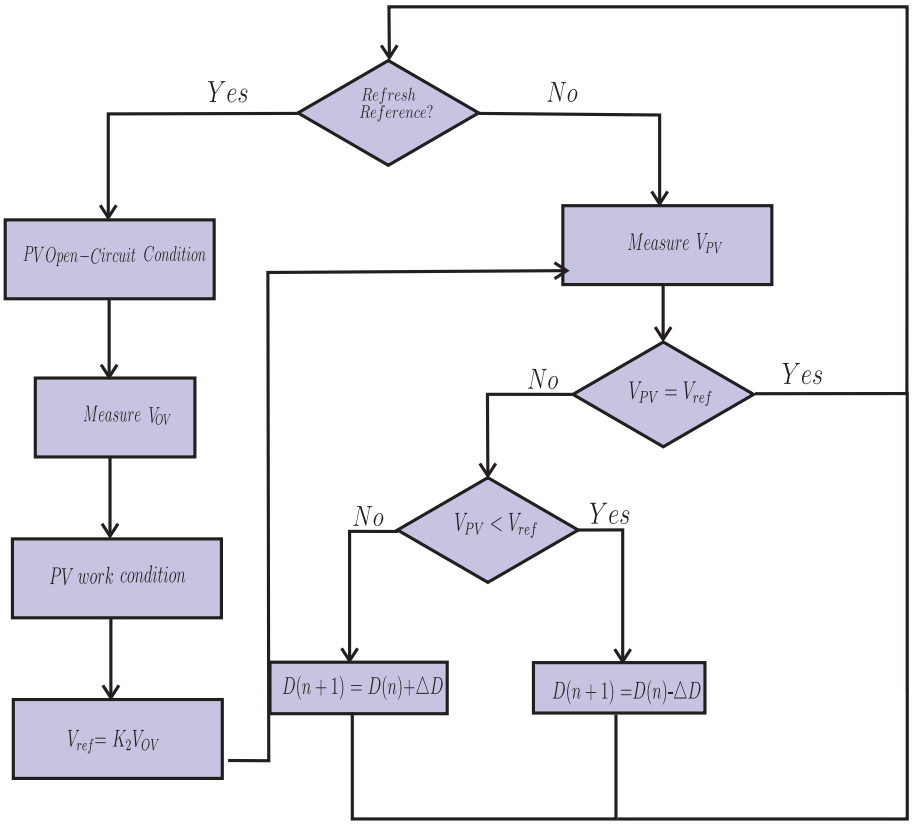

Figure 2.6 Flowchart of the OCV method

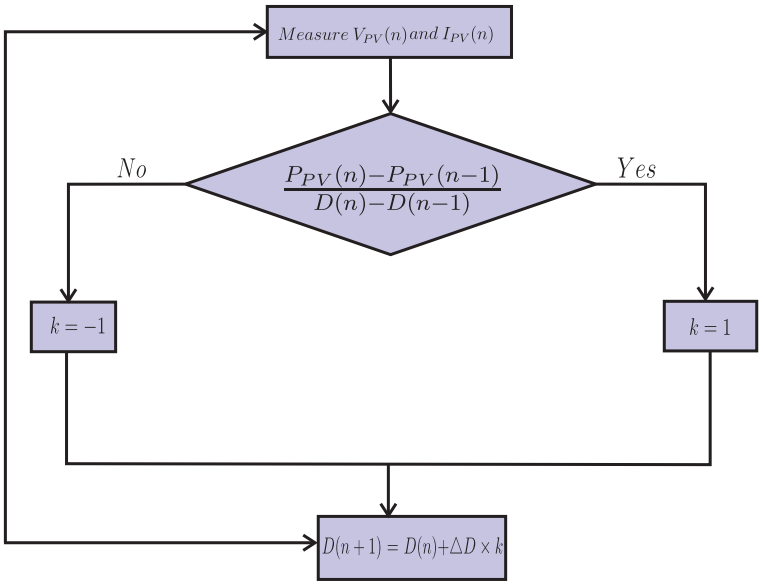

Figure 2.7 Flowchart of the P & O(a) method

Whereas in an optimized P & O technique (P & O(b)) method, several samples of average power is sampled and is used to adjust the magnitude of perturbation of the PV array operating point. Reducing perturbation step size around the MPP reduces the oscillation, however, a smaller

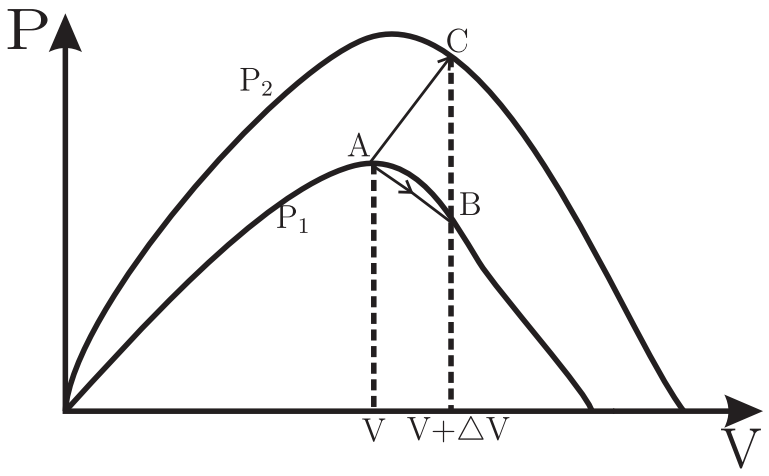

Figure 2.8 Divergence of hill climbing from MPP for rapid changing environment conditions [Wasynczuk 1983]

perturbation size slows down MPPT. A solution to this is to have variable perturbation size that gets smaller as MPP is approached [Xiao and Dunford 2004] [Al Amoudi and L 1996] [Hua and Lin 2001] [Femia *et al.* 2005].

The P & O method can fail under rapidly changing atmospheric conditions as illustrated in Figure 2.8. In Figure 2.8, assuming the scenario starts at the operating point A, for constant atmospheric condition a perturbation $\triangle$V in the PV array voltage will shift the operating point to point B which reverses the perturbation due to a decrease in power. Alternatively, if there is rapid increase in irradiance such that the power curve is shifted from P_1 to P_2 within one sampling period, the operating point will shift from B to C. This represents an absolute increase in power and hence perturbation continues in the same direction. Consequently, the operating point diverges from the MPP and keeps diverging if the irradiance steadily increases.

In order to ensure that the MPP is tracked even after a sudden change in the irradiance, a three points weight comparison P & O method (P & O(c)) is used in which the current power point is compared to the two preceding power point values before a decision is made about the perturbation sign [Hsiao and Chen 2002]. An optimized sampling rate [Femia *et al.* 2005] or a simply high sampling rate could be used within the P & O method. Similarly, a toggling between the traditional hill climbing algorithm and a modified adaptive hill climbing mechanism is used in order to prevent a deviation from the MPP.

2.3.5 Incremental Conductance Method

The Incremental Conductance (IncCond) method is based on the fact that the slope of a PV array power curve is zero at the MPP as shown in the Figure 2.9, and hence equation 2.8 holds true at MPP [Femia *et al.* 2005].

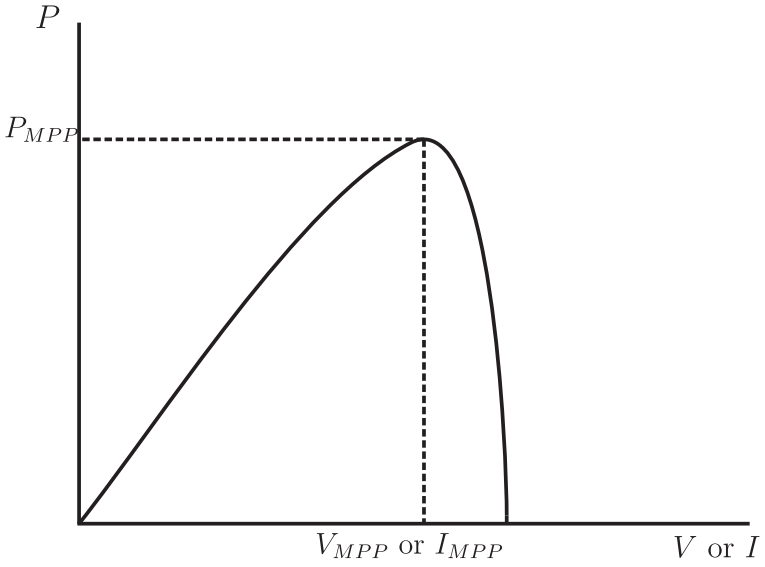

Figure 2.9 Characteristic PV array Power Curve
[Wasynczuk 1983]

$$\frac{dI_{PV}}{dV_{PV}} + \frac{I_{PV}}{V_{PV}} = 0 \tag{2.8}$$

where I_{PV} and V_{PV} are PV array current and voltage respectively. For an operating point to the right of the MPP, $\frac{dI_{PV}}{dV_{PV}} + \frac{I_{PV}}{V_{PV}} < 0$. Similarly $\frac{dI_{PV}}{dV_{PV}} + \frac{I_{PV}}{V_{PV}} > 0$ indicates that the operating point is to the left of the MPP. Hence, the MPP can be tracked by comparing the instantaneous conductance ($\frac{I_{PV}}{V_{PV}}$) to the incremental conductance ($\frac{dI_{PV}}{dV_{PV}}$). After reaching the MPP, the operation of the PV array is maintained at this point and the perturbation is stopped unless a change in dI_{PV} is noted. If there is certain change in dI_{PV}, the algorithm decrements or increments the PV array voltage V_{PV} in order to track a new MPP. The increment or decrement size determines how fast the MPP is tracked. Under rapidly changing atmospheric conditions, the IncCond method shows a good performance [Dolara *et al.* 2009]. The flowchart for the IncCond method is as shown in Figure 2.10. This algorithm is implemented with finite variability size (hence dI and dV is replaced by $\triangle I$ and $\triangle V$).

2.3.6 Fuzzy Logic Control MPPT

Fuzzy Logic controllers work with imprecise inputs, and do not require an accurate mathematical model, and can handle nonlinearity [Veerachary *et al.* 2003]. This type of control generally consists of three stages: fuzzification, rule based lookup table, and defuzzification. During fuzzification, numerical input variables are converted into linguistic variables based on the membership function as shown in Figure 2.11 [Hillowala and Sharaf 1992] [Simoes *et al.* 1998] [Veerachary *et al.* 2003] [Khaeintung *et al.* 2004]. In this controller, five fuzzy levels are used: NB (Negative

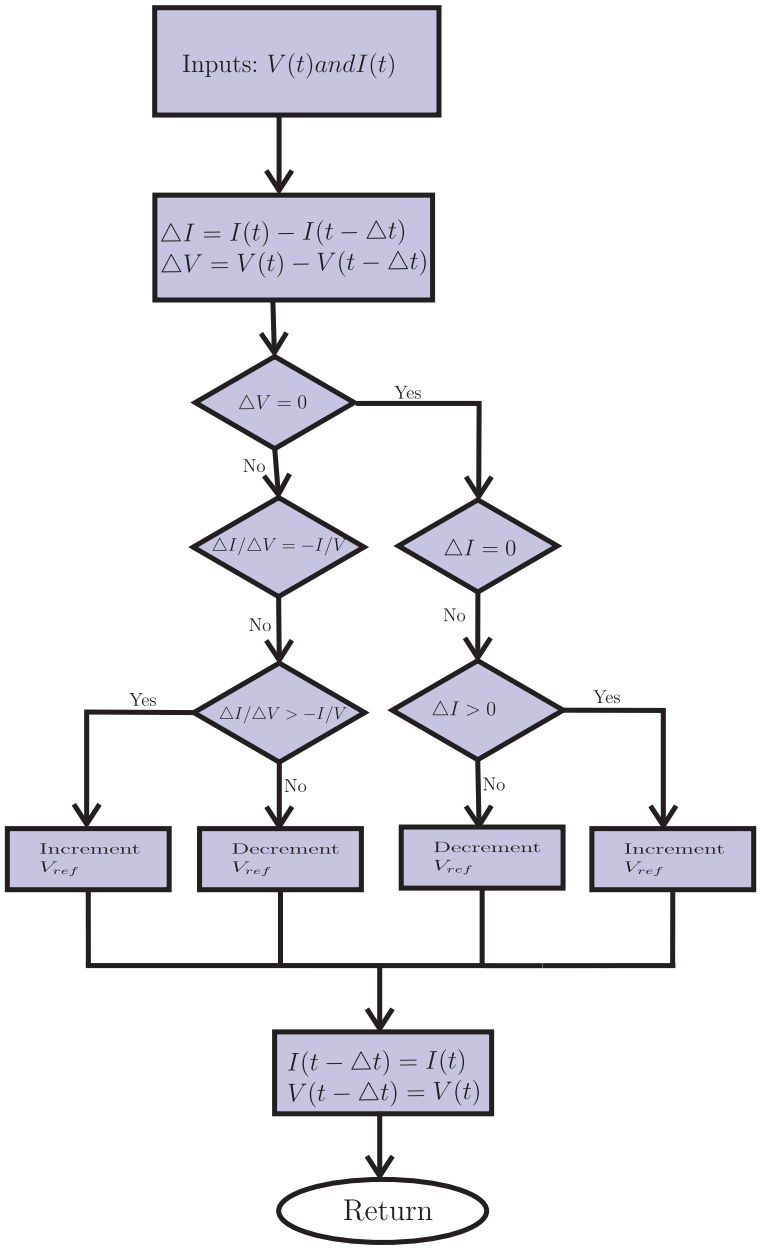

Figure 2.10 IncCond Algorithm as given in
[Hussein and Mota 1995][Kim *et al.* 2001][Kuo *et al.* 2001][Wu *et al.* 2003]

Big), NS (Negative Small), PS (Positive Small), and PB (Positive Big). In Figure 2.11, a and b are based on the range of values of the numerical variable.

Usually, the inputs to the MPPT fuzzy logic controller is an error (E_r) and change in an error ($\triangle$E). A change in an error ($\triangle E_r$) and its approximation can be made [Khaeintung *et al.* 2004]. E and $\triangle E$ are given by equation 2.9 and equation 2.10 which considers the fact that dP/dV vanishes at the MPP.

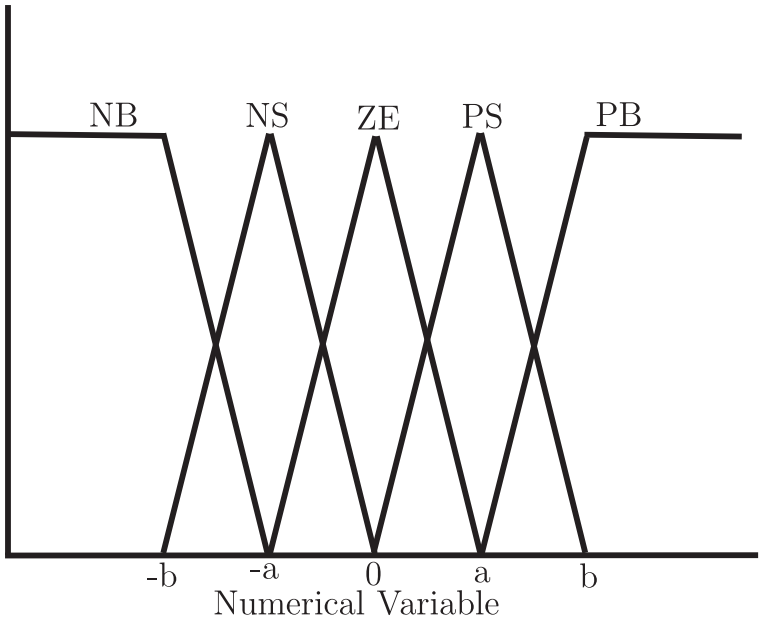

Figure 2.11 Membership Function for Inputs and Outputs of Fuzzy Logic Controller

$$E_r(n) = \frac{P(n) - P(n-1)}{V(n) - V(n-1)} \tag{2.9}$$

$$\triangle E_r(n) = E(n) - E(n-1) \tag{2.10}$$

After calculating and converting the values of E_r and $\triangle E_r$ into the linguistic variables, the fuzzy logic controller output, which is generally a change in duty ratio ($\triangle D$) of the power converter, can be looked up in a rule based table such as in Table 2.1 [Won *et al.* 1994].

Table 2.1 Fuzzy Rule Based Table as shown in [Won *et al.* 1994]

$E/\triangle$**E**	**NB**	**NS**	**ZE**	**PS**	**PB**
NB	ZE	ZE	NB	NB	NB
NS	ZE	ZE	NS	NS	NS
ZE	NS	ZE	ZE	ZE	PS
PS	PS	PS	PS	ZE	ZE
PB	PB	PB	PB	ZE	ZE

The linguistic variables assigned to $\triangle D$ are for different combinations of E_r and $\triangle E_r$ which are based on the specific power converter being used and also on the knowledge of the user. Table 2.1 is based on a boost converter. As shown in Figure 2.9, if an operating point lies far to the left of the MPP (i.e. E_r is at PB) and $\triangle E_r$ is at ZE (Zero Error), a large duty cycle is required to reach the MPP and hence $\triangle D$ should be PB to reach MPP.

In the defuzzification stage, the output of the fuzzy logic controller is converted from a linguistic

variable to a numerical variable still using a membership function as in Figure 2.11. Defuzzification also provides an analog signal that will control the power converter stage to reach the MPP.

MPPT based on fuzzy logic control shows a good performance under varying environment conditions [Esram and Chapman 2007], however, their effectiveness depends upon the selection of the correct error computation and creating the rule based table. An adaptive based fuzzy logic control which constantly tunes the membership functions and the rule based table in order to obtain an optimum performance has been proposed [Patcharaprakiti and Premrudeepreechacharn 2002]. The experimental results for fuzzy logic by Senjyu and Uezato 1994 [Senjyu and Uezato 1994], shows fast convergence and minimal fluctuation of MPP. Veerachary et. al. [Veerachary *et al.* 2003] shows that two membership functions can be used and hence tracking performance depends on the membership function type.

2.3.7 Neural Network based MPPT

Utilization of a neural network is another method that can be used for implementing MPPT. Such neural networks commonly have three layers. Namely, input, hidden, and output as shown in Figure 2.12 [Hiyama *et al.* 1995] [Ro and Rahman 1998] [Hussein *et al.* 2002] [Sun *et al.* 2002] [Zhang *et al.* 2002]. The number of nodes in each layer are user-dependent and hence may vary. The input variables for a neural network could be the PV array parameters like V_{OC} and I_{SC}; atmospheric data like irradiance and temperature; or any combination of these. The output is generally one or several reference signal(s) like a duty cycle signal used to drive the power converter to operate at or close to the MPP. The closeness of the operating point towards the MPP depends on the algorithm used by the hidden layer and how well the neural network has been trained. As shown in Figure 2.12, the link between nodes i and j is labeled as having a weight of w_{ij}. To accurately identify the MPP, w_{ij} needs to be carefully determined through appropriate training, where the PV array is tested over months or years and the patterns between input(s) and output(s) of the neural network are recorded. A neural network needs to be specifically trained for the PV array with which it will be used according to the array characteristics. Since the array properties change with time, the neural network has to be periodically retrained in order to provide accurate MPPT.

2.3.8 Ripple Correlation Control

A current and voltage, and hence power ripple is observed whenever a power converter is connected to a PV array. RCC uses these ripples to perform MPPT in which the time derivative of the time varying PV array power ($\dot{p}$) is correlated with the time derivative of the time varying

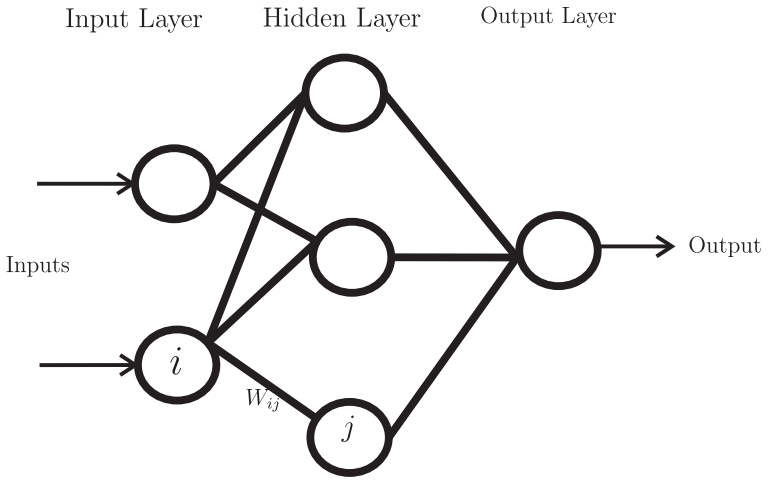

Figure 2.12 Neural Network Example

PV array current or voltage ($\dot{i}$ or $\dot{v}$) in order to drive the power gradient to zero. Referring to Figure 2.9, if v or i is increasing (hence $\dot{i} > 0$ or $\dot{v} > 0$) and p is increasing (hence $\dot{p} > 0$), then the operating point is below the MPP (i.e.$V < V_{MPP}$ and $I < I_{MPP}$). On the other hand, if v or i is increasing and p is decreasing (hence $\dot{p} < 0$), than the operating point is above the MPP (i.e. $V > V_{MPP}$ or $I > I_{MPP}$). Hence, it can be observed that $\dot{p}\dot{v}$ or $\dot{p}\dot{i}$ is positive to the left of the MPP and $\dot{p}\dot{v}$ or $\dot{p}\dot{i}$ is negative to the right of the MPP and zero at the MPP.
For a boost converter, increasing the duty ratio increases inductor current which is same as the PV array current, but decreases the PV array voltage [Midya *et al.* 1996]. The duty cycle control ratios are give by equation 2.11 and equation 2.12.

$$d(t) = -k_3 \int \dot{p}\dot{v}dt \tag{2.11}$$

$$d(t) = k_3 \int \dot{p}\dot{i}dt \tag{2.12}$$

where k_3 is a positive constant. Hence, controlling the duty ratio in this fashion assures that the MPP is continuously tracked, making RCC a true MPP tracker.
The derivatives can be approximated by using high pass filters with a cutoff frequency higher than the ripple frequency. An easy method for obtaining the current derivative for equation 2.12 is to sense the inductor voltage which is proportional to the current derivative. As the time constant of the inductor ripple is much larger than the switching frequency, the core loss and resistance have a negligible effect. RCC can be implemented with simple and inexpensive analog circuits [Midya *et al.* 1996]. Experiments have been performed which showed that RCC quickly tracks the MPP, even under varying irradiance conditions [Midya *et al.* 1996]. The gain of RCC circuit and the switching frequency of power converter limits the time taken by RCC to

converge to MPP. An advantage of RCC is that it does not require any prior information about the PV array hence can be used for different PV array systems.

2.3.9 Load Current or Load Voltage Maximization

When a PV array is connected to a power converter, maximizing the PV array output power also maximizes the power at the load of the converter. Conversely, assuming a lossless system, maximizing power at the converter will maximize the PV array power. Most of the loads encountered in PV system are either voltage- source type, current-source type, resistive type or a combination of these, as shown in the Figure 2.13 [Shmilovitz 2005]. From Figure 2.13, it is clear that for a voltage-source load type, load current (i_{out}) should be maximized in order to reach MPP. While for current-source load type, load voltage (v_{out}) is maximized. For other types of the load, either i_{out} or v_{out} is maximized to reach maximum power. For almost all loads of interest, it is adequate to maximize either load current or load voltage to maximize load power and hence only one sensor needs to be used.
A battery bank is the load encountered most implementation of PV systems, which could be regarded as a constant voltage-source type load and hence the load current can be used as a control variable. Since the power converter is assumed to be lossless, operation at exactly the MPP is never achieved through this method.

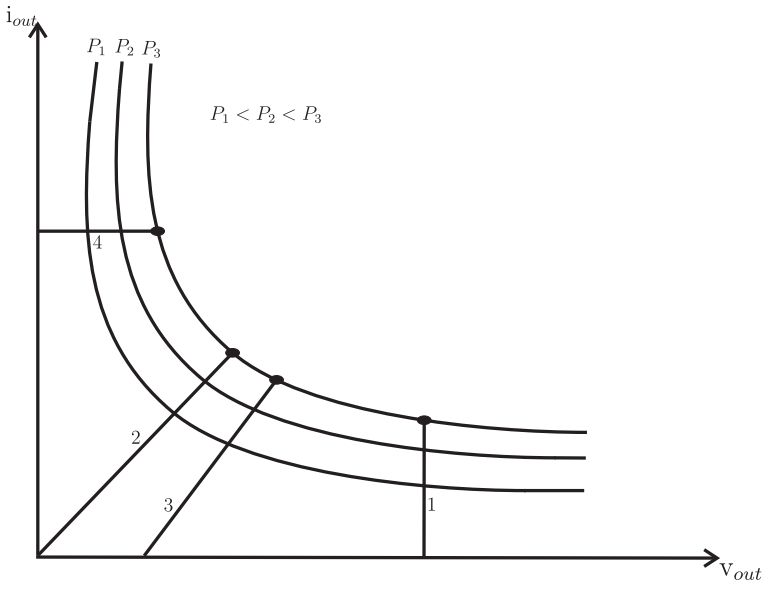

Figure 2.13 Different load types 1:Voltage Source 2:Resistive 3:Resistive and Voltage Source 4: Current Source[Shmilovitz 2005]

2.3.10 dP/dV or dP/dI Feedback Control

A general method for achieving the MPP is to compute the slope (dP/dV or dP/dI) of the power curve and feed this back to the power converter with some control to drive the slope to zero. The derivative dP/dV is computed for a few cycles and its sign stored for the past few cycles, and based on these signs, the duty cycle of the power converter can be either incremented or decremented to reach the MPP [Bhide and Bhat 1992]. A linearization based method could be used to compute dP/dV [Sugimoto and Dong 1997] while sampling and data conversion is done with subsequent digital division of Power and Voltage to approximate dP/dV [Chiang and chang 1998] [Blejis and Gow 2001] [Hou *et al.* 2004]. As such, dP/dI can then be integrated together with an adaptive gain to improve the transient response [Blejis and Gow 2001]. While it is shown the PV array voltage can be periodically incremented or decremented and $\triangle$P/$\triangle$V is compared to the marginal error until the MPP is reached [Hou *et al.* 2004]. It has also been shown that the convergence to the MPP is reached within tens of milliseconds[Chiang and chang 1998].

2.4 MICRO-HYDRO MPPT CONTROLLER

For a run-of-river plant type hydropower station which consequently does not have any significant water reservoir, only a fraction of the available stream flow at a given time is used. In order to allow extended control features when they are integrated into an electric power grid, and to provide enough flexibility to adapt to the specific conditions of rivers with low water flow rate, a variable-speed turbine is proposed in a similar manner to small wind turbines. Thus, by optimizing the turbine working point in order to extract the maximum power of the water flowing per second, superior efficiencies compared to traditional hydro turbines could be obtained. Moreover, by replacing mechanical controls with advance technologies in power electronic devices, higher reliability power generation with better efficiencies could be reached.
If output power is plotted against turbine RPM for a fixed head, then the inverted parabolic type of curve is achieved as obtained for small wind turbines, which will be discussed in Chapter 3. For different values of water flow rate, there always lies a point where maximum power out of the turbine can be obtained. Hence in order to optimize the power, the turbine should be operated at the particular RPM for different values of water flow rate. Measuring water flow rate in the rotor of the hydraulic turbine is difficult and hence in order to avoid using this measurement for determining the optimal rotor speed, an indirect method is usually implemented [Marquez *et al.* 2010]. Adjusting the duty cycle of a DC-DC converter directly in-order to attain optimum rotor speed according to the successive power measurements is proposed for a Micro Hydro Power Plant (MHPP) system [Marquez *et al.* 2010]. P&O (b) iterative method is an efficient method in tracking the MPP for a wide range of water flow rates [Marquez *et al.* 2010]. Since

the principles involved in micro-hydro systems mostly resemble with small wind turbine systems, most of the MPPT algorithms employed for wind turbines could be used for micro-hydro as well.

2.5 CONCLUSION

Different MPPT techniques implemented for WECS, PV and micro-hydro systems are considered in this Chapter. The main focus is on the MPPT techniques that do not require any mechanical sensors for different parameters like wind and rotor speed (for wind turbines), irradiation and temperatures (for PV systems), and water flow and water head (for micro-hydro).

Chapter 3

MODELING OF A SMALL SCALE GENERATING SYSTEM

3.1 MODEL OF A SMALL WIND TURBINE

The power output from a wind turbine depends upon the rotor swept area, velocity of the wind and density of air. The general power equation for a wind turbine is given in equation 3.1.

$$P = 0.5 c_p(\lambda, \beta) \rho_a \pi R^2 V_w^3 \tag{3.1}$$

where, c_p = power coefficient, ρ_a = density of air, R = rotor radius, and V_w = Wind velocity. The power coefficient(c_p) for the wind turbine is defined as the power that could be extracted out of the total available in the wind, which is a function of a blade tip speed ratio (λ) and blade pitch angle (β). Theoretically, a wind turbine can only be, at maximum, 59.3 % efficient (which is also known as Betz's limit). That is, a wind turbine can only convert an absolute maximum of 59.3 % of the total energy available in the wind into useful energy. A turbine which extracts 40 % of the power in the wind is extracting almost two-thirds of the ideal wind turbine power. This could be regarded as an efficient factor considering different aerodynamic constraints such as constantly changing wind speed and direction as well as the frictional losses due to blade surface roughness [Gohnson 2001].
For most small wind turbines, β (angle between the chord of the blade and the reference line on the rotor hub) is kept constant (normally zero). Hence for a constant β, c_p is only a function of λ. The tip speed ratio is defined as a ratio between the speed of the blade tip (V_{tip}) and wind speed (V_w) as shown in equation 3.2. The computation of the power coefficient (c_p) requires the use of blade element theory and the knowledge of blade geometry or the use of real wind turbine characteristics [Gohnson 2001].

$$\lambda = \frac{V_{tip}}{V_w} = \frac{\omega_r R}{V_w} \tag{3.2}$$

where, ω_r is the turbine angular speed.

The dynamic equation of the wind turbine is given by equation 3.3

$$\frac{d\omega_r}{dt} = \frac{T_m - T_L - F\omega_r}{J} \tag{3.3}$$

where, J is the system inertia, F is the viscous friction coefficient, T_m is the torque developed by the turbine and T_L is the torque due to load.
Equation 3.4 is used to model $c_p(\lambda,\beta)$ of the wind turbine [Heier 2006].

$$c_p(\lambda,\beta) = c_1(\frac{c_2}{\lambda_i} - c_3\beta - c_4)e^{\frac{-c_5}{\lambda_i}} + c_6\lambda \tag{3.4}$$

where,λ_i is a variable which is a function of λ, and β is defined as in equation 3.5 [Heier 2006].

$$\frac{1}{\lambda_i} = \frac{1}{\lambda + 0.08\beta} - \frac{0.035}{\beta^3 + 1} \tag{3.5}$$

In equation 3.4, the coefficients c_1 to c_6 are : $c_1 = 0.5176$, $c_2 = 116$, $c_3 = 0.4$, $c_4 = 5$, $c_5 = 21$ and $c_6 = 0.0068$ [Heier 2006].

Using equations from equation 3.1 through to equation 3.5, a wind turbine model is developed in matlab simulink which is shown in Figure 3.1. Different parameters used for the small wind turbine model development is as shown in Table 3.1. The inputs to the model are blade pitch angle (in degrees), wind speed (in m/s) and rotor speed (in rad/s). The blade pitch angle is normally kept at zero as pitch angle control is not standard for small wind turbines but can be assigned to certain value within the model if desired. Power vs rotor speed for different wind velocity is generated which is as shown in Figure 3.2.

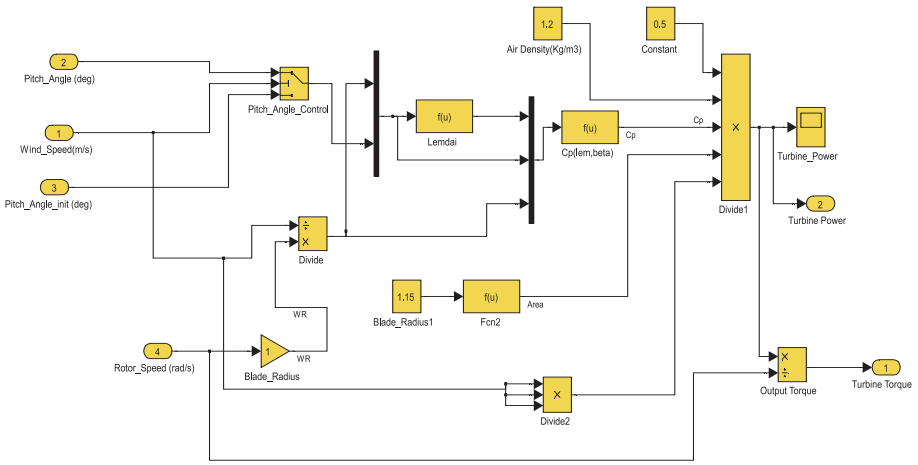

Figure 3.1 Simulink model of the wind turbine

Table 3.1 Different parameters for the small wind turbine model development

Rated Mechanical power (P_m)	1000 Watts
Wind Speed for the rated power (V_w)	10 m/s
Density of air (ρ_a)	1.2kg/m^3
Radius of the blade for the rated power (R)	1.15m
Area swept by the rotor blades (A_w), πR^2	4.16m^2

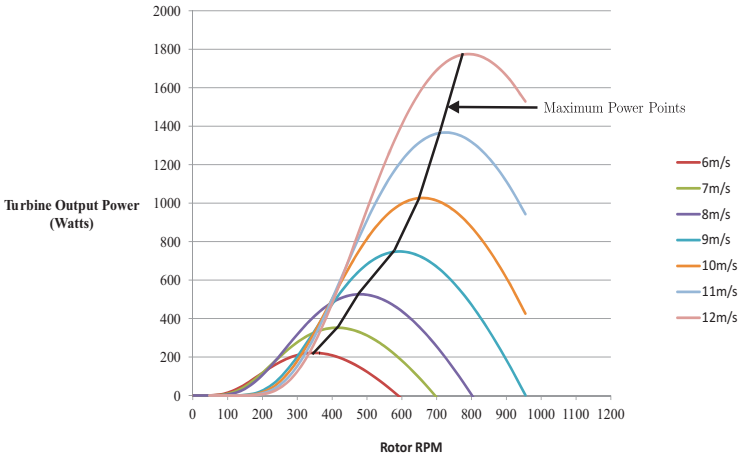

Figure 3.2 Turbine output power versus rotor rpm at different wind speeds

Figure 3.2 shows that for each wind velocity, there is a maximum power that the turbine could extract if operated at a particular (or optimum) rotor speed (ω_{opt}). ω_{opt} is the speed that represents the optimum tip speed ratio (λ_{opt}). In order to obtain maximum possible power, the turbine must be operated at λ_{opt} and this is possible by controlling the turbine rotational speed such that it always operates at the optimum speed.

Using equation 3.1 and equation 3.2, the target power (or the maximum power) out of the wind turbine can be written as in equation 3.6.

$$P_{max} = K_{opt}\omega_{ropt}^3 \tag{3.6}$$

where, K_{opt} is an optimum wind constant given by equation 3.7.

$$K_{opt} = \frac{0.5\pi\rho c_{pmax} R^5}{\lambda_{opt}^3} \tag{3.7}$$

where, c_{pmax} is the maximum power coefficient of the wind turbine at peak power point. Similarly, ω_{opt} is given by equation 3.8.

$$\omega_{opt} = \frac{\lambda_{opt} V_w}{R} \tag{3.8}$$

Hence, the Maximum Power Point Tracking (MPPT) controller tries to run the turbine at the optimum turbine speed (ω_{opt}) for each wind velocity. Reaching the maximum power point depends upon the controller type and its parameters.

3.2 MODEL OF A MICRO-HYDRO SYSTEM

For low water heads and low water flow rates, reaction turbo turbine systems are well suited, which are a propeller type, modified from a Kaplan turbine with neither blade pitch control nor upstream guide vane [Marquez *et al.* 2010]. For a simple and robust design, Permanent Magnet Synchronous Generators (PMSGs) are used as in small wind turbines without any gearbox coupled to the generator.
The general equation for output power available from a hydraulic turbine (P_{hyd}) is given by equation 3.9 [Fang *et al.* 2008].

$$P_{hyd} = \rho_w g H Q \tag{3.9}$$

where, ρ_w is the specific density of water (1000 kg/m^3 at approximately 4^{o}C), g is gravitational acceleration (9.8 m/s^2), H is the water net head (m), and Q is water flow rate or discharge (m^3/s). The potential energy of water is converted into mechanical energy in the turbine as a result of water pressure which applies a force on the runner blades which then decreases as it passes through the reaction turbine. Hydraulic turbine efficiency (η_h) needs to be considered in order to determine the relation between mechanical and hydraulic powers as given in equation 3.10 [Marquez *et al.* 2010].

$$P_m = \eta_h P_{hyd} \tag{3.10}$$

The hydraulic efficiency (η_h) depends highly upon the turbine design and the operating conditions (such as Q, H and angular speed of the turbine rotor (ω)) and thus is very difficult to

determine analytically. An approximate numerical expression used to calculate the mechanical power characteristics of the hydraulic turbine is determined with a relation between turbine efficiency (η_h) as a function of Q and ω as in equation 3.11 [Marquez *et al.* 2010].

$$\eta_h(\tau, Q) = [\frac{1}{2}(\frac{90}{\tau_i} + Q + 0.78)exp(\frac{-50}{\tau_i})](3.33Q) \tag{3.11}$$

In equation 3.11, the value of τ_i is given by equation 3.12.

$$\tau_i = [\frac{1}{\tau + 0.089} - 0.0035]^{-1} \tag{3.12}$$

where, $\tau = \frac{RA\omega}{Q}$, R being the radius of the hydraulic turbine (m), and A is the area swept by the rotor blades (m^2).
Parameters used for the modeling of an example micro-hydro system is given in Table 3.2.

Table 3.2 Different parameters for the micro-hydro model development

Rated Mechanical power (P_m)	350 Watts
Rated water Flow Rate (Q)	120 litre/sec (0.12Kg/m^3)
Average water Head (H)	1.5 m
Density of water (ρ_w)	1000kg/m^3
Acceleration due to Gravity(g)	9.8m/s^2
Radius of the Turbine Blades (R)	0.15m
Area swept by the rotor blades (A)	0.071 m^2

Figure 3.3 illustrates the steady-state mechanical power characteristic function (P_m) versus the rotating-speed (ω) of the hydraulic turbine at various water flow rates (Q) with H fixed at 1.5 m. The point of the optimal efficiency is designed to be at the rated water flow rate and head, where the turbine captures maximum power. It can be observed that for each water flow rate, there exists a specific point in the hydraulic turbine characteristic where the output mechanical power is maximized and is known as the Maximum Power Point (MPP). Thus the control of the turbine rotor results in a variable-speed operating conditions such that the maximum power can be extracted continuously from the water flow. It is also observed that the power versus speed characteristics of a micro-hydro turbine system in Figure 3.3 closely match those of a small wind turbine system of Figure 3.2.

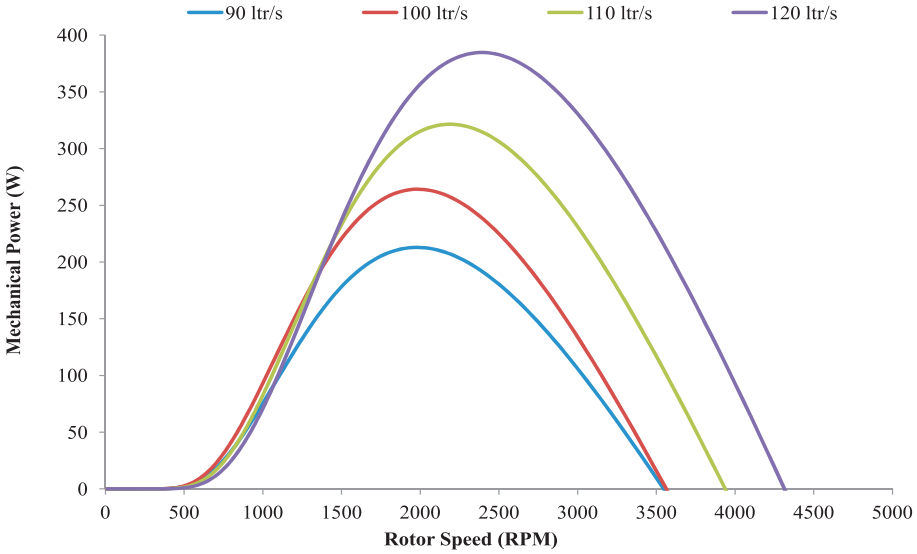

Figure 3.3 Mechanical Power versus rotor speed curves at various water flow rates for a hydraulic turbine

3.3 PERMANENT MAGNET SYNCHRONOUS GENERATOR (PMSG) MODEL

The mathematical model of PMSGs for power system and converter system analysis are usually based on the following assumptions [Krause 2002].

1. The stator windings are positioned sinusoidally along the air-gap as far as the mutual effect with the rotor is concerned.
2. The stator slots cause no appreciable variations of the rotor inductance with rotor position.
3. Magnetic hysteresis and saturation effects are negligible.
4. The stator windings are considered symmetrical.
5. Damping windings are not considered while the capacitance of all the windings is neglected and resistance of the coils are assumed to be constant.

The dynamic model of a PMSG is derived from a two-phase synchronous reference. Namely direct (d) and quadrature (q) axis frame in which the q-axis is 90^o ahead of the d-axis with respect to the direction of rotation. In the case of a balanced three phase system, application of dq transformation reduces the three AC quantities to two DC quantities. Simplified calculations can be performed within these imaginary DC quantities before performing the inverse transform to recover actual three phase quantities. The dq transform applied to the three phase system is as shown by equation 3.13 [Krause 2002]. The inverse transform is given by equation 3.14.

$$\begin{bmatrix} F_d \\ F_q \end{bmatrix} = \frac{2}{3} \begin{bmatrix} sin\omega t & sin(\omega t - \frac{2\pi}{3}) & sin(\omega t + \frac{2\pi}{3}) \\ cos\omega t & cos(\omega t - \frac{2\pi}{3}) & cos(\omega t + \frac{2\pi}{3}) \end{bmatrix} \begin{bmatrix} F_a \\ F_b \\ F_c \end{bmatrix} \tag{3.13}$$

$$\begin{bmatrix} F_a \\ F_b \\ F_c \end{bmatrix} = \begin{bmatrix} sin\omega t & cos\omega t \\ sin(\omega t - \frac{2\pi}{3}) & cos(\omega t - \frac{2\pi}{3}) \\ sin(\omega t + \frac{2\pi}{3}) & cos(\omega t + \frac{2\pi}{3}) \end{bmatrix} \begin{bmatrix} F_d \\ F_q \end{bmatrix} \tag{3.14}$$

The d axis stator current in the frequency domain is represented by equation 3.15 [Krause 2002].

$$i_{ds} = \frac{(-v_{ds} - R_s i_{ds} - \omega_r L_q i_{qs})}{SL_d} \tag{3.15}$$

Similarly, q axis stator current in the frequency domain is represented by equation 3.16 [Krause 2002].

$$i_{qs} = \frac{(-v_{qs} - R_s i_{qs} - \omega_r (L_{ds} + L_{ls}) i_{ds} + \omega_r \phi_r)}{S(L_{ds} + L_{qs})} \tag{3.16}$$

where, v_{ds} and v_{qs} are the d and q axis stator voltages, i_{ds} and i_{qs} are the d and q axis stator currents, R_s is the stator resistance and ω_r is the angular speed of the generator. L_d and L_q are the stator d and q axis self inductances and ϕ_r is the rotor flux. L_d, L_q are given by equation 3.17 and equation 3.18 [Wu *et al.* 2011].

$$L_d = L_{ls} + L_{dm} \tag{3.17}$$

$$L_d = L_{ls} + L_{qm} \tag{3.18}$$

where, L_{dm} and L_{qm} are the magnetizing inductances in the d and q axis, and L_{ls} is the leakage inductance. For a non-salient pole PMSG, d and q axis magnetizing inductances are equal (i.e. $L_{dm} = L_{qm}$) whereas for a salient pole PMSG, d axis magnetizing inductance is normally lower than the q axis magnetizing inductance (i.e. $L_{dm} < L_{qm}$) [Wu *et al.* 2011]. The simplified dq axis model in the rotor-field synchronous frame is as shown in Figure 3.4.

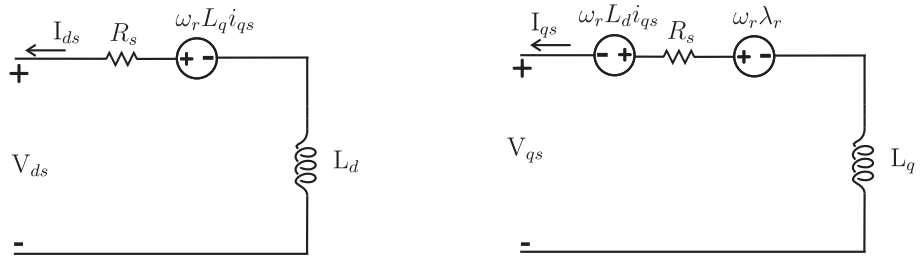

(a) d axis circuit (b) q axis circuit

Figure 3.4 Simplified dq-axis model of PMSG in the rotor field synchronous reference frame

The electromagnetic torque (T_e) and the rotor speed (ω_r) of the PMSG are calculated as shown in equation 3.19 and equation 3.20 respectively [Wu *et al.* 2011].

$$T_e = \frac{3N_{pp}}{2}(\phi_r i_{qs} - (L_d - L_q) i_{ds} i_{qs}) \tag{3.19}$$

where, N_{pp} is the number of pole pairs of the rotor.

$$\omega_r = \frac{N_{pp}}{JS}(T_e - T_m) \tag{3.20}$$

where, J is the rotational inertia of the generator and T_m is the mechanical torque for the generator (in the case of the PMSG connected to a wind turbine, T_m is the torque from the turbine).

Using equations from equation 3.13 through to equation 3.20, a PMSG model has been developed in matlab/simulink as shown in Figure 3.5. Inputs for the model are $d-q$ axis voltages and mechanical torque. Rotor speed (ω_r) as calculated through equation 3.20, is a feedback to the system. Number of pole pairs, d and q axis inductances, leakage inductance, magnetic flux of the rotor magnets, stator resistance and moment of inertia of rotor and load can be initially set for a particular size of the generator. As shown in Figure 3.5, d- axis current (i_{ds}), q-axis current (i_{qs}) and electromagnetic torque (T_e) are the outputs from the system as calculated by equation 3.15, equation 3.16 and equation 3.19 respectively.

3.4 MODEL OF A PHOTO VOLTAIC (PV) ARRAY

The Photovoltaic effect of a semiconductor PN junction can be used to describe the working principle of a PV array [Go *et al.* 2011]. An equivalent circuit of a PV module can be represented as in Figure 3.6(a).

In Figure 3.6(a), I_{pc} is the photocurrent of the PV module under certain solar irradiance and temperature, I_D is the diode current which is given by the classical diode current expression, R_s is the intrinsic resistance (or series resistance) to the current flow and R_{sh} is the parallel (or shunt) resistance. Practically, R_{sh} is very large and hence current through this resistance could be neglected. The final expression for the load current considering I_{sh} can be expressed as in equation 3.21 [Go *et al.* 2011].

$$I = I_{pc} - I_D - I_{sh} = I_{sc} - I_0[exp\frac{V + IR_s}{nV_T} - 1] - \frac{V + IR_s}{R_{sh}} \tag{3.21}$$

where, I is the output terminal current, I_0 is the diode saturation current, V is the terminal voltage of the module, n is the ideal constant of the diode, V_T is the thermal potential of a

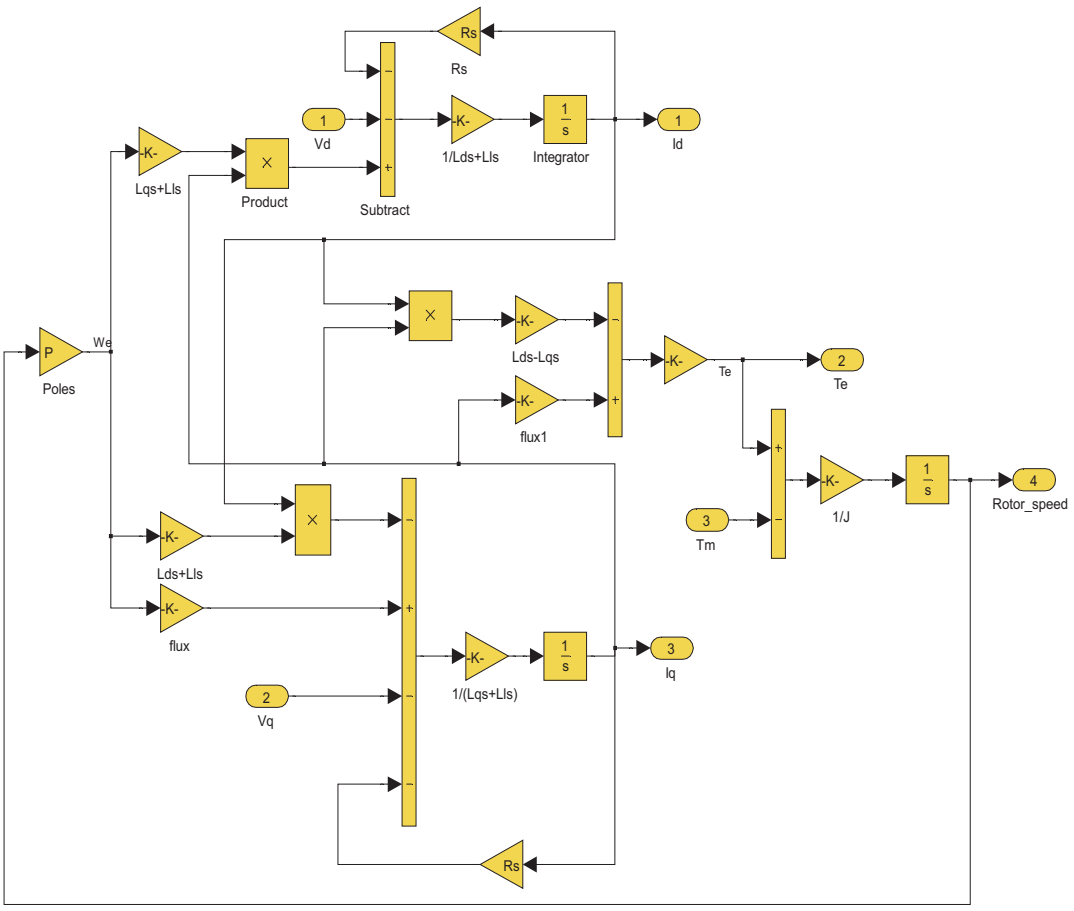

Figure 3.5 PMSG model developed in matlab simulink

module whose value is $m\frac{kT}{q}$, k is Boltzmann's constant, T is the cell temperature in Kelvin, q is the electric charge magnitude of the electron, and m is the number of cells connected in series. The photocurrent mainly depends upon the solar insolation (or irradiation) which can be expressed as in equation 3.22 [Tsai *et al.* 2008].

$$I_{pc} = [I_{sc} + K_i(T_c - T_{ref})]\mu \tag{3.22}$$

where, I_{sc} is the short circuit current at 25 ^0C and 1 kW/m^2, K_i is the cell's short-circuit temperature coefficient, T_{ref} is the cell's reference temperature, and μ is the solar insolation in kW/m^2. The diode saturation current varies with the cell temperature as shown in equation 3.23.

$$I_0 = I_{RS}(\frac{T_c}{T_{ref}})^3 exp[\frac{qE_G(\frac{1}{T_{ref}} - \frac{1}{T_c})}{kA_{PV}} \tag{3.23}$$

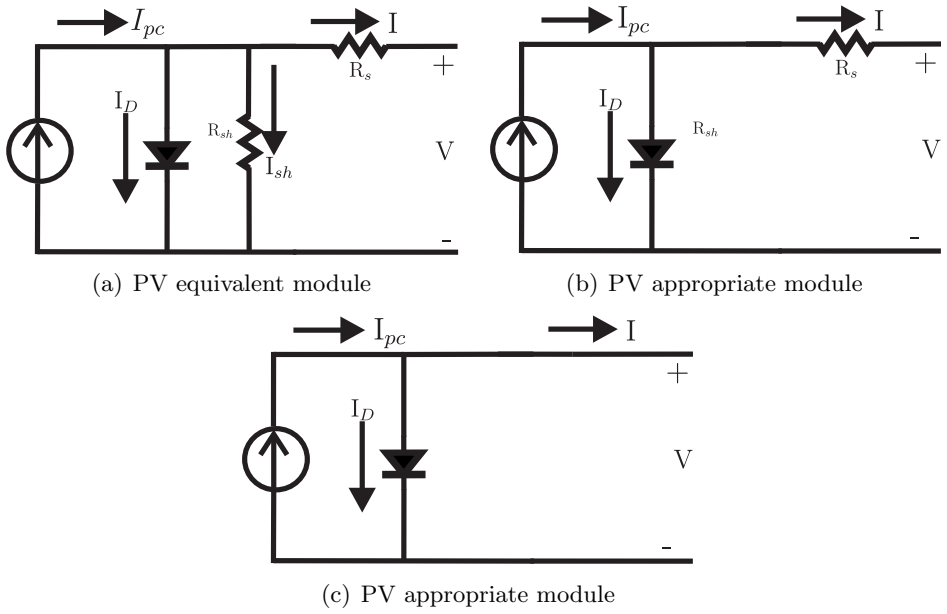

(a) PV equivalent module

(b) PV appropriate module

(c) PV appropriate module

Figure 3.6 Equivalent Circuit Model of PV cell

where, I_{RS} is the cell's reverse saturation current at a reference temperature and a solar radiation, E_G is the band-gap energy of the semiconductor used in the cell, and A_{PV} is the ideal factor which is dependent on the PV technology [Tsai *et al.* 2008].

The shunt resistance (R_{sh}) is inversely proportional with shunt leakage current to ground. In general, the PV efficiency is insensitive to the variation in R_{sh} and hence the shunt- leakage resistance can be assumed to be infinity without any shunt leakage current to ground. On the other hand, a small variation in R_s will significantly affect the PV output power. Hence, an appropriate simplified model of the PV solar cell is as shown in Figure 3.6(b). From the appropriate model of solar as in Figure 3.6(b), equation 3.21 can be written as in equation 3.24 [Hua and Shen 1998].

$$I = I_{pc} - I_s[exp(\frac{q(V + IR_s)}{kT_cA_{PV}}) - 1] \tag{3.24}$$

For an ideal PV module, there is no series loss and leakage to ground i.e. R_s= 0 and $R_{sh} = \infty$. Hence equation 3.24 can be rewritten as in equation 3.25 and the circuit can be simplified as in Figure 3.6(c).

$$I = I_{pc} - I_s[exp(\frac{qV}{kT_cA_{PV}}) - 1] \tag{3.25}$$

3.4.1 Array Module

In order to produce high enough power, individual PV cells need to be connected in series-parallel configurations in a module. An equivalent electrical circuit for a solar array module arranged in N_P parallel and N_S series PV cells is as shown in Figure 3.7(a). The terminal equation in terms of series and parallel arrays can be derived and is given by equation 3.26.

$$I = N_p I_{pc} - N_p I_0 [exp(\frac{q(\frac{V}{N_s} + \frac{IR_s}{N_p})}{KT_c A_{PV}})] - \frac{\frac{N_p V}{N_s} + IR_s}{R_{sh}} \tag{3.26}$$

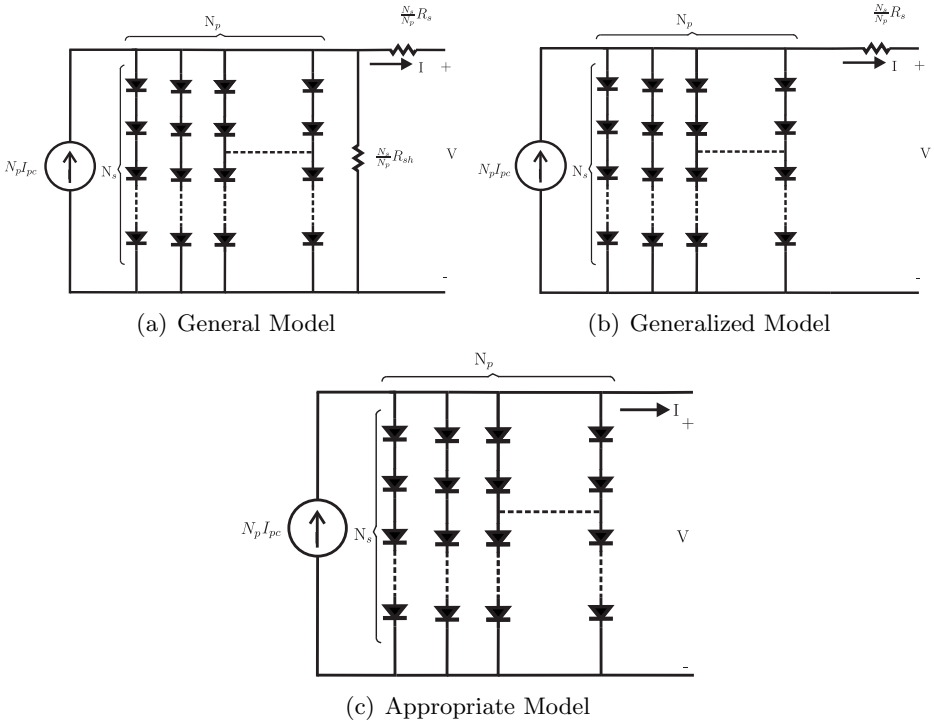

(a) General Model (b) Generalized Model

(c) Appropriate Model

Figure 3.7 Equivalent Circuit Models of Generalized PV

The PV efficiency is quite sensitive to a small change in R_s and is quite insensitive to the change in R_{sh} [Tsai *et al.* 2008]. An appropriate equivalent circuit of the PV model is as shown in Figure 3.7(b), whose mathematical approximation can be expressed as in equation 3.27.

$$I = N_p I_{pc} - N_p I_0 [exp(\frac{q(\frac{V}{N_s} + \frac{IR_s}{N_p})}{KT_c A_{PV}}) - 1] \tag{3.27}$$

Finally, the most simplified model of the generalized PV module is depicted in Figure 3.7(c) and is expressed in equation 3.28.

$$I = N_p I_{pc} - N_p I_0 [exp(\frac{qV}{N_s K T_c A_{PV}}) - 1] \tag{3.28}$$

Generally, the model parameters are determined from the manufacturer's data sheet, two of the most important parameters being the short circuit current, (I_{sc}), and the open circuit voltage (V_{oc}). Since $I_{pc} >> I_0$ and ignoring the ground and diode leakage currents, I_{sc} is approximately equal to I_{pc}. Similarly, V_{oc} is obtained assuming the output current to be zero. Considering V_{oc} at the reference temperature and ignoring the shunt- leakage current, the reverse saturation current (I_{RS}) at the reference temperature can be approximated as given by equation 3.29.

$$I_{RS} = \frac{I_{sc}}{exp(\frac{qV_{oc}}{N_s K A_{PV} T_c}) - 1} \tag{3.29}$$

Hence, using equations from equation 3.21 through to equation 3.29, a solar array model in Matlab-Simulink has been developed as shown in Figure 3.8. The inputs for the model are the cell voltages, solar irradiance and cell temperatures. The model could be modified for any number of series and parallel cells, open circuit voltage and short circuit current, reference temperature, and short circuit temperature coefficient.

Different parameters used for the modeling of the PV arrays are as shown in Table 3.3 which is taken from the MSX 60 PV module.

Table 3.3 Different Solar parameters for the model development

Short Circuit Current (I_{sc})	3.8 Ampere
Open Circuit Voltage (V_{oc})	21.1V
Number of Parallel Cells(N_p)	1
Number of series Cells(N_s)	36
Reference Temperature (T_{ref})	298 Kelvin
Boltzman Constant (K)	1.38X10^{-19}
Ideality Factor (A)	1.3
Electron Charge (q)	1.6X10^{-19}
Short Circuit Temperature Coefficient (K_i)	0.003

The Current-Voltage ($I-V$) and Power-Voltage ($P-V$) characteristics of the PV array are plotted for different values of irradiance as shown in Figure 3.9(a) and Figure 3.9(b) respectively. Figure 3.9(a) shows that the current increases with the increase in the solar irradiance for increased values of the voltage. The current is almost constant for a particular value of the irradiance but decreases abruptly after a particular voltage is reached. If the $P-V$ characteristic is plotted, there is always a point at which the power out of the solar array is maximum for a particular irradiance, which is the MPP and the main aim of the controller is to run the system at this point. The MPP increases with an increase in the solar irradiation. This is because the open-circuit voltage is logarithmically dependent on the solar irradiance and the short circuit current is directly proportional to the solar irradiation.

Similarly, Figure 3.10(a) and Figure 3.10(b) shows $I-V$ and $P-V$ characteristics of the solar array at different temperatures and at reference irradiation (1kW/m^2). The output current increases with the increasing temperature but the MPP decreases. Since the increase in the output current is much less than the decrease in the voltage, the net power decreases at the higher temperature.

3.5 CONCLUSION

In the case of small wind turbines, there is always a MPP for a particular wind velocity which can be determined by adjusting the rotor (or generator) speed such that tip speed ratio (λ) is at its optimum value. The MPP of a PV array can be achieved for a particular solar irradiance and cell temperature by adjusting the output of the cell voltage. For a micro-hydro, the point of an optimal efficiency is achieved for a particular water flow rate and water head by adjusting the rotor (or generator) speed.

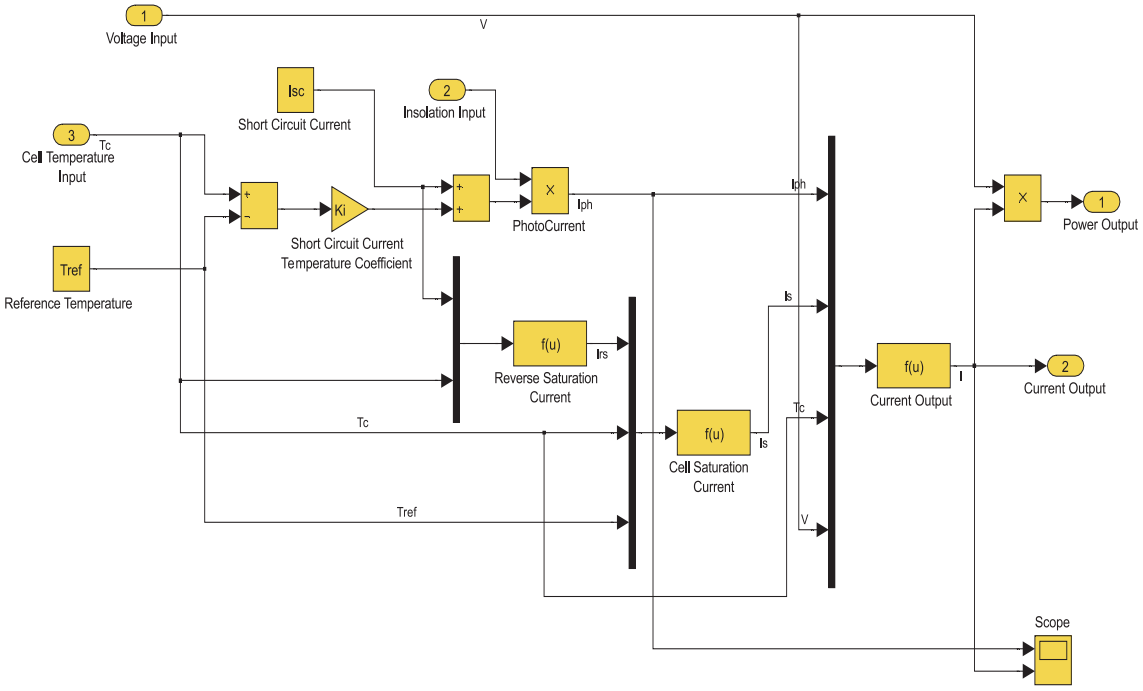

Figure 3.8 PV model implemented in Matlab/Simulink

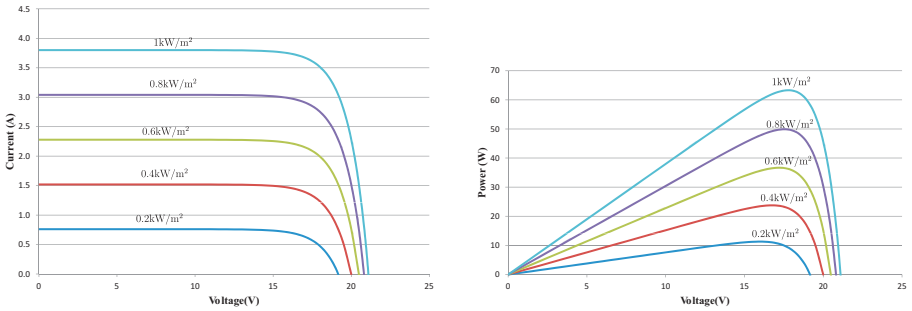

(a) I-V characteristics at different Irradiance

(b) P-V characteristics at different Irradiance

Figure 3.9 (a) I-V and (b) P-V characteristics at different Irradiance and reference temperature

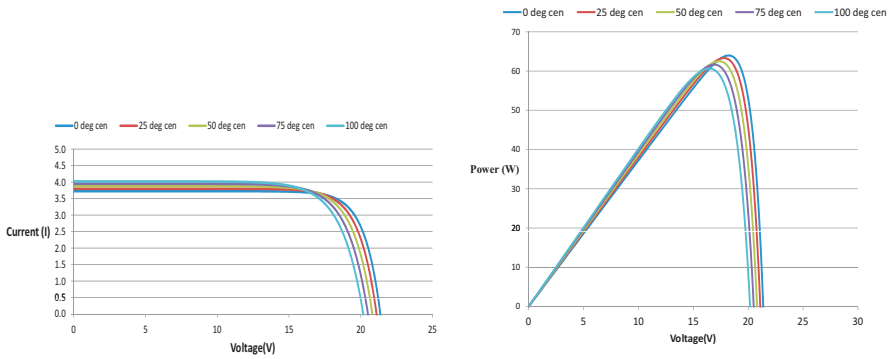

(a) I-V characteristics at different Temperatures

(b) P-V characteristics at different Temperatures

Figure 3.10 (a) I-V and (b) P-V characteristics at different temperatures and reference irradiance

Chapter 4

CONTROLLER THEORY, MODELING AND SIMULATION

The controller should not only track maximum power but also try to operate the system at the highest possible efficiency. Hence, along with the MPPT property, a Power Factor Correction (PFC) boost rectifier section is proposed instead of an uncontrolled rectifier. The general functional block arrangement for the proposed controller system is summarized as in Figure 4.1. The controller is mainly designed for a stand alone system in which a battery bank is used to store the captured energy. Hence, the MPPT controller should charge the battery with maximum power available from the wind Generator (WG-combination of wind turbine and PMSG systems for a given wind speed) whenever the battery voltage is below the rated value, and should keep the battery voltage constant after it reaches the rated value. Initially, the output voltage from the PMSG is boosted up with a three phase Pulse Width Modulation (PWM) boost rectifier in which its output voltage is kept above the battery rated voltage. At this stage, PFC is also achieved along with the stable boosted DC link voltage. A buck DC-DC converter is used in the second stage for implementing the MPPT algorithm as well as charging the battery.

4.1 THREE PHASE BOOST RECTIFIER

A PWM based three phase boost rectifier is proposed that provides dc bus voltage stabilization and can also act as an active line conditioner (ALC) that compensates harmonics and reactive

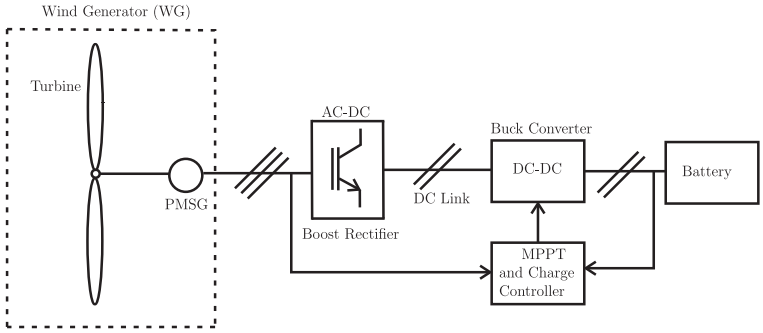

Figure 4.1 Basic Block Diagram of the controller

power to achieve Unity Power Factor (UPF). Two strategies are normally used for PWM based boost rectifiers. Namely, Voltage Oriented Control (VOC) and Direct Power Control (DPC) [Trzynadlowski]. The name 'boost' indicates that the output dc voltage is always greater than that of the corresponding diode bridge rectifier output. This boost property also allows higher values of output DC voltage without the necessity of step-up transformer at the rectifier's ac input side, or the need of a buck/boost converter at the rectifier's DC output side.

Different control techniques used in PWM boost rectifiers are summarized in Figure 4.2. In VOC, UPF is achieved when the line current vector $I = I_\alpha + I_\beta$ is aligned with the phase voltage vector, $V = V_\alpha + V_\beta$ of the power line supplying the rectifier [Trzynadlowski]. In this technique, the revolving reference frame aligned with V is used, and the reference value I_q^* of the quadrature component of I is set to zero to achieve UPF. I_q is achieved by using a rotating coordinate transformation as explained in section 3.3.

Compared to VOC, DPC does not require rotating coordinate transformation or modulation strategies. DPC is based upon the active and reactive power control loops in which the converter switching states are selected by a switching table based on the instantaneous errors between commanded and estimated active and reactive powers [Trzynadlowski].
There are two types of DPC strategy for PWM rectifiers. Namely Voltage based Direct Power Control (V-DPC) and Virtual Flux based Direct Power Control (VF-DPC). In V-DPC, the real and reactive powers (P and Q) drawn from the power line are calculated using the information from a dc link voltage, rectifier switching states, and the line currents (I_a,I_b and I_c). Whereas in the VF-DPC, the line voltages are estimated as the sum of the rectifier input voltage and voltage drop across line reactors.
In order to calculate the real power for MPPT operation within buck converter, V-DPC is chosen such that less mathematical computation within micro-controller is required. The basic config-

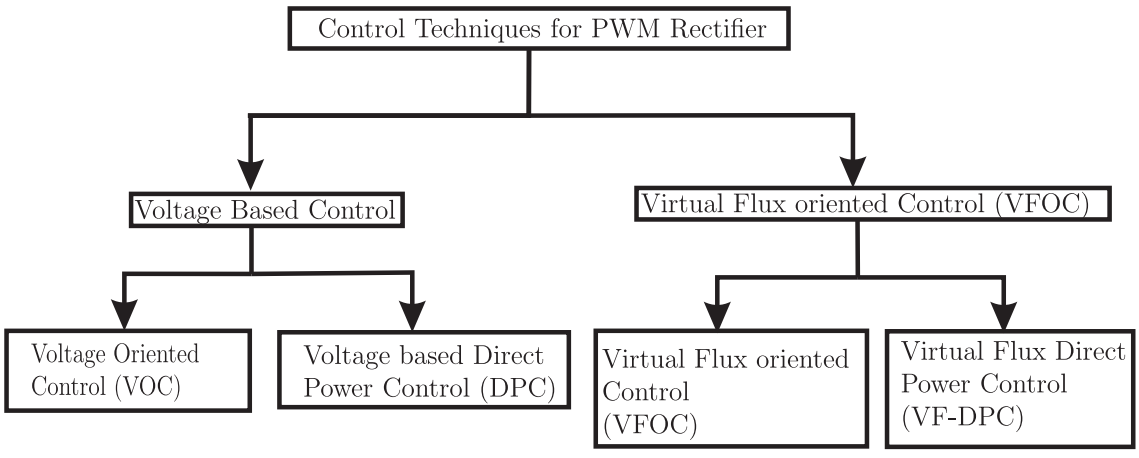

Figure 4.2 Four Control Techniques of the PWM Rectifier

uration for three phase V-DPC PWM rectifiers is as shown in Figure 4.3. The dc bus voltage is regulated by adjusting the active power, and UPF is achieved by controlling the reactive power to be zero. The active power reference (P_{ref}) command is provided from the outer Proportional Integral (PI) controller of the dc bus voltage. The reference reactive power command (Q_{ref}) is normally set to zero for UPF. Errors between reference and estimated feedback powers are the inputs for the hysteresis comparators and digitized to the signals d_p and d_q. The phase of the power source voltage vector is converted into a digitized signal and for this purpose, the stationary coordinates are divided into 12 sectors as shown in Figure 4.5 which is proposed initially by Noguchi [Noguchi *et al.* 2002b].

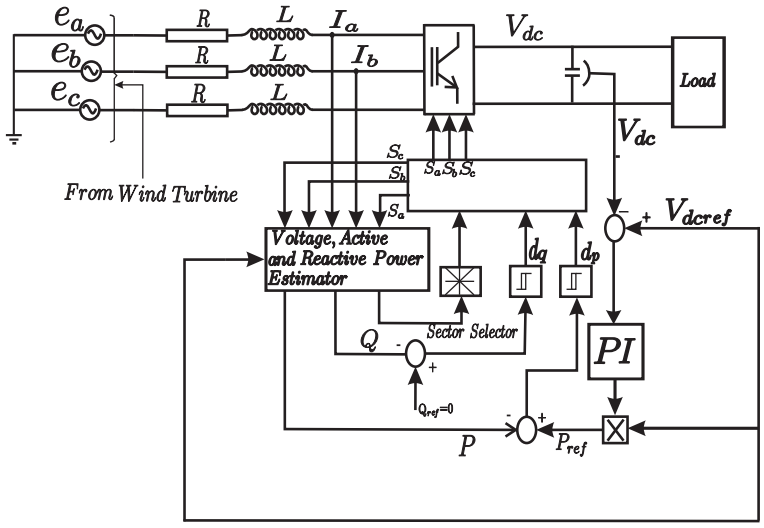

Figure 4.3 configuration of DPC for three phase PWM Rectifier

4.1.1 Active and Reactive Power Calculation

An analogous equation for a vector $\vec{S}$ of a complex power is as given by equation 4.1 [Trzynadlowski].

$$\vec{S} = \frac{2}{3}\vec{E}\vec{I}^{*} = P + jQ \tag{4.1}$$

where, $\vec{E}$ and $\vec{I}$ are the rms source voltage and current. P and Q are instantaneous values of real and reactive powers. $\vec{I}^{*}$ is the conjugate of $\vec{I}$ which can be represented by a two phase system (real and complex). Using Clarke transformation and considering a three phase balance system, abc (three phase) coordinates can be transferred to $\alpha\beta$ (two phase) coordinates as given by equation 4.2 and equation 4.3 for three phase balanced currents and voltages.

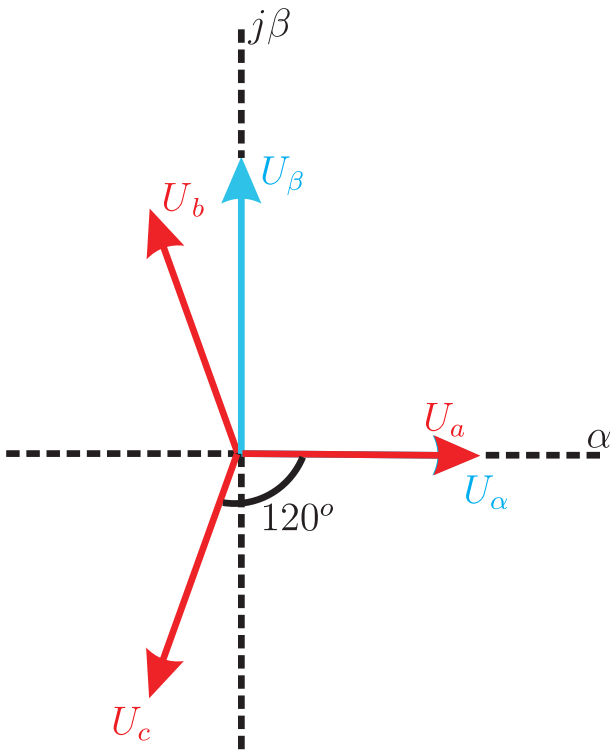

Figure 4.4 Three-phase and two-phase stationary reference frames

$$\begin{bmatrix} I_\alpha \\ I_\beta \end{bmatrix} = \begin{bmatrix} 1 & -0.5 & -0.5 \\ 0 & \frac{\sqrt{3}}{2} & -\frac{\sqrt{3}}{2} \end{bmatrix} \begin{bmatrix} I_a \\ I_b \\ I_c \end{bmatrix} \tag{4.2}$$

$$\begin{bmatrix} E_\alpha \\ E_\beta \end{bmatrix} = \sqrt{\frac{2}{3}} \begin{bmatrix} 1 & -0.5 & -0.5 \\ 0 & \frac{\sqrt{3}}{2} & -\frac{\sqrt{3}}{2} \end{bmatrix} \begin{bmatrix} E_a \\ E_b \\ E_c \end{bmatrix} \tag{4.3}$$

where E_a, E_b, E_c and I_a, I_b, I_c are three phase voltages and currents respectively. E_α,E_β and I_α,I_β are the two phase stationary representation of three phase voltages and currents respectively.

Replacing $\vec{E}$ by (E_α+jE_β) and $\vec{I}^*$ by (I_α-jI_β) in equation 4.2 yields equation 4.4.

$$\vec{S} = \frac{2}{3}(E_\alpha I_\alpha + E_\beta I_\beta) + \frac{2}{3}j(E_\beta I_\alpha - E_\alpha I_\beta) \tag{4.4}$$

Hence, active and reactive powers can be expressed from equation 4.4 as in equation 4.5 and equation 4.6.

$$P = \frac{2}{3}(E_\alpha I_\alpha + E_\beta I_\beta) \tag{4.5}$$

$$Q = \frac{2}{3}(E_\beta I_\alpha - E_\alpha I_\beta) \tag{4.6}$$

Using abc to $\alpha\beta$ transformation, the instantaneous active and reactive powers can also be expressed as in equation 4.7 and equation 4.8.

$$P = E_a I_a + E_b I_a + E_c I_c \tag{4.7}$$

$$Q = E_{bc} I_a + E_{ca} I_b + E_{bc} I_c \tag{4.8}$$

where, E_{ab}, E_{bc} and E_{ca} are three phase line to line voltages. Real and reactive powers could also be estimated without any voltage sensors and is known as voltage sensor-less control which is given as in equation 4.9 and equation 4.10 [Noguchi *et al.* 2002b].

$$P = L(\frac{dI_a}{dt} I_a + \frac{dI_b}{dt} I_b + \frac{dI_c}{dt} I_c) + V_{DC}(S_a I_a + S_b I_b + S_c I_c) \tag{4.9}$$

$$Q = \sqrt{3}(L\frac{dI_a}{dt} I_c - \frac{dI_c}{dt} I_a) - V_{DC}[S_a(I_b - I_c) + S_b(I_c - I_a) + S_c(I_a - I_b)] \tag{4.10}$$

Where, L is the line inductance as in Figure 4.3, S_a, S_b and S_c are switching states of each phases of the converter. V_{DC} is a DC bus voltage. Line resistance (R) also needs to be considered while estimating active power, but practically it is neglected assuming that the power dissipated in this resistance is much lower than the active power associated with the dc bus and inductance of the reactors.

E_α and E_β could be estimated using the values of P, Q, I_α and I_β and can be given as in equation 4.11 below.

$$\begin{bmatrix} E_\alpha \\ E_\beta \end{bmatrix} = \frac{1}{I_\alpha^2 + I_\beta^2} \begin{bmatrix} I_\alpha & -I_\beta \\ I_\beta & I_\alpha \end{bmatrix} \begin{bmatrix} P \\ Q \end{bmatrix} \tag{4.11}$$

Finally, voltages E_a, E_b, E_c can be estimated using the Reverse Park transformation as in equation 4.12.

$$\begin{bmatrix} E_a \\ E_b \\ E_c \end{bmatrix} = \begin{bmatrix} 1 & 0 \\ -\frac{1}{2} & \frac{\sqrt{3}}{2} \\ -\frac{1}{2} & -\frac{\sqrt{3}}{2} \end{bmatrix} \begin{bmatrix} E_\alpha \\ E_\beta \end{bmatrix} \tag{4.12}$$

4.1.2 Switching Algorithm Development for a three phase Boost Rectifier

In a balanced three phase system, the line currents in a stationary $\alpha - \beta$ reference frame are represented as in equation 4.13 and equation 4.14.

$$\frac{dI_\alpha}{dt} = \frac{1}{L}(E_\alpha - V_\alpha - RI_\alpha) \tag{4.13}$$

$$\frac{dI_\beta}{dt} = \frac{1}{L}(E_\beta - V_\beta - RI_\beta) \tag{4.14}$$

where, V_α and V_β are rectifier voltage vector in stationary $\alpha - \beta$ reference frame. Line current vectors I_α and I_β are controlled by selecting the proper rectifier voltage vectors. Practically, parameter R is neglected as mentioned in the previous section and hence discrete first order approximations of equation 4.13 and equation 4.14 are adopted, and the change in line current is calculated as in equation 4.15 and equation 4.16.

$$\triangle I_\alpha = I_\alpha(K+1) - I_\alpha(K) = \frac{T_s}{L}[E_\alpha(K) - V_\alpha(K)] \tag{4.15}$$

$$\triangle I_\beta = I_\beta(K+1) - I_\beta(K) = \frac{T_s}{L}[E_\beta(K) - V_\beta(K)] \tag{4.16}$$

where, K and T_s are the iteration period and the sampling time respectively. The instantaneous active and reactive power can be represented as in equation 4.17 below.

$$\begin{bmatrix} P \\ Q \end{bmatrix} = \begin{bmatrix} E_\alpha & E_\beta \\ E_\beta & -E_\alpha \end{bmatrix} \begin{bmatrix} I_\alpha \\ I_\beta \end{bmatrix} \tag{4.17}$$

For high switching frequency, the change in the power-source voltage can be neglected and hence the change in the active and reactive power for next control cycle is as given in equation 4.18 and equation 4.19.

$$\triangle P = E_\alpha \triangle I_\alpha + E_\beta \triangle I_\beta \tag{4.18}$$

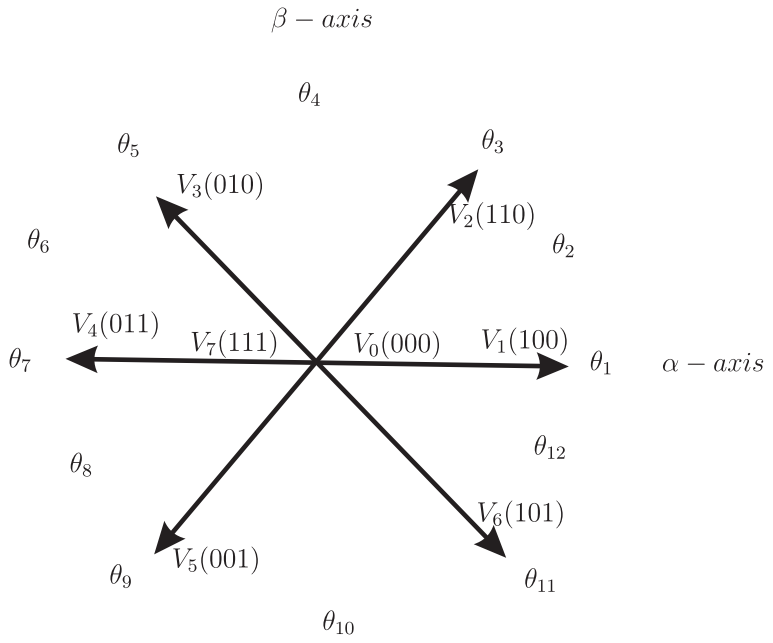

Figure 4.5 Sectors in stationary coordinates and Rectifier Voltage Vectors

$$\triangle Q = E_\beta(K)\triangle I_\alpha - E_\alpha(K)\triangle I_\beta \tag{4.19}$$

By putting values of $\triangle I_\alpha$ and $\triangle I_\beta$ from equation 4.15 and equation 4.16 respectively into equation 4.19 yields equation 4.20 and equation 4.21 respectively.

$$\triangle P = \frac{T_s}{L}[(E_\alpha^2(K) + E_\beta^2(K)) - (E_\alpha(K)V_\alpha(K) + E_\beta(K)V_\beta(K))] \tag{4.20}$$

$$\triangle Q = \frac{T_s}{L}[E_\alpha(K)V_\beta(K) - E_\beta(K)V_\alpha(K)] \tag{4.21}$$

Hence, for controlling the instantaneous active and reactive powers, there are basically six non-zero vectors and two zero vectors as shown in Figure 4.5. For eight states of the rectifier, there are eight different ways of selecting the corresponding switching states which controls the evolution of active and reactive power and are given by the expressions as in equation 4.22 and equation 4.23.

$$\triangle p_i = \frac{t_s}{L}[(e_\alpha^2 + e_\beta^2) - (e_\alpha V_{\alpha i} + e_\beta(k)v_{\beta i})] \tag{4.22}$$

$$\triangle q_i = \frac{t_s}{L}[v_\alpha v_{\beta i} - v_\beta(K)v_{\alpha i}] \tag{4.23}$$

where, i = 0,1,2,....,7.

The voltage vectors in $\alpha - \beta$ coordinate system can be represented as in equation 4.24.

$$E_{\alpha\beta} = \begin{bmatrix} E_\alpha \\ E_\beta \end{bmatrix} = \sqrt{\frac{2}{3}} \begin{bmatrix} 1 & -0.5 & -0.5 \\ 0 & \frac{\sqrt{3}}{2} & -\frac{\sqrt{3}}{2} \end{bmatrix} \begin{bmatrix} E_a \\ E_b \\ E_c \end{bmatrix} \tag{4.24}$$

The vectors E_α and E_β are represented as in equation 4.25 in terms of RMS value of line voltage.

$$E_{\alpha\beta} = \begin{bmatrix} E_\alpha \\ E_\beta \end{bmatrix} = \begin{bmatrix} Ecos\theta \\ Esin\theta \end{bmatrix} \tag{4.25}$$

where, E is the RMS value of line power source voltage and θ is the angular position of voltage source vector in the $\alpha - \beta$ coordinate system which is defined as in equation 4.26.

$$\theta = tan^{-}[\frac{e_\beta}{e_\alpha}]; 0 \leq \theta \leq 2\pi \tag{4.26}$$

For rectifier voltage vector 'V', space vector representation of the seven converter switching states and its corresponding V_α and V_β component values are as shown in Table 4.1

Table 4.1 Rectifier Voltage Space Vectors

V_i	V_{sa}	V_{sb}	V_{sc}	$V_{s\alpha}$	$V_{s\beta}$
0	0	0	0	0	0
1	$\frac{2}{3}V_{dc}$	$-\frac{1}{3}V_{DC}$	$-\frac{1}{3}V_{DC}$	$\sqrt{\frac{2}{3}V_{DC}}$	0
2	$\frac{1}{3}V_{dc}$	$\frac{1}{3}V_{DC}$	$\frac{2}{3}V_{DC}$	$\frac{1}{\sqrt{6}}V_{DC}$	$\frac{1}{\sqrt{2}}V_{DC}$
3	$-\frac{1}{3}V_{DC}$	$\frac{2}{3}V_{DC}$	$-\frac{1}{3}V_{DC}$	$-\frac{1}{\sqrt{6}}V_{DC}$	$\frac{1}{\sqrt{2}}V_{DC}$
4	$-\frac{2}{3}V_{DC}$	$\frac{1}{3}V_{DC}$	$\frac{1}{3}V_{DC}$	$-\sqrt{\frac{2}{3}V_{DC}}$	0
5	$-\frac{1}{3}V_{DC}$	$-\frac{1}{3}V_{DC}$	$\frac{2}{3}V_{DC}$	$-\frac{1}{\sqrt{6}}V_{DC}$	$-\frac{1}{\sqrt{2}}V_{DC}$
6	$\frac{1}{3}V_{DC}$	$-\frac{2}{3}V_{DC}$	$\frac{1}{3}V_{DC}$	$\frac{1}{\sqrt{6}}V_{DC}$	$\frac{1}{\sqrt{2}}V_{DC}$

The rectifier voltage in the $\alpha - \beta$ plane is given as in equation 4.27.

$$|V_{\alpha\beta}| = \sqrt{\frac{2}{3}}V_{dc} \tag{4.27}$$

The normalized value of the change in active power ($\bar{\triangle P_i}$) is derived from equation 4.22 and equation 4.25 and is written in equation 4.28.

$$\bar{\triangle P_i} = \frac{\triangle P_i}{\frac{T_s}{L}|E_{\alpha\beta}||V_{\alpha\beta}|} \tag{4.28}$$

Finally,from equation 4.25 and equation 4.28, the normalized value of active power in terms of the rectifier voltage vector is obtained as in equation 4.29.

$$\bar{\triangle P_i} = \frac{|E_{\alpha\beta}}{|V_{\alpha\beta}|} - [cos\theta \bar{V_{\alpha i}} + sin\theta \bar{V_{\beta i}} \tag{4.29}$$

Similarly, the change in normalized reactive power ($\bar{\triangle Q_i}$) deduced from equation 4.23 and equation 4.25 is written in equation 4.30.

$$\bar{\triangle Q_i} = \frac{\triangle Q_i}{\frac{T_s}{L}|V_{\alpha\beta}||V_{s\alpha\beta}|} \tag{4.30}$$

Hence, from equation 4.25 and equation 4.30, the normalized value of reactive power can be obtained as in equation 4.31.

$$\bar{\triangle Q_i} = cos\theta \bar{V_{\beta i}} - sin\theta \bar{V_{\alpha i}} \tag{4.31}$$

From equation 4.29 and equation 4.31 respectively, it can be seen that the change in reactive power has a sinusoidal waveform whereas change in the active power has a shifted magnitude sinusoidal waveform .

In order to ensure the smooth control of the instantaneous active and reactive power during each sector, the best rectifier voltage is selected among the eight possible states. The rectifier voltage vectors among eight different states are selected according to the voltage vector position and change in active and reactive powers during each sector. The commands of reference reactive power Q_{ref} (set to zero for UPF) and active power P_{ref} (delivered from the outer PI-DC voltage controller) are compared with estimated Q and P values in the reactive and active power hysteresis controller respectively. The digitized output signal of the active power is defined as in equation 4.32.

$$d_P = 1 for P < P_{ref} - H_P \tag{4.32a}$$

$$d_P = 0 for P > P_{ref} - H_P \tag{4.32b}$$

where, H_P is the hysteresis control band for the active power.

Similarly, the digitized output signal of reactive power controller is defined as in equation 4.33.

$$d_Q = 1 for Q < Q_{ref} - H_Q \tag{4.33a}$$

$$d_Q = 0 for Q > Q_{ref} - H_Q \tag{4.33b}$$

where, H_Q is the hysteresis control band for the reactive power.

Hence according to the digitized variables d_P, d_Q and the voltage vector position, appropriate switching states are generated through look up table which is as given in Table 4.2. This is also known as a classical table and was initially proposed by Noguchi [Noguchi *et al.* 2002b].

Table 4.2 Rectifier Voltage Space Vectors

d_P	d_Q	θ_1	θ_2	θ_3	θ_4	θ_5	θ_6	θ_7	θ_8	θ_9	θ_{10}	θ_{11}	θ_{12}
0	0	V_2	V_1	V_1	V_6	V_6	V_5	V_5	V_4	V_4	V_3	V_3	V_2
0	1	V_3	V_2	V_2	V_1	V_1	V_6	V_6	V_5	V_5	V_4	V_4	V_3
1	0	V_0	V_1	V_7	V_6	V_0	V_5	V_7	V_4	V_0	V_3	V_7	V_2
1	1	V_0	V_0	V_7	V_7	V_0	V_0	V_7	V_7	V_0	V_0	V_7	V_7

where, V_0 = 000, V_1 = 100, V_2 = 110, V_3 = 010 , V_4 = 011 , V_5 = 001 , V_6 = 101 , V_7 = 111. Each switching state represents the top switch of the three phase rectifier. For example, for V_1 = 100, the top switch connected to phase A is 'ON' and other top switches which are connected to other 2 phases (B and C) are turned 'OFF'. For this case, the bottom switch connected to phase A is 'OFF' while bottom switch connected to phase B and C are turned 'ON'.

4.2 MAXIMUM POWER POINT TRACKING CONTROLLER

The MPPT controller is designed and selected such that it does not require any mechanical sensors for sensing physical parameters like wind speed and rotor speed. The MPPT controller is implemented with a buck DC-DC converter. The proposed MPPT is based on directly adjusting the converter duty cycle according to the result of the comparison of successive PMSG output power measurements. The same measurement of the active power as in the boost rectifier is used which reduces the computation time in the micro-controller. A steepest ascent method as given by equation 4.34 is employed for maximizing the output power from the WG as proposed by Koutroulis and Kalaitzakis [Koutroulis and Kalaitzakis 2006].

$$D_k = D_{k-1} + C_1 \frac{\triangle P_{k-1}}{\triangle D_{k-1}} \tag{4.34}$$

Where, D_k and D_{k-1} are duty cycle values at iterations k and k-1 respectively; $\frac{\triangle P_{k-1}}{\triangle D_{k-1}}$ is the PMSG power gradient at k-1 and C_1 is the step change in control variable (in this case duty cycle). For the power versus rotor speed curve as shown in Figure 4.6, there always lies an optimum rotor speed point for a particular wind velocity. Hence, this optimum rotor speed is the target rotor speed at which maximum power is produced. At the point of maximum power, equation 4.35 should hold true.

$$\frac{dP}{d\omega} = 0 \tag{4.35}$$

where dP and $d\omega$ are change in power and change in rotor speed respectively.
Applying the chain rule, equation 4.35 can be written as in equation 4.36.

$$\frac{dP}{d\omega} = \frac{dP}{d\omega}\frac{dD}{dV_{PMSG}}\frac{V_{PMSG}}{d\omega_e}\frac{d\omega_e}{d\omega} = 0 \tag{4.36}$$

where, D is the duty ratio of the converter, V_{WG} is the rms voltage out of a wind generator. ω_e is the generator- phase voltage angular speed. For a buck converter, input voltage is related to the output voltage by equation 4.37.

$$D = \frac{V_0}{V_{DC}} \tag{4.37}$$

where, D is the converter duty cycle, V_0 is the converter output voltage and V_{DC} is input voltage for buck converter (or the voltage out of the boost rectifier). Differentiating both side of equation 4.4, 4.38 could be achieved.

$$\frac{dD}{dV_{DC}} = \frac{1}{V^2}V_0 \neq 0 \tag{4.38}$$

Similarly, the wind-turbine rotor speed is related to the generator phase voltage speed by equation 4.39.

$$\frac{d\omega_e}{d\omega} = N_{pp} > 0 \tag{4.39}$$

where, Npp is the generator number of pole pairs, ω_e and ω are generator electrical and mechanical speeds in rad/s respectively. Normally, rectifier output voltage (V_{DC}) is proportional to the generator phase voltage. Phase voltage changes with the rotor speed and hence equation 4.40 is greater than zero.

$$\frac{dV_{ph}}{d\omega_e} > 0 \tag{4.40}$$

From equation 4.40, $\frac{dV_{WG}}{d\omega_e} > 0$ but since output voltage is boosted and kept almost constant, hence there might not be a significant change in V_{DC}. However,even while keeping the output voltage from the boost rectifier constant, the active power can be varied by varying the output load of the buck converter as will be shown by the simulation results as shown in Figure 4.16. This implies that varying the load (or the duty ratio) could vary the active power demand from the WG and hence equation 4.41 could be determined.

$$\frac{dP}{d\omega} = 0 \implies \frac{dP}{dD} = 0 \tag{4.41}$$

Equation 4.41 implies that function ($P(D)$) always has a single extremum point which coincides with the WG MPP. Hence, adjusting the converter duty cycle according to the control equation 4.34 converges WG towards MPP.
The duty cycle adjustment follows the direction of dP/dD. As shown in Figure 4.6, the duty cycle(D) value is increased at the high speed side of the generator, resulting in rotor speed reduction and hence power is increased untill MPP is reached. Similarly, on the low speed side of the generator, D is decreased resulting in higher generator speed and finally reaching MPP. A summary of the MPP tracking process is as shown in Figure 4.6.

In order to reduce the dependency of sensor accuracy on the generated power, a control equation 4.42 is proposed [Koutroulis and Kalaitzakis 2006] . It is based upon incremental WG power measurements rather than absolute measurements.

$$D_k = D_{k-1} + \triangle D_{k-1} \tag{4.42a}$$
$$\triangle D_{k-1} = C_2 sign(\triangle D_{k-2} sign(P_{in,k-1} - P_{in,k-2}) \tag{4.42b}$$

where, $\triangle D_{k-1}$ is the duty cycle change at step $k-1$; $P_{in,k-1}$ and $P_{in,k-2}$ are the converter input-power at steps k-1 and k-2 respectively. C_2 is a constant determining the speed and accuracy of the convergence towards MPP. The function sign(x) is defined as in equation 4.43.

$$sign(x) = 1, if x \geq 0 \tag{4.43a}$$
$$sign(x) = -1, if x < 0 \tag{4.43b}$$

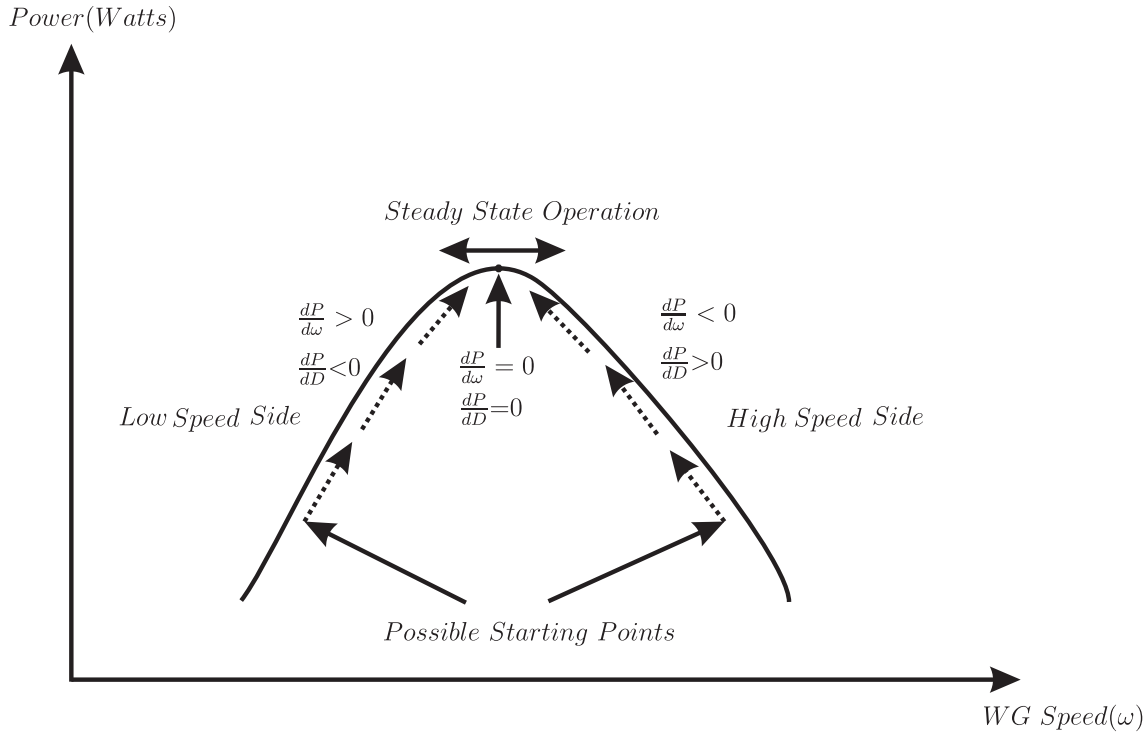

Figure 4.6 MPP Tracking Process

The reference duty cycle (and hence reference generator speed) is sampled at the same frequency as the sample power. If magnitude of $\triangle P(k)$ is within some small band (P_{band}), then the reference speed is not changed, otherwise D(k) is changed by $\triangle D_{k-1}$ as given by equation 4.42. The general algorithm for the proposed MPPT controller is summarized as in Figure 4.7.

Initially, the buck converter is switched at low duty cycle (i.e. low turn 'ON' time, around D=0.1). In the next sample, D is increased by some amount such that there is change in power which can be sensed by the sensors. The power for these two values of duty cycles are computed and further action is taken according to the algorithm as in Figure 4.7.

4.2.1 Buck Converter for MPPT implementation

A buck converter proposed for the MPPT implementation is as shown in Figure 4.8 which is a positive voltage to positive voltage buck in which the output voltage has a same polarity as input.

In the buck configuration as shown in Figure 4.8, when the switch is 'ON', energy is delivered to the inductor through switch (S1). Some of the energy also passes through the output. When S1 is 'OFF', energy stored in the inductor passes to the output via freewheeling diode and none of it comes from the input source. Since the average current from the capacitor is zero, the

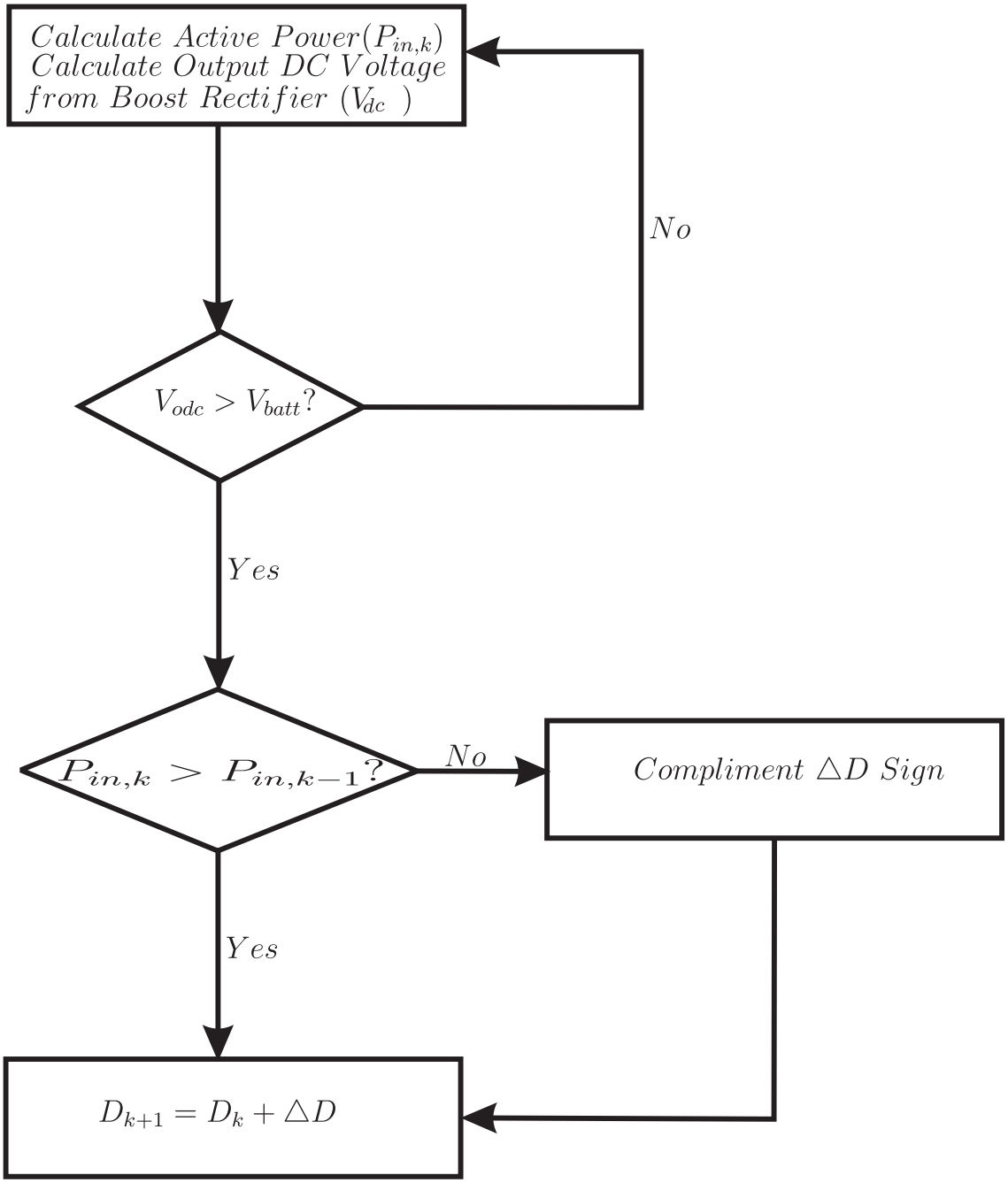

Figure 4.7 MPP Tracking Process

average inductor current from buck converter is equal to the load current.

From Figure 4.8 the voltage across the inductor during 'ON' and 'OFF' time is as given by equation 4.44.

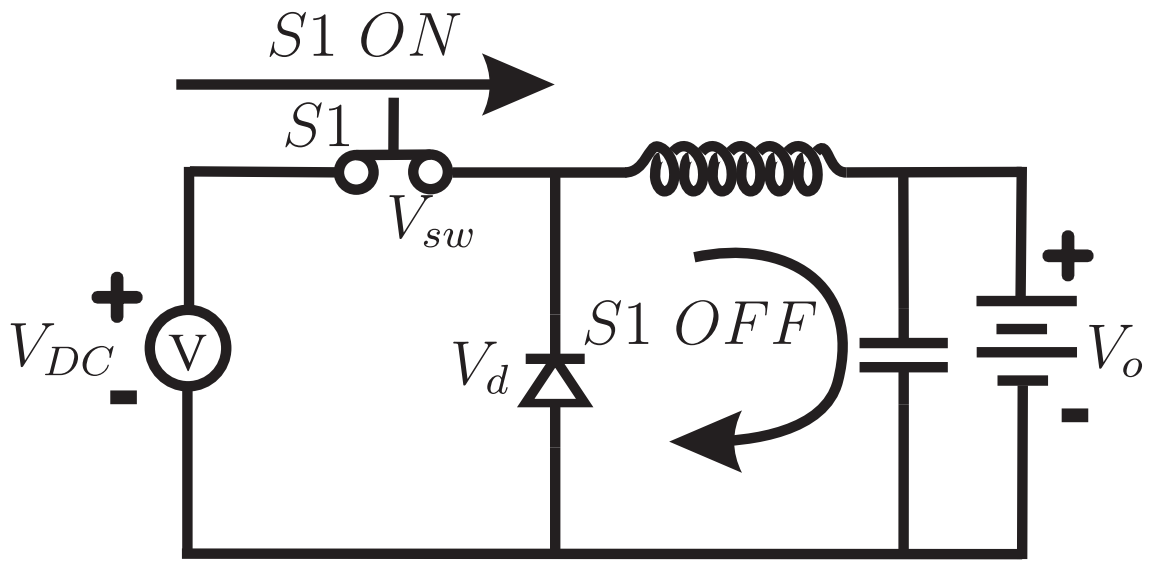

Figure 4.8 Buck Converter

$$V_{ON} = V_{in} - V_{sw} - V_o \approx V_{in} - V_o \tag{4.44a}$$

$$V_{OFF} = V_o + V_D \approx V_o \tag{4.44b}$$

where, V_{ON} and V_{OFF} are voltage drop across the inductor during 'ON' and 'OFF' time. Similarly, V_{in}, V_{sw}, V_o, V_D are input voltage, voltage drop across the switch, output voltage, and voltage drop across the diode.
Hence applying volt-second balance law and simplifying equation 4.44 gives the duty cycle (D) for buck converter as in equation 4.45.

$$D = \frac{V_o}{V_{in}} \tag{4.45}$$

The change in inductor current ($\triangle I$) could be written as in equation 4.46.

$$\triangle I = \frac{V \triangle t}{L_{buck}} \tag{4.46}$$

From volt-second law, $V_{ON}T_{ON} = V_{OFF}T_{OFF}$. Hence, equation 4.46 could be written as,

$$\triangle I = \frac{V_{ON}T_{ON}}{L_{buck}} = \frac{V_{OFF}T_{OFF}}{L_{buck}} \tag{4.47}$$

Using equation 4.44 and equation 4.47, the value of the inductance in terms of peak inductor

current, switching frequency, duty cycle and output voltage can be determined as in equation 4.48.

$$L_{buck} = \frac{V_o(1-D)}{F_s \triangle I} \tag{4.48}$$

where, F_s is switching frequency of the buck converter. Equation 4.48 is used to calculate the inductor size for buck converter.

4.3 SIMULATION PARAMETERS AND RESULTS OF PMSG CONNECTED WITH SMALL WIND TURBINE

In order to observe the overall performance of the system, simulation of the whole system in Matlab/Simulink was performed. Initially, models of PMSG and wind turbine as discussed in Chapter 3 were connected and results were observed. Different input parameters for wind turbines and generators within the modeling are as shown in Table 4.3 and Table 4.4 respectively.

Table 4.3 Wind Turbine Parameters

Rotor Blade Radius (R)	1.25m
Swept Area of the Wind Turbine (A)	6.25m^2
Air Density (ρ)	1.225kg/m^3
Pitch Angle (β)	0^0

Table 4.4 Three Phase PMSG parameters

Stator Resistance (R_s)	2.875 Ω
Inductance on d-axis (L_d)	0.0085H
Inductance on q-axis (L_q)	0.0085H
Permanent Magnet Flux Density (λ_0)	0.175Weber
Pole Pairs (N_{pp})	4
Moment of Inertia (J)	0.0008Kgm^2

4.3.1 Results

The electromagnetic power, rms voltage per phase, electrical frequency and current for different change in wind speeds of 3m/s, 6m/s, 10m/s and 15m/s are as shown in Figure 4.9. Different steady state results for the model of PMSG and wind turbine system is as shown in Table 4.5.

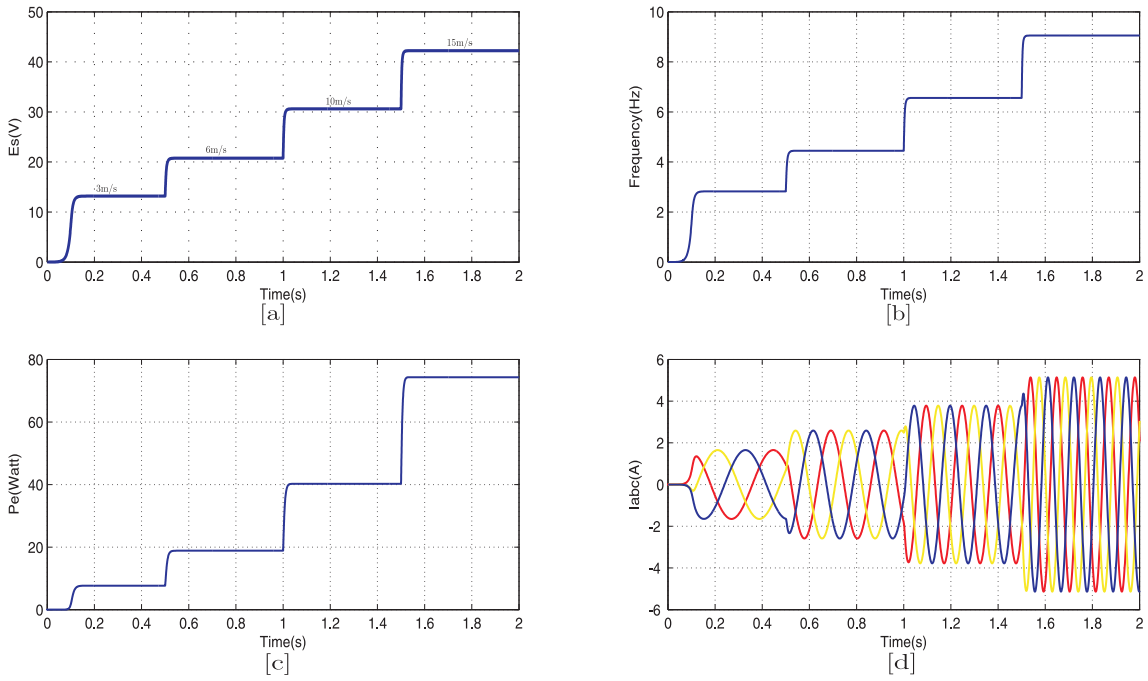

Figure 4.9 RMS Voltage per phase[a], electrical frequency[b], electromagnetic power[c] and three phase current at variable wind speed of 3m/s, 6m/s, 10m/s and 15m/s[d]

Similarly, the change in turbine torque, rotor speed and turbine output power for the change in wind speed is as shown in Figure 4.10. Small transient is observed in output torque and output power during variation in the wind speeds.

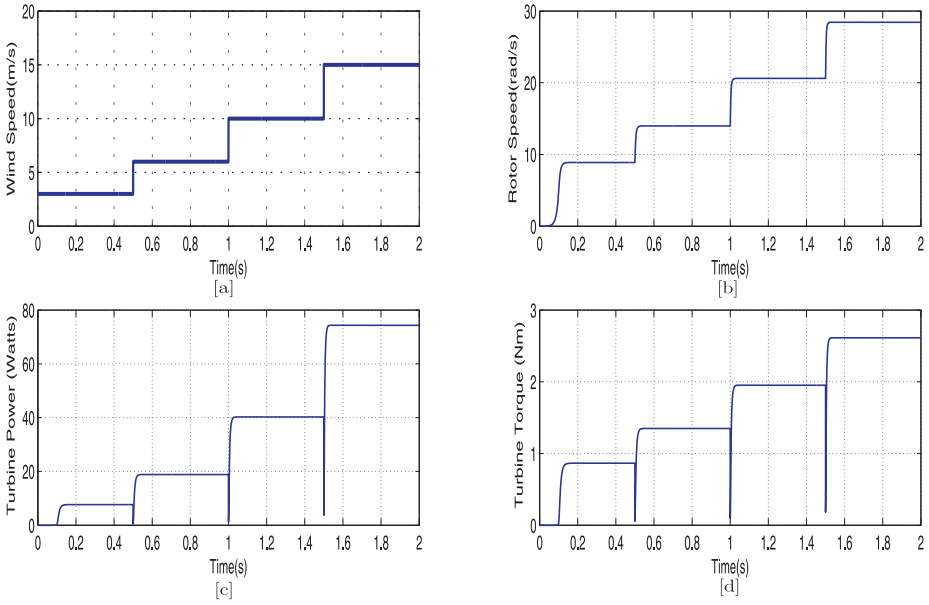

Figure 4.10 Turbine torque [b], turbine output power [c] and rotor speed [d] at different wind velocity of 3m/s, 6m/s, 10m/s and 15m/s [a]

Table 4.5 Summary of the simulation results of Wind Turbine and PMSG for different wind speeds

Wind Speed (m/s)	Three phase peak current(A)	voltage(V_{rms})	Electromagnetic Power (Watt)
3	1.56	13.2	7.67
6	2.53	20.76	18.84
10	3.65	30.61	40.23
15	5.12	42.22	74.3

4.4 THREE PHASE BOOST RECTIFIER SIMULATION RESULTS

A three phase boost rectifier model which uses the principle of DPC-SVM is developed using MATLAB/SIMULINK. Different Parameters used for the modeling are summarized as in Table 4.6.

Table 4.6 Parameters used for the rectifier modeling

Output DC Bus Voltage	80V
Line Inductance	2mH
Line Resistance	0.56 Ω
Load Capacitance	2350μF
Load Resistance	100 Ω
Proportional (P) Gain	4
Integral (I) gain	0.005
Hysteresis band for Active Power (H_P)	0.1
Hysteresis band for Reactive Power (H_Q)	0.1

The DPC SVPWM boost rectifier is simulated using three single phase voltage sources with equal 120^0 phase differences. Initially, the boost rectifier is simulated for constant AC voltage with unity power factor(zero reactive power). This results in a constant boosted DC regulated output voltage as shown in Figure 4.11. In order to test the controller response, the reference reactive power is varied during the simulation period. It can be observed as in Figure 4.12 that the controller quickly responses to the reference reactive power making current in phase, leading and lagging the generator voltage respectively.

Figure 4.11 and Figure 4.12 shows initial startup transients in the generator current. Initially, the capacitor is fully discharged and there is a large voltage difference between input and output and the load tries to draw a huge amount of current. As the voltage stabilizes to a reference value, the current reduces in magnitude and is finally in phase with voltage maintaining UPF. In order to observe the controller response and reduce the initial transient in the current waveform, the load capacitor can be charged to a reference value. Pre-charging the capacitor close to the reference value or even lower than the reference value reduces the current transients by huge

amount as shown in Figure 4.13 where the load capacitor is pre-charged to 80 V.

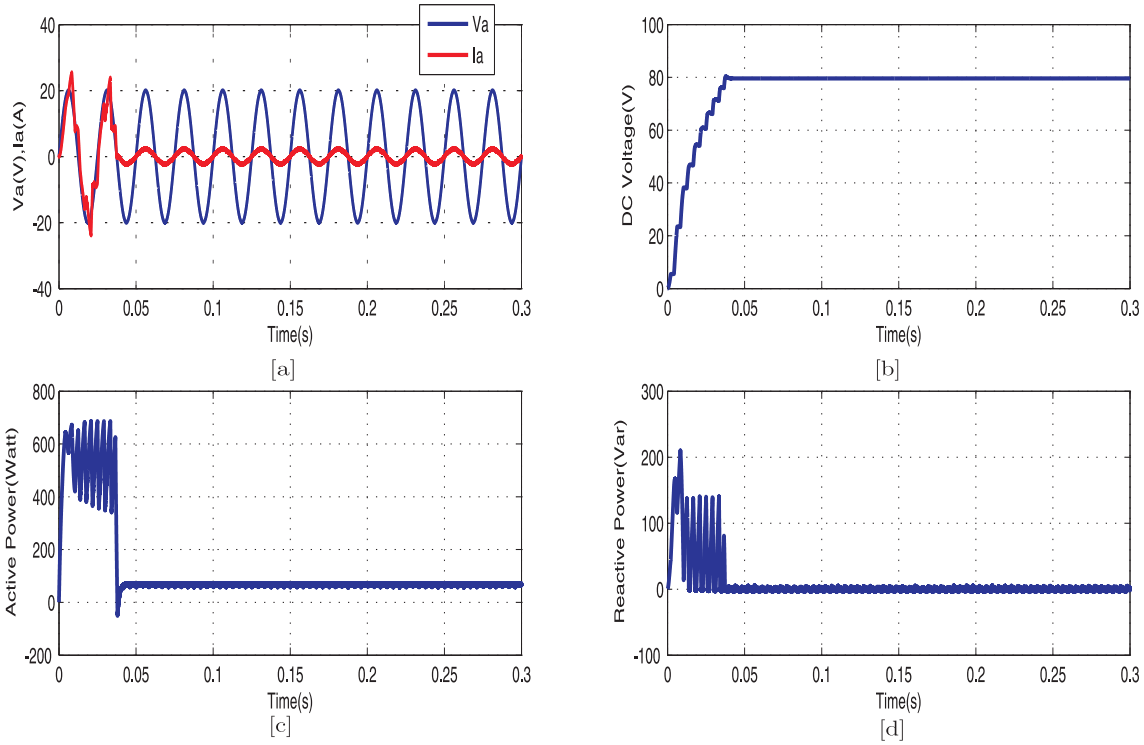

Figure 4.11 Unity Power Factor [a] [d] and regulated DC voltage [b] for a constant input three phase AC voltage [a]

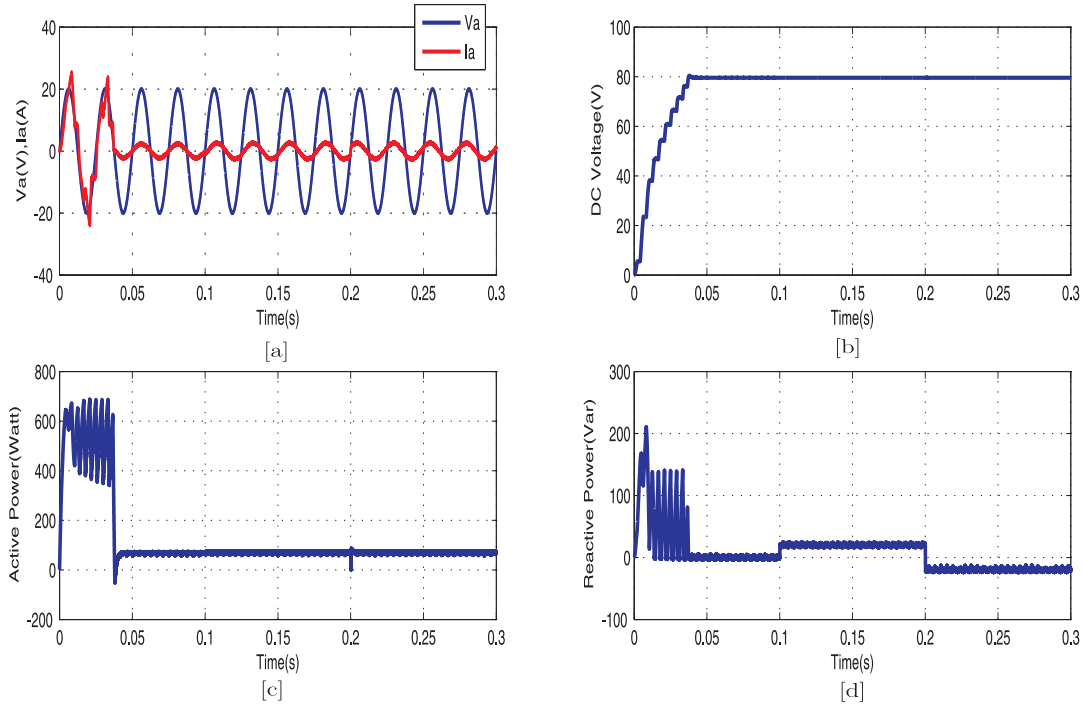

Figure 4.12 Phase A voltage and current for unity, lagging and leading power factor [a] [d] with a regulated constant DC output voltage [b] and constant active power [c]

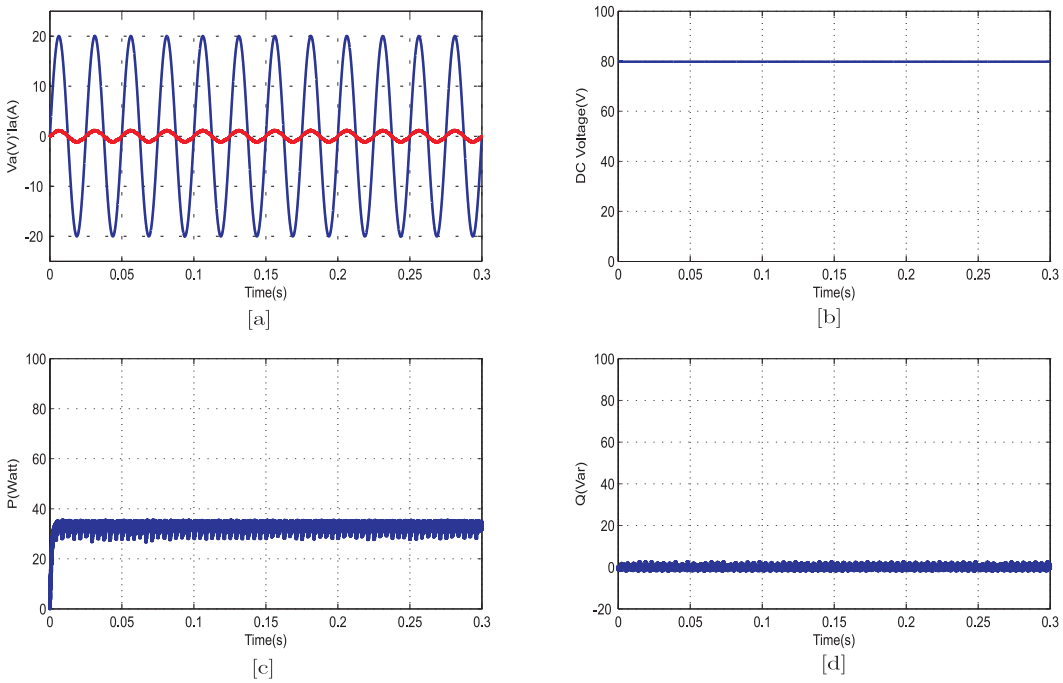

Figure 4.13 Phase A voltage and current [a], DC output voltage[b], active power [c] and reactive power [d] after pre-charging the capacitor to the reference voltage level

In order to model for variable speed wind turbine, the controller was tuned for phase voltages of 15V-50Hz, 20V-60Hz, 25V-70Hz, 30V-80Hz and 40V-100Hz. Figure 4.14 shows that UPF is still achieved with constant boosted DC voltage and constant active power. The start up transient in current causes the spikes in active and reactive power. This can be reduced if the output capacitor is pre charged as discussed for Figure 4.13.

The controller is also simulated for different DC reference voltages. Simulation result in Figure 4.15 shows that with the change in reference DC voltage there is a change in active power while the reactive power is always kept at zero. Hence active power demand could be changed by changing the output DC voltage reference. Similarly, the controller was tested for variable output load (120Ω and 50 Ω) and the output responses are plotted as in Figure 4.16. It can be seen that the variation of load changes the output power maintaining UPF and regulating constant output DC voltage. Hence if the load (current) on the output of the boost rectifier is changed, active power from the turbine could be varied while still achieving UPF. Hence two ways to change the active power is either by changing the reference DC voltage (Figure 4.15) or changing the DC output load (Figure 4.16) . There is a large transients observed in the active and reactive power during the change in reference DC voltage as shown in Figure 4.15. Therefore changing the reference DC voltage to change the active power might not be an appropriate option. From Figure 4.16, It can be seen that the variation of load changes the output power with less transients maintaining UPF and regulating constant output DC voltage.

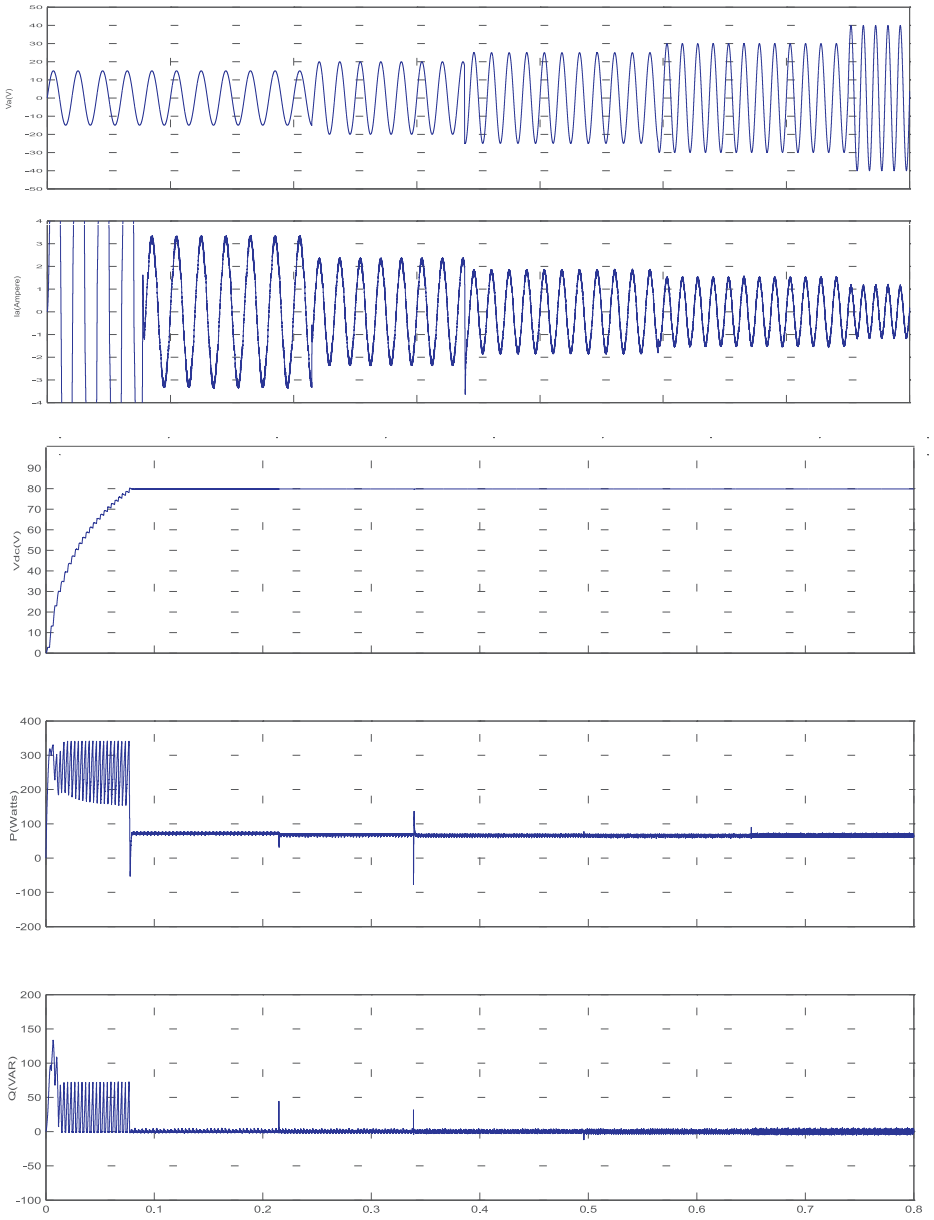

Figure 4.14 DC regulated voltage with UPF for different input voltages and frequencies

Hence, out of these two options, changing the output load in order to change the active power is a desirable option.

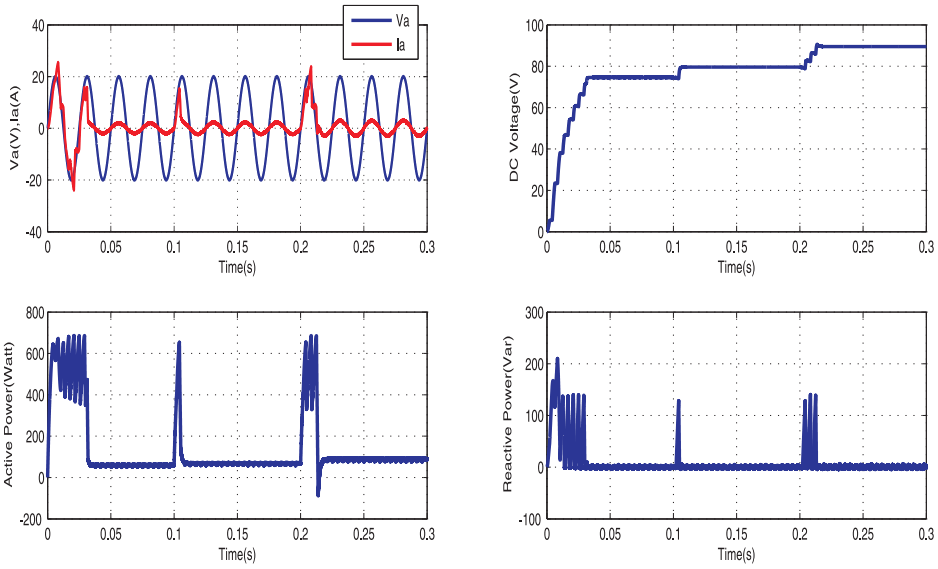

Figure 4.15 DC regulated voltage with UPF for different reference DC voltages

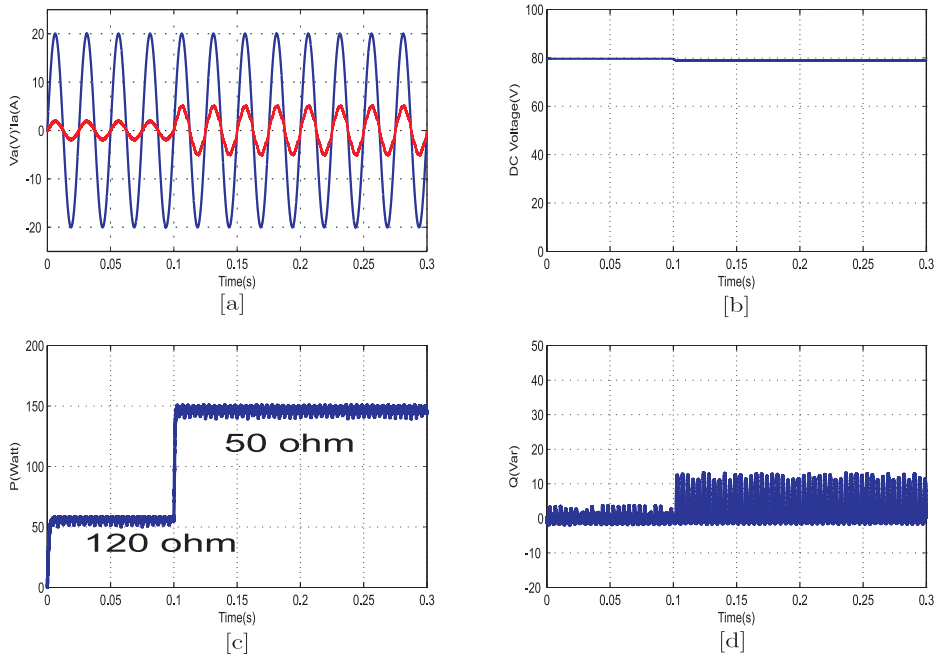

Figure 4.16 Variation of Power for the step change in load [a] Phase voltage and current [b] DC regulated voltage [c] Active Power and [d] Reactive Power

4.5 BUCK CONVERTER SIMULATION RESULTS

A 48 V lead acid battery block model available in simulink is connected across the buck converter. Different parameters of the battery are as shown in Table 4.7. The power flow towards the battery

bank at various duty ratio which is shown in Figure 4.17[b]. A ramp signal as shown in Figure 4.17[a] is used for varying the duty ratio. Figure 4.17[b] shows that the output power varies with the varying duty ratio of the buck converter. A 5Ω current limiting resistor is used in front of 48V battery bank system. All the parameters for model development of the wind turbine, PMSG and boost rectifier are taken from Table 4.3, Table 4.4 and Table 4.6 respectively. For a buck converter, an inductance and output capacitance values of 1.26mH and 2350 μF are taken respectively.

Table 4.7 Different parameters of 48V battery model

Nominal Voltage	48V
Rated Capacity	50Ah
Initial state of Charge	80%
Maximum Capacity	52.2632Ah
Nominal Discharge Current	10A
Internal Resistance	0.0096Ω
Capacity @ Nominal Voltage	15.5139Ah
Exponential Zone [Voltage Capacity]	[48.8684V 0.166667Ah]

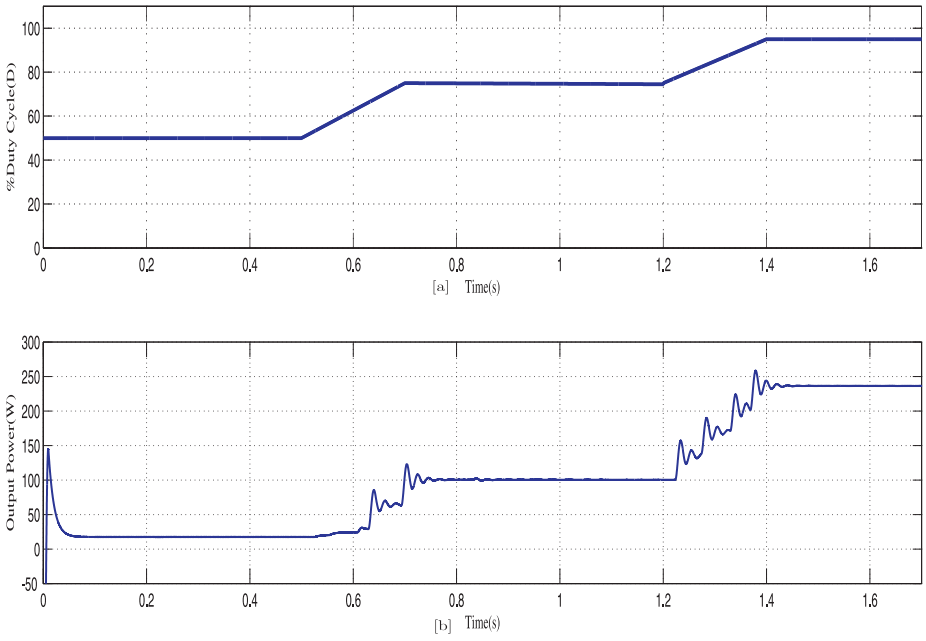

Figure 4.17 [a] Variable duty cycle (50%, 75% to 95%), [b]Power flowing towards the battery bank at these duty ratios

Similarly, the battery voltage for variable duty ratio is as shown in Figure 4.18[a] and the battery charging current is as shown in Figure 4.18[b]. It can be seen from Figure 4.18 that the battery voltage remains almost constant but the charging current increases with the increase

in converter's duty ratio. Hence the variation of duty ratio of the buck converter changes the power fed to the battery.

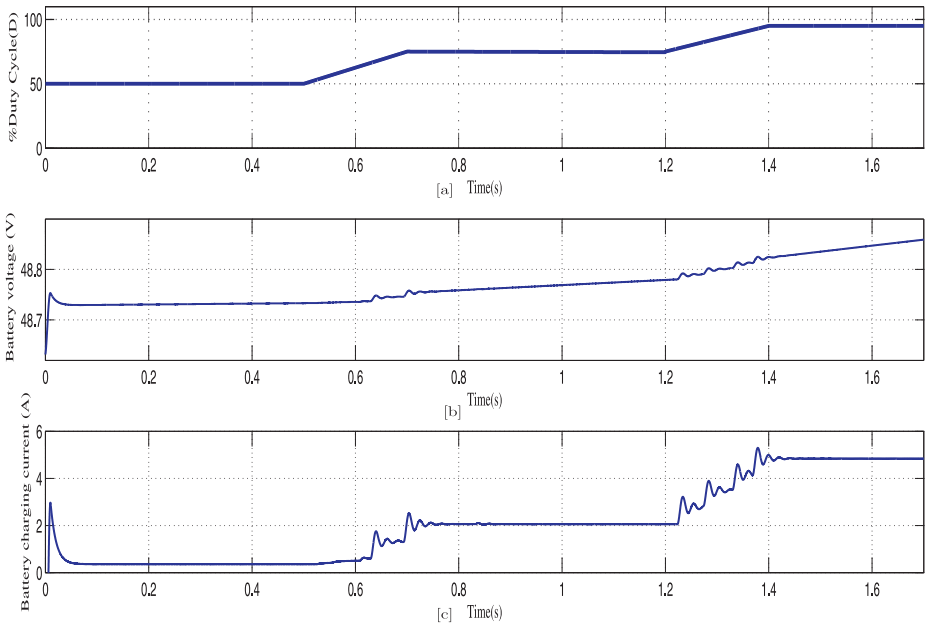

Figure 4.18 [a]Variable duty cycle (50%, 75% and 95%), [b] battery voltage and [c]battery charging current at these duty ratios

4.6 SIMULATION RESULTS OF THE ENTIRE SYSTEM

The entire System consisting of Wind Turbine, PMSG, three phase boost rectifier and buck converter were connected together. Figure 4.19 shows output voltage and current for one of the phases. It shows that UPF is obtained at variable wind speed. The phase current decreases at higher wind speed so that the reference active power within the boost rectifier is achieved. Figure 4.19[d] shows that constant boosted DC voltage 0f 80V is achieved at variable wind speeds.

The output power from the PMSG at three different wind speeds (5m/s, 10m/s and 15m/s) without implementing MPPT controller is as shown in Figure 4.20. Figure 4.20 shows that with the increase in wind speed (which is a ramp function rather than a step change), there is substantial increase in the output power from PMSG with less transient at the variation of wind speed. The next stage is to test the output power from PMSG with the implementation of MPPT controller. A MPPT algorithm as explained in Section 4.2 is implemented to control the duty cycle of the buck converter. Figure 4.21 shows that the controller continuously look for the peak power out of the turbine. After it reaches the peak power point at particular wind

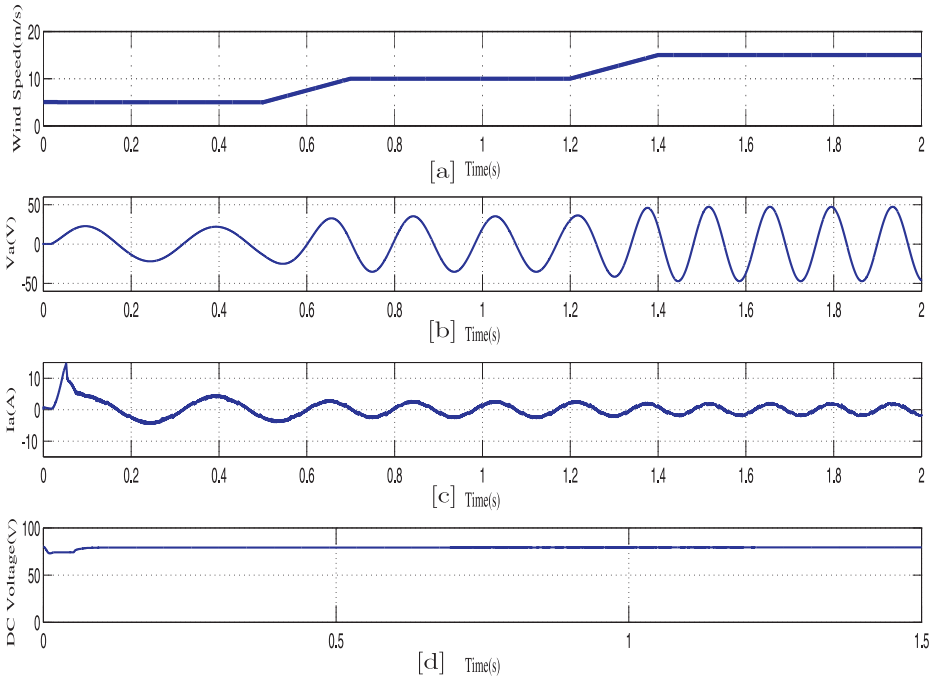

Figure 4.19 [a]Variable wind speeds, [b]Phase A voltage and [c]current achieving UPF, [d]Boosted DC output voltage

speed, the controller tries to settle down to this point. Change in duty ratio ($\triangle D$) is determined according to the location of the operating point. If the operating point is near MPP, $\triangle D$ is less than when the operating point is far from MPP. This ensures that there is less oscillation at MPP.

Output power after implementing MPPT controller is as shown in Figure 4.21. Figure 4.21[b] shows that the output power is increased compared to Figure 4.20[b].

Figure 4.22 shows that the UPF as well as boosted DC voltage is achieved during MPPT operation at different wind speeds.

4.7 CONCLUSION

Controller theory, modeling and simulation part is explained in detail. UPF and stable boosted DC voltage can be obtained by controlling six non-zero and two zero voltage vectors within PWM rectifier. Wind turbine connected with PMSG along with the boost rectifier and DC-DC buck converter is simulated. Algorithm employed for MPPT is explained along with the buck converter theory. Finally, whole system is simulated and results are presented. MPPT is achieved for changing wind speeds of 5 m/s, 10 m/s and 15 m/s with PFC and boosted DC

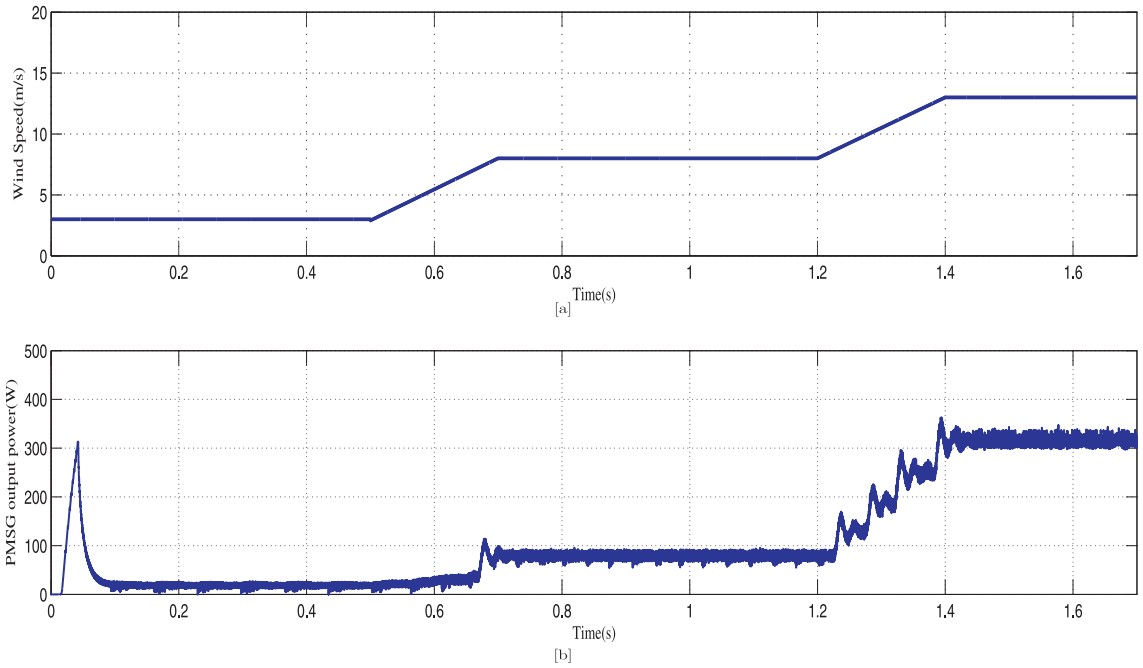

Figure 4.20 [a]Variable wind speeds, [b]PMSG Powers without implementing MPPT controller

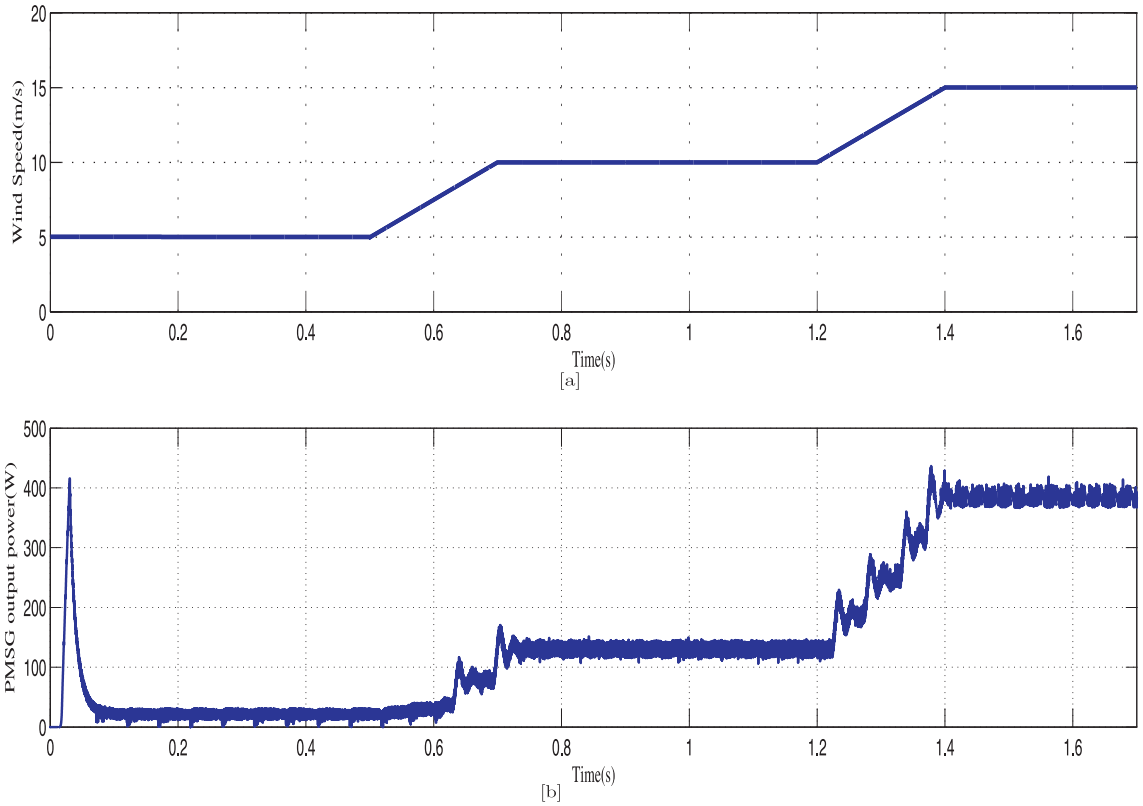

Figure 4.21 [a]Variable wind speeds, [b]PMSG Powers after implementing MPPT controller

output voltage of 80 V.

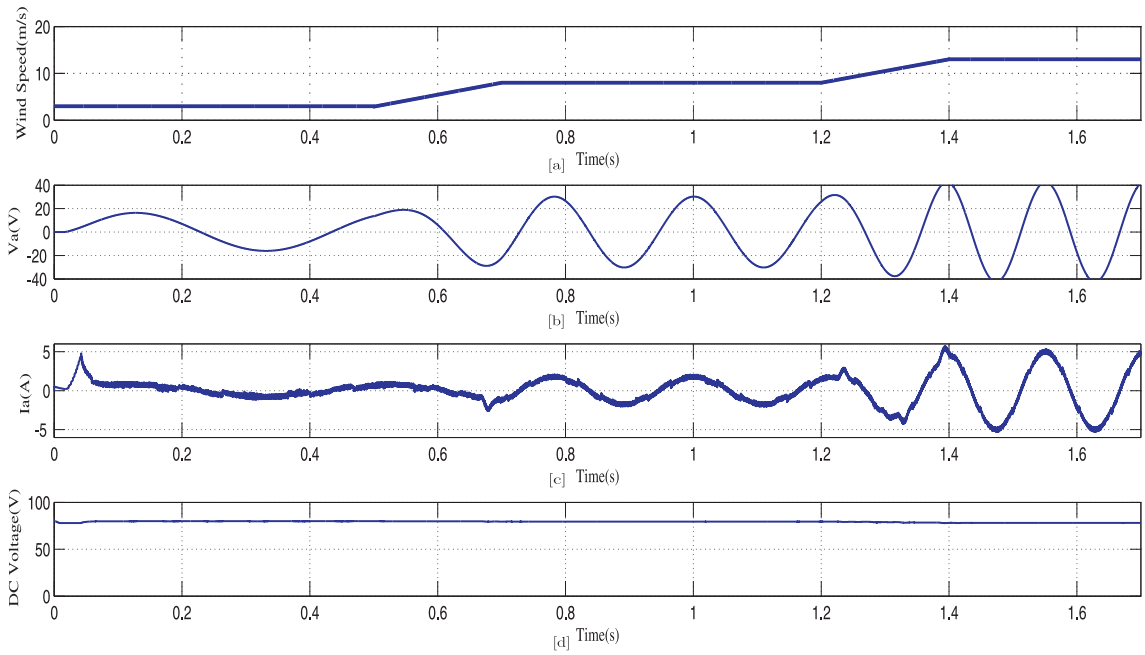

Figure 4.22 [a]Variable wind speeds, [b]Phase A voltage [c] Phase A current and [d] Output boosted DC voltage

Chapter 5

CONTROLLER HARDWARE DEVELOPMENT, TESTS AND RESULTS

5.1 THREE PHASE PWM BOOST RECTIFIER WITH BUCK CONVERTER OUTPUT

Different circuits designed and built to realize a PWM based boost rectifier along with buck converter are explained in the following sections. In order to calculate instantaneous real and reactive power, phase voltages and currents need to be measured. The measured voltages can be used to determine the sectors in which the voltage vector lies. All the calculations of the measured values were done within the micro controller. The instantaneous errors between real and reactive power are converted into a digitized signal (d_P and d_Q) as explained in section 4.1. Using these digitized signals and according to the sector in which the voltage vector lies, three PWM signals for the two switches of the rectifier are generated. A Dead Time Control (DTC) IC is used to generate six signals for each of the switches for the boost rectifier.

5.1.1 Boost Rectifier Design

A boost rectifier is designed such that it can operate for the system ranging from 50W to 1kW. A 48 V battery bank system is used as the system load. The current rating of all these components is determined by the maximum turbine size (i.e. 1kW). The inductor size is determined from the minimum size turbine such that it can charge the 48 V battery bank. Individual opto-isolator gate driver for each of the MOSFETs is used in which the driver is supplied by separate DC power supply chip. Driver circuit schematic is as shown in Figure 5.1. According to the datasheet of the selected driver, input forward current (I_F) is 10mA and input forward voltage (V_F) is 1.4 V. Hence the current limiting resistor of 1.5kΩ is selected such that it satisfies these ratings of the driver. A filter capacitor of 0.1μF is used. Six PWM signals generated from DTC IC chip are inputs to the anode pin of the gate driver via 1.5kΩ resistor. Selection procedures for the switches and components used within the driver circuits are explained in the section 5.1.4.

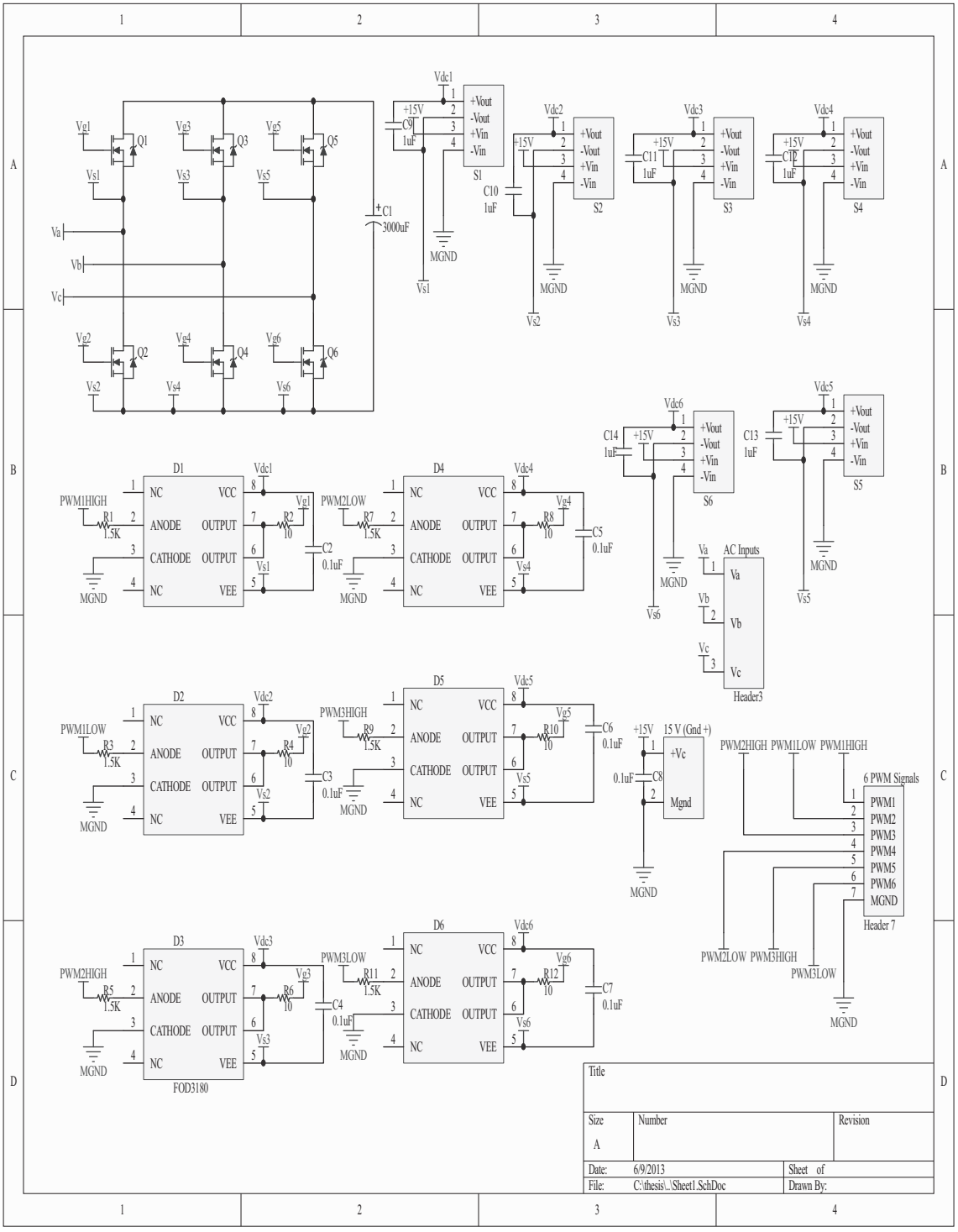

Figure 5.1 MOSFET Driver Circuit

5.1.2 Three Phase Voltage Sensors

Three phase voltage sensors were built using the LM324 op-amp in which the three phase input voltages were first stepped down and then fed into the micro-controller such that the sensed

voltage is within 0-5 V. In the initial stage, an op-amp is used in its inverting configuration in which the AC voltage is stepped down. In a second stage, a summing configuration is used such that the voltage is DC level 0-5 V. A zener diode is used at the output in order to clamp any voltage above 5 V for micro-controller protection. A voltage sensor for one of the phases is as shown in Figure 5.2.

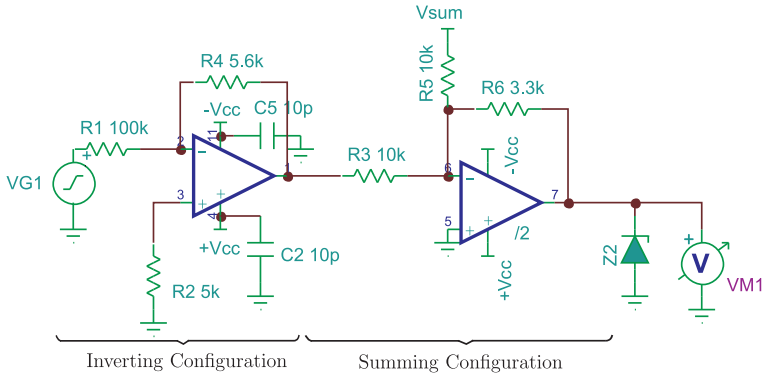

Figure 5.2 Voltage Sensor for a single Phase

The final output voltage from the op-amp is calculated as in equation 5.1 which is a basic summing equation of an op-amp.

$$V_0 = (V_{sum} + V_1)(\frac{-3.3}{10}) \tag{5.1}$$

where, V_{sum} is the summing voltage and V_1 is the output voltage from the inverting amplifier. V_1 is given as in the equation 5.2.

$$V_1 = V_a(\frac{-5.6}{100}) \tag{5.2}$$

where, V_a is the voltage from one of the phases. V_{sum} is kept at -7.5 V such that the output AC voltage is referenced at 2.5 V. A typical sensed AC voltage and its output is as shown in Figure 5.3 in which the input voltage of the sensor is 100V (pk-pk) at 40Hz.

From equation 5.1 and equation 5.2, the final expression that is used to calculate the phase voltage (V_a) out of the system within micro-controller is as given by equation 5.3.

$$V_a = (3.03V_0 + V_{sum}) \times 17.857 \tag{5.3}$$

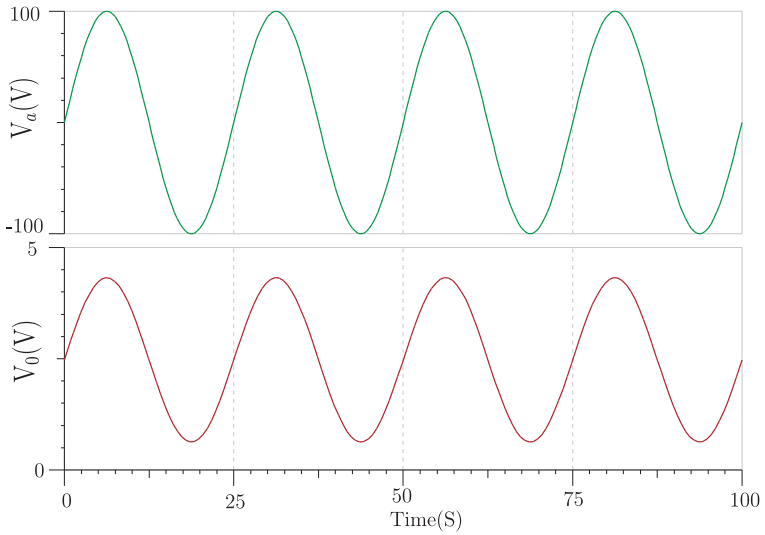

Figure 5.3 Voltage Sensor output(V_0), given a phase voltage(V_a)

5.1.3 Three Phase Current Sensors

The LEM current transducer HXS 10-NP/SP3 was used for sensing the phase currents out of the generator whose output is referenced at 2.5 V. From the datasheet of the HXS 10-NP/SP3 LEM current transducer, the output voltage from the current sensor is as given by equation 5.4.

$$V_{out} = V_{OE} \pm (0.625 \times \frac{I_p}{I_{PN}}) \tag{5.4}$$

where, V_{OE} is the electrical offset voltage which is given by V_{ref}±0.0125 and V_{ref} is the reference voltage at 2.5±0.025 V. I_P is the maximum primary current (30 A when the primary is connected in series and 60 A when connected in parallel). I_{PN} is a nominal primary current (10 A when primary is connected in series and 20 A when connected in parallel). For a 50 Watt to 1 kW system, a series connection topology is used whose nominal current is 10 A and has a maximum current of 30 A. Considering all of these above conditions and using equation 5.4, an approximated final expression used to calculate the actual value of phase current (I_a) is as given in equation 5.5.

$$I_a = 16 \times (V_{out} - 2.5) \tag{5.5}$$

Two of the phase currents are sensed and the current on the third phase is calculated assuming a balanced system such that $I_a + I_b + I_c = 0$ where I_a, I_b and I_c are the phase currents in each of the phases.
The circuit connection of the LEM transducer for current sensing with series primary connection (such that pin 2 and pin 7 are connected) is as shown in Figure 5.4.

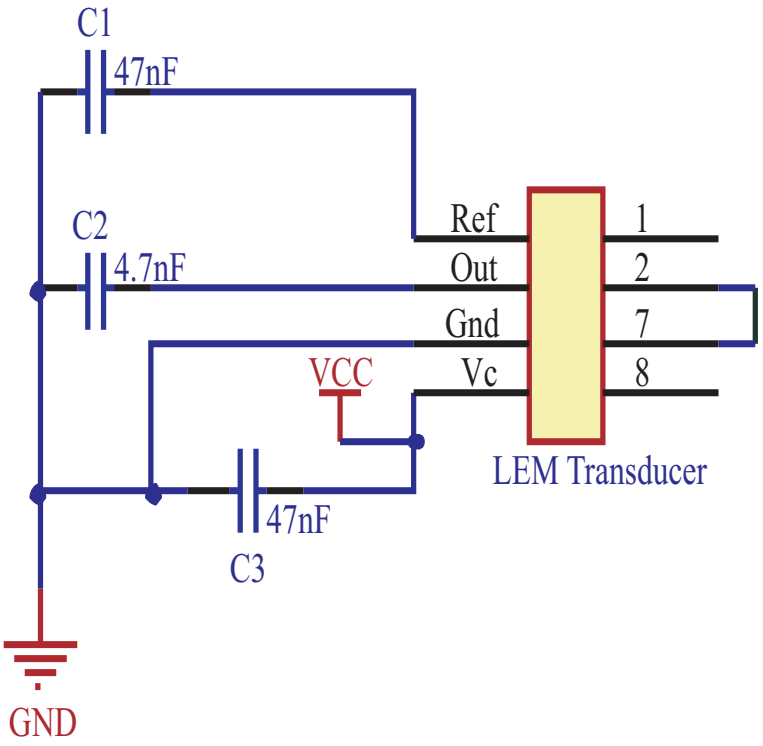

Figure 5.4 LEM Current Transducer Circuit

5.1.4 MOSFET and Driver Selection for the Three Phase Boost Rectifier

MOSFETs are generally preferred for wide line or load variations, long duty cycle, low voltage (<250V) and low power (<500 watts) applications [Blake and Bull]. MOSFETs are generally used for battery charging [Blake and Bull]. An N-channel MOSFET was selected with low $R_{DS(on)}$ within the range of V_{DS} and I_D. The IPP50CN10N MOSFET manufactured by Infineon Technologies was chosen with a $V_{DS} = 100$ V, $R_{DS(on)} = 49$ mΩ and $I_{Dmax} = 20$ A. This a low cost MOSFET with a dollar each.

Matching the MOSFET and MOSFET gate Driver

There are multiple variables involved in selecting the appropriate MOSFET driver for the MOSFET used within the design. Parameters such as input-output propagation delay, quiescent current, latch up immunity and driver current rating must be taken into account while selecting the driver [Technology 2004]. Moreover, power dissipation of the driver also effects the packaging decision and the driver selection. There are three elements of power dissipation in the MOSFET driver [Technology 2004].

1. Power dissipation due to charging and discharging of the gate capacitance of MOSFET (P_c) as given by equation 5.6.

$$P_C = C_G \times V_{DD}^2 \times F_{sw} \tag{5.6}$$

where, C_G is the MOSFET gate capacitance, V_{DD} is the supply voltage of the MOSFET driver and F_{sw} is the Switching frequency.
2. Power dissipation due to quiescent current drawn by the MOSFET driver (P_Q) as shown in equation 5.7.

$$P_Q = (I_{QH} \times D + I_{QL} \times (1 - D)) \times V_{DD} \tag{5.7}$$

where, I_{QH} is quiescent current of the driver with the input in the high state and I_{QL} is quiescent current of the driver with the input in the low state, D is the duty cycle of the rectifier.

3. Power dissipation due to cross-conduction (shoot-through) current in the MOSFET driver (P_s) as given in equation 5.8.

$$P_S = CC \times F_{sw} \times V_{DD} \tag{5.8}$$

where, CC = Crossover constant (A.S)

From equation 5.6 through to equation 5.8, it can be concluded that only one of the three elements(i.e. P_C) is due to the charging and discharging of the MOSFET gate capacitance. This portion of power dissipation is the highest especially at the higher switching frequencies.
In order to calculate the value of equation 5.6, the gate capacitance is required which is comprised of two capacitances: the gate-to-source capacitance and gate-to-drain capacitance (Miller capacitance). The proper method for determining gate capacitance is to look at the total gate charge (Q_G) in the MOSFET datasheet. Rather than using input capacitance (C_{ISS}) rating of the MOSFET, total gate capacitance needs to be calculated from the total gate charge of the MOSFET [Technology 2004].
For the selected MOSFET (IPP50CN10N G), the total gate charge is determined from the graph of gate-to-source voltage (V) versus total gate charge (nC) provided by its datasheet. From the datasheet, at V_{GS} = 10 V and V_{DS} = 50 V,the gate charge is around 12.2nC. The total gate capacitance then equals 1.22 nF.
Six MOSFET gate drivers are used for six MOSFETs and each driver is supplied through a separate isolated DC power supply. This design is used in order to acoid bootstraping issues (which can be a problem for high duty ratios). Different components used for the driver design are summarized in Table 5.1.

Table 5.1 Components rating for the driver circuit

MOSFET Driver	FOD3180-opto-coupler, 2A, Gate drive O/P
Isolated 15V DC-DC supply	MEE1S1515DC
Current limiting resistance	1.5 KΩ
Output Resistance from the Driver	10 Ω
Capacitors	0.1μF

5.1.5 DC Voltage Sensor for the Boost Rectifier Output

Output DC voltage is sensed through an op-amp such that input for the micro-controller is within 0-5 V. The circuit schematic for the DC voltage sensor is as shown in Figure 5.5. The output DC voltage is stepped down by 56 times using the voltage divider as shown in Figure 5.5.

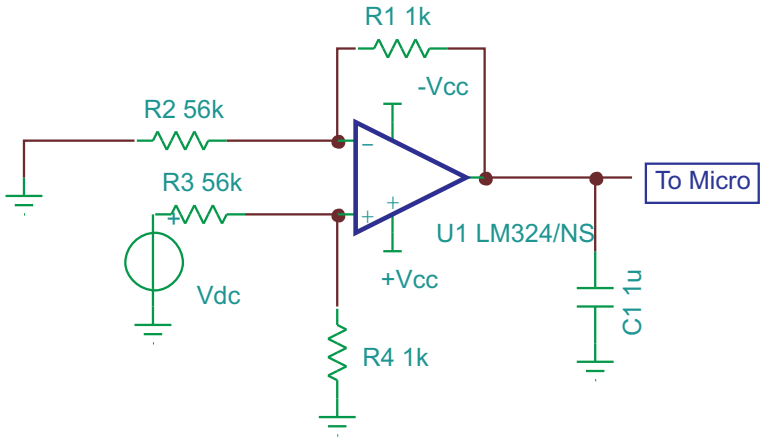

Figure 5.5 DC voltage Sensor for Boost Rectifier

5.2 BUCK DC-DC CONVERTER DESIGN AND COMPONENTS SELECTION

Different parameters used for selecting the components for the DC-DC buck converter is as shown in Table 5.2 Considering a nominal 48 V DC bus system (i.e. 48 V battery bank system), a 55 V output from the buck converter is considered. A constant voltage of 80 V is assumed to be the input for the buck converter. The controller was designed to operate in the range of 50W to 1 kW system. Hence there is a wide variation in the peak current values which determines the required inductance. A specific ripple current is initially chosen for the design. The load current is equal to the inductor current in case of the buck converter assuming that the average capacitor current is zero for steady state condition.

Table 5.2 Design Parameters for DC-DC buck Converter

Input Voltage (V_{in})	80 V
Output Voltage (V_{out})	55 V
On Voltage (V_{on})= V_{in}- V_{out}	25 V
Current ripple factor (r)	0.4
Minimum Power	50 W
Maximum Power	1000 W
Minimum Load Current	0.9 A
Maximum Load Current	18.1 A
Minimum Peak Current	1.3 A
Maximum Peak Current	18.7A
Duty Cycle	0.6875
Switching Frequency(F_{sw})	30 kHz
Inductance (L)	1.26 mH
Peak Flux Density (B_{pk})	0.3 T
Estimated copper loss (P_{cu})	3 W

5.2.1 Components Selection for the Buck Converter Design

The size of an inductor, output capacitor, diode and MOSFET (switch) were chosen according to the rating as shown in Table 5.2. The size of the inductor is obtained from the minimum load current (for 50 W system) and the current rating is obtained from maximum current (for 1000 watt system). Assuming ripple factor of 0.4, minimum load current of 1.3A, duty cycle (D) of 0.675 and switching frequency (F_{sw}) of 30kHz, the size of inductor is calculated as in equation 5.9.

$$Inductance = \frac{V_{on} \times D}{F_{sw} \times r \times Loadcurrent} \tag{5.9}$$

Hence, inductor size of 1.26mH is obtained. With this value of inductance, current ripple (r) is reduced at the higher power values. Hence peak current of 18.7A is obtained for 1000W turbine system. Hence, 1.26 mH, 18.7 A rating of the inductor is required such that it satisfies the design criteria. The full inductor design details are provided in Section 1.3.
In order to calculate the value of output capacitance for a buck converter, peak to peak ripple voltage ($\triangle V_c$) is specified. Equation 5.10 is used to calculate the value of output capacitor [Rashid].

$$\triangle V_c = \frac{\triangle I}{8 F_{sw} C} \tag{5.10}$$

where, $\triangle I$ is the peak to peak ripple current of the inductor, F_{sw} is the switching frequency and

C is output capacitance. Assuming 200mV of peak to peak ripple voltage, switching frequency of 30 kHz and peak current ($\triangle I$) of 7.24 A (i.e. ripple $\times$ load current), output capacitance of 151μ F is obtained. The MOSFET and the diode is rated for the maximum load current (18.7 A).

5.3 INDUCTOR DESIGN PROCEDURES FOR BOOST RECTIFIER AND BUCK DC-DC CONVERTER

Three inductors of the boost rectifier (one for each phase) and one inductor for the dc-dc buck converter were designed and built. The core geometry can be selected if the quantities such as inductance (L) peak flux density (B_{max}), resistivity (ρ), maximum current (I_{max}) and Resistance (R)of the winding are specified as given by equation 5.11 [Rashid].

$$\frac{A_c^2 W_a}{MLT} \geq \frac{\rho L^2 I_{max}}{B_{max}^2 R K_u} \tag{5.11}$$

where, A_c is area of the core, W_a the window area, MLT the Mean Length per Turn and K_u the fraction area filled by copper. The term $\frac{A_c^2 W_a}{MLT}$ is denoted as K_g which is also known as the core geometry. Some of the readily available EE cores with its geometry are as given in Table 5.3.

Table 5.3 Different E cores along with its geometry

Types	Core Area(A_e, mm^2)	Window Area(W_a, mm^2)	Magnetic path(MLT,mm)	$K_g(cm^5)$
EE10	12.1	23.3	26.1	0.013
EE13	17	34.3	30.2	0.032
EE16	19	41.4	34.5	0.043
EE19	23	55.8	39.4	0.07
EE25	40	79	48.7	0.26
EE30	109	75.8	57.7	1.56
EE40	128	164	77.3	3.48
EE50	226	262	95.8	13.97
ETD59/31/32	368	366	139	35.66
EE60	247	407	110	22.57
EE70X91X19	386	1086	204	79.32
EE80X76X20	406	1100	182	99.62
EE90X56X16	419	608	141	75.70
EE71/33/32	683	968	149	30.30

Using the design parameters, the right hand side of the equation 5.11 comes out to be 27.9 cm^5. Hence the core geometry that has K_g greater than or equal to this value is selected from Table

5.3 which is ETD59/31/32. This particular core was also selected according to its availability and cost.

Different design parameters of the inductor using the ETD59/31/32 core are calculated as in the Table 5.4. In order to reduce the skin effect, wire diameter of twice the skin depth is selected. For practice, three inductors of 0.42 mH each were built and connected in series for the buck converter.

Table 5.4 Inductor parameters of buck DC-DC Converter for ETD59/31/32 ferrite core

Area of the Core, A_c	$368mm^2$
Material permeability,μ_e	1500
Magnetic path length, MLT	0.139m
permeability of air, μ_0	1.25664E-06
Peak flux density, B_{pk}	0.4 Tesla
Inductance, L	0.42 Milli henry
Peak Current, I_{pk}	18.7 Ampere
Number of turns, N	53
Total Reluctance,R_T ($\frac{NI_{pk}}{B_{pk}A_e}$)	6778239 Amperes/Weber
Core Reluctance, R_c	200385 Amperes/Weber
Gap Reluctance,R_g (R_T- R_c)	6577853 Amperes/Weber
Air gap, g ($\mu_0 A_e R_g$)	3 mm
Skin Depth,δ	0.38 mm
Wire Diameter,W_d ($2*\delta$)	0.518 mm^2
Current rating of the wire I_{rat}	1.5 Ampere
Number of parallel conductors ,N_{tot}($\frac{I_{pk}}{I_{rat}}$)	12
Total area of the wire, A_w($N_{tot}\pi W_d^2/4$)	344m^2
Winding area, (W_a)	366 mm^2

Similarly, the design parameters of three inductors for boost rectifier are as shown in Table 5.5.

5.4 LABORATORY SETUP AND RESULTS

In order to test the overall system, a laboratory setup was constructed as shown in Figure 5.6. A 4kW induction motor was used to drive a 1kW PMSG. Programming of a STM32F302 microcontroller was done in order to perform all the calculations for generating three PWM signals for the boost rectifier and another PWM signal for the buck converter. Within the micro-controller, all signal scaling factors were considered to calculate the original signals. Active and reactive powers were calculated and all the signals for DPC-SVM were generated using the instantaneous error between the real and reactive power. Only high side switching signals were generated through micro-controller. A dead time control IC, the IRS 21844 was used in-order to prevent the switching overlap between high side and low side switches. In order to test the MPPT property of the

Table 5.5 Inductor design parameters for Boost Rectifier

Output DC Voltage	80 V
Minimum Input Power	50 Watts
Maximum Output Power	1000 watts
current ripple	0.6
Frequency	30000 Hz
Minimum Output DC Current	0.625A
Maximum Output DC Current	12.5A
Minimum RMS Voltage	10 V
Maximum RMS Voltage	40 V
Minimum RMS current	0.42 A
Maximum RMS Current	8.33 A
Peak Current	0.5 A
Maximum Peak Current	11.78 A
Maximum Peak Voltage	56.57 V
Inductance	5.33 mH

controller, an induction motor inherent torque-speed characteristic was used. At different input voltages, an induction motor has different torque-speed curves. Changing the duty cycle (D) of the buck converter will change the power out of the motor which was determined empirically. For each input voltage for the induction motor, the peak torque value was obtained at particular speed, which is the target speed for MPPT. Hence the controller is checked as to whether it hits this target speed and hence achieve MPP.

5.4.1 Boost Rectifier Results

The three phase boost rectifier was built as shown in Figure 5.7. Six MOSFETs were used for the three phase bridge rectifier. Each MOSFET is driven by an opto-isolator gate driver which is supplied from an isolated DC-DC power supply. Three signals for the top switches generated from the micro-controller is fed to Dead Time Control (DTC) IC which generates six signals with dead time of 4 μS.

Figure 5.8 shows 4 gate signals with DTC . A controller console was developed which displays three phase voltages and currents along with output DC voltage (V_{DC}), active power (P), reactive power (Q), voltage Sector, instantaneous active power error (d_p) and reactive power error (d_q). A lockout system is used within the microcontroller such that the controller is only activated after voltage and current sensors senses respective voltages and currents.

Three phase voltages out of the sensor, such that it is within 0-5 V range are as shown in Figure

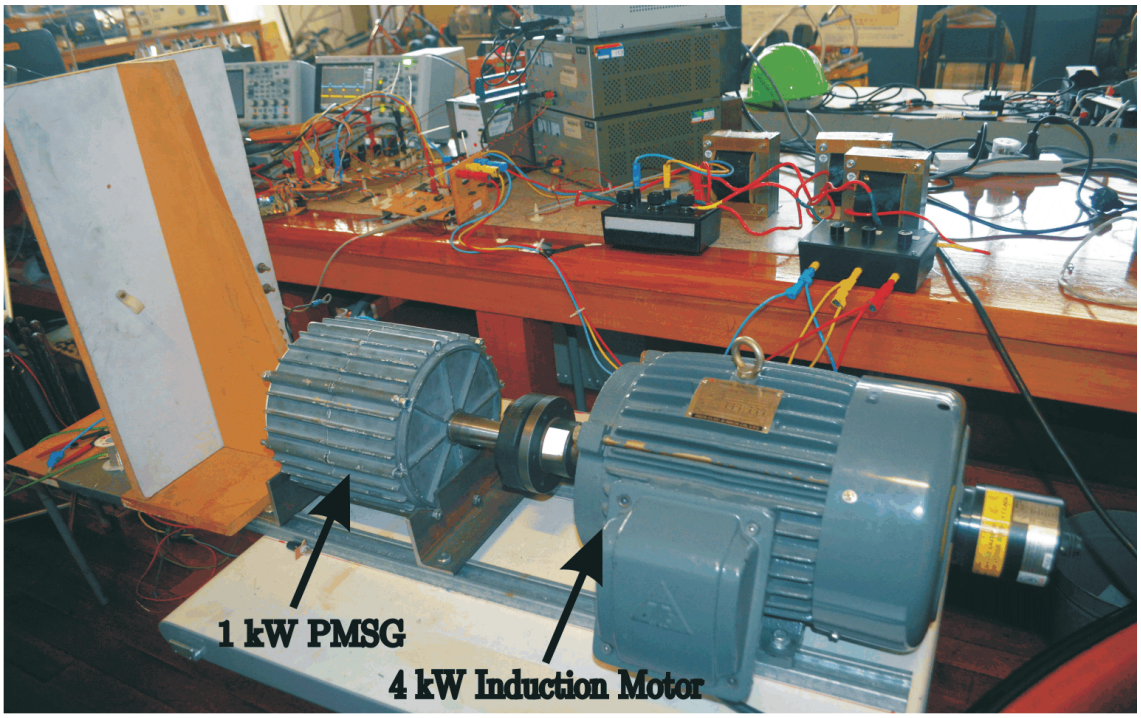

Figure 5.6 Laboratory Setup for Controller Testing

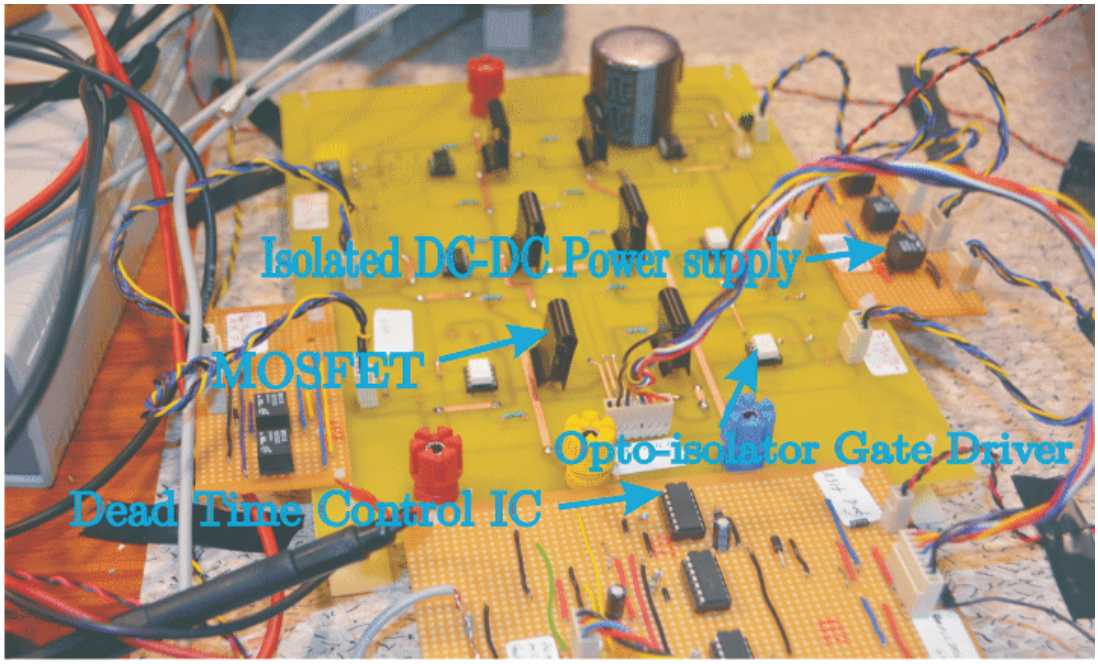

Figure 5.7 Major Components within three phase boost rectifier

5.10.

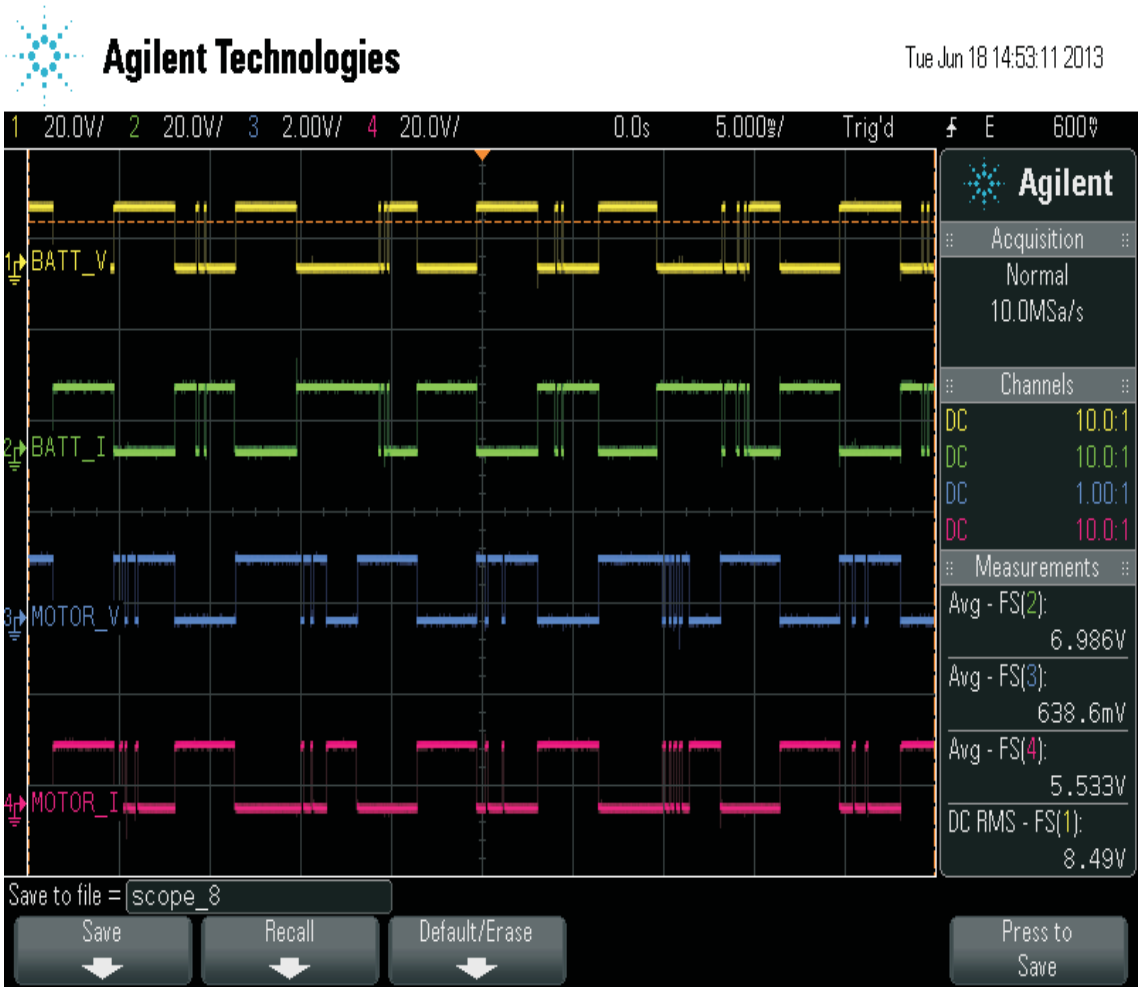

Figure 5.8 Four gate signals from DTC IC

5.4.2 Buck Converter Results

The designed and constructed buck DC-DC converter is shown in Figure 5.11. Initially, the buck converter was tested for different duty ratio. The output power versus duty ratio for a switching frequency of 30 kHz and output load of 55 Ω is shown in Figure 5.12. The converter is supplied through 30V, 5A DC power supply and output voltage and current were measured for constant DC voltage of 30V. PWM signal with switching frequency of 30 kHz is generated through signal generator and the converter is tested at various duty ratio. Figure 5.12 shows that the output power could be varied by varying the duty ratio of the buck converter.

A Gate to Source Voltage (V_{gs}) signal along with load current for the buck converter is shown in Figure 5.13. Negative current in Figure 5.13 is obtained because of the direction of the current probe used to measure the current.

Figure 5.9 A controller console displaying phase voltages and currents along with the DC voltage, active power, reactive power, voltage sector and instantaneous active and reactive power errors

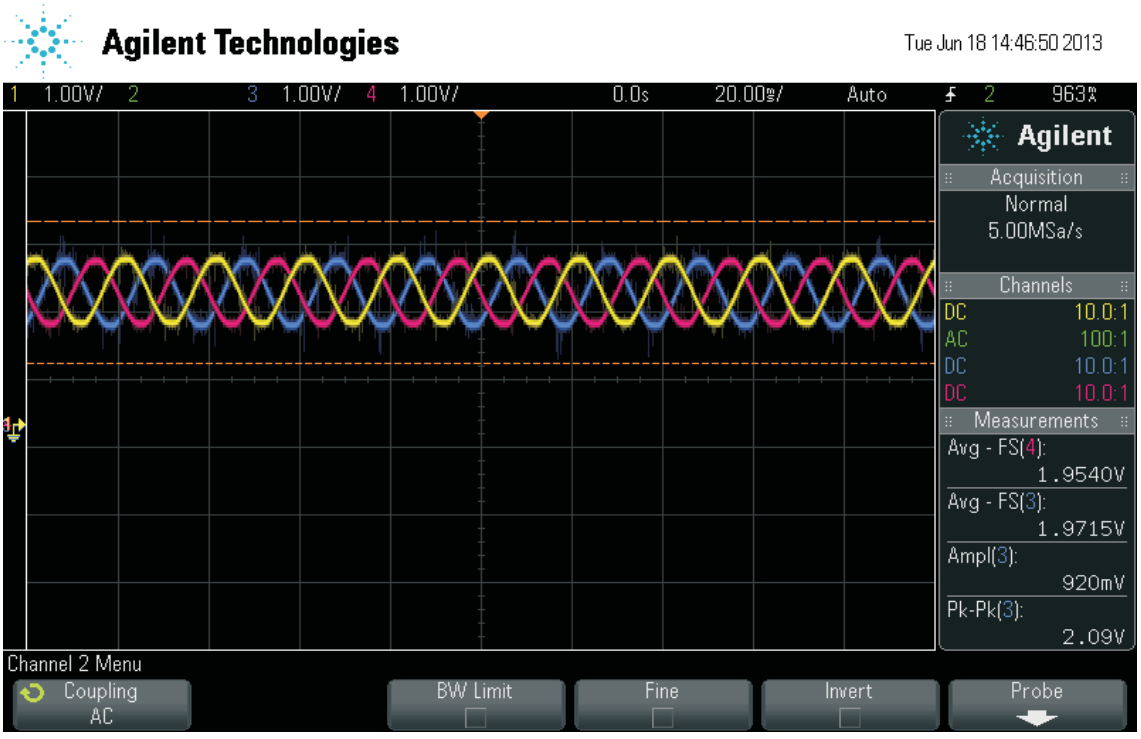

Figure 5.10 Three phase voltages out of the sensor kept within 0-5 V which is fed to the microcontroller

In order to test the proposed MPPT algorithm, an induction motor acting as a wind turbine is characterized for different line-line voltages supplied to the induction motor. For a particular

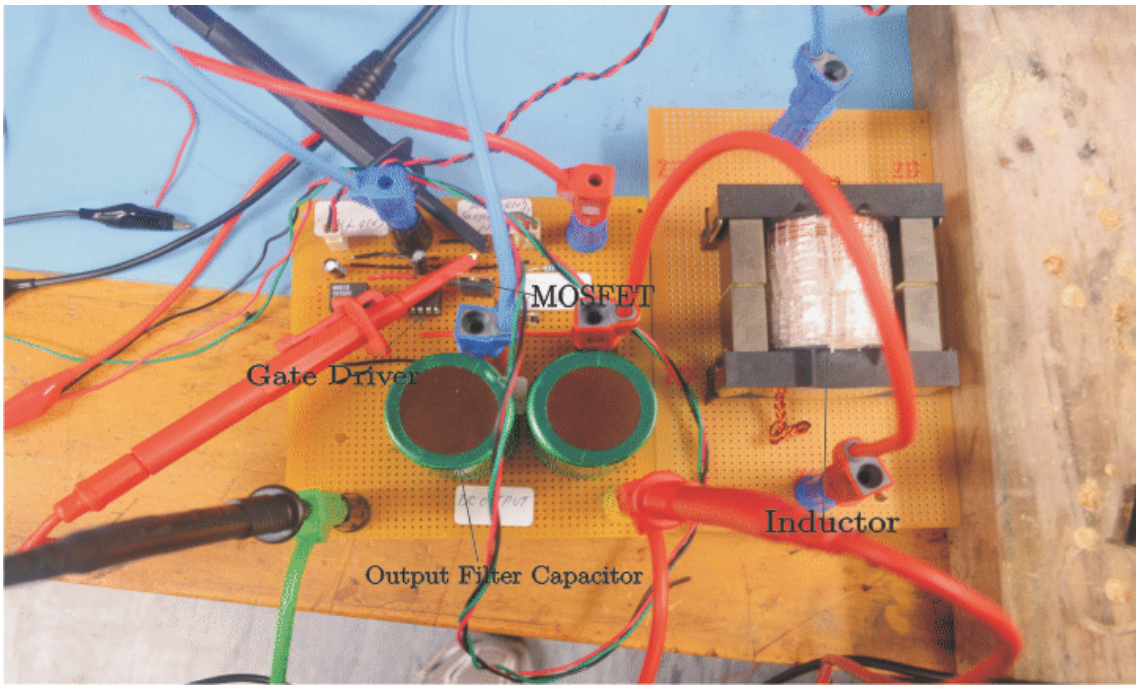

Figure 5.11 Major components in Buck DC-DC Converter

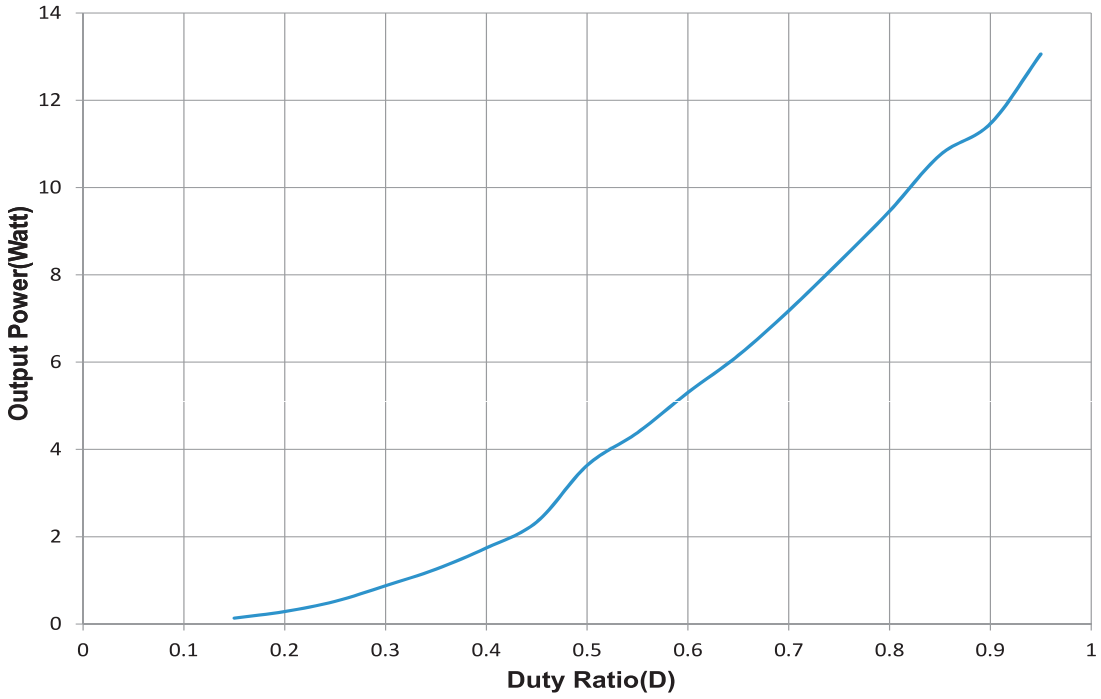

Figure 5.12 Change in output power for various duty ratio of the Buck Converter at switching frequency 30 kHz and output load of 55 Ω

line voltage supplied to the motor, there is a local maxima of the output power. Hence initially the induction motor is characterized in order to determine the local power maxima. The output power versus duty ratio at various induction motor supply voltages are as shown in Figure 5.14.

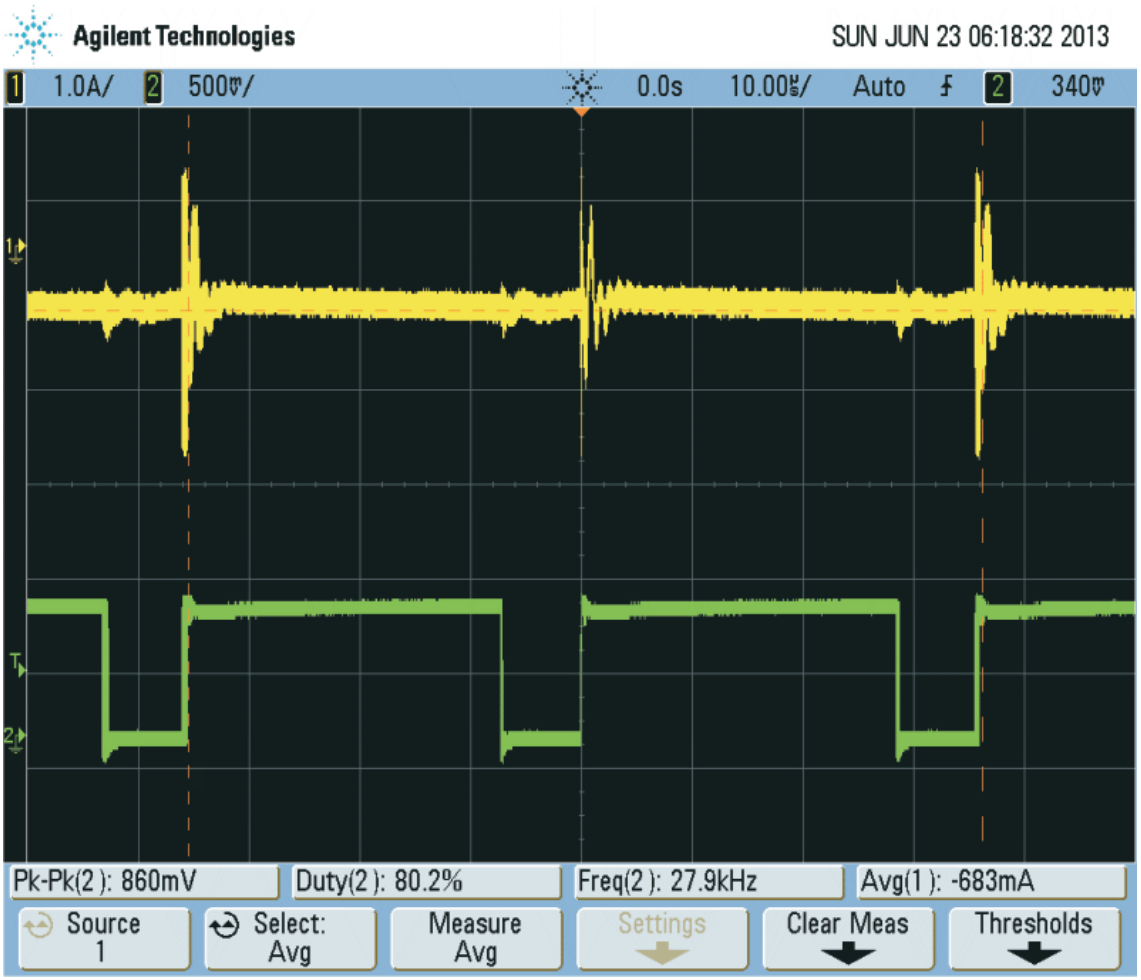

Figure 5.13 Gate signal (green) and output load current (yellow) for buck DC-DC converter in order to characterize the induction motor

The MPPT algorithm was checked for the induction motor power versus duty ratio characteristics and to see if the peak power points were obtained. Initially, sampling time was kept at 2 s. Hence, the duty ratio of the buck converter is changed after every 2 s comparing the power at k and k-1 sampling time. The peak power points reached for different line to line supply voltages are as shown in Figure 5.15. Initially the duty ratio was set at 10% for 30kHz switching frequency as shown in Figure 5.16. The power is sampled for every 2 s and the duty ratio is changed by 2%. Figure 5.14 shows output power at various duty ratio out of the PMSG which is connected to 4 kW induction motor. Speed-torque characteristic of the induction motor is reflected on Figure 5.14 which shows that for a particular three phase supply for the induction motor, there is a duty ratio at which the maximum power out of the PMSG could be extracted. The major objective of the proposed MPPT controller is to operate the system such that it always operates at MPP. Figure 5.15 is compared with Figure 5.14 in order to check the MPPT controller. From Figure 5.15, it can be seen that for different line to line supply voltage for the induction motor, MPP is reached and operates the system at this power unless the supply voltage for an

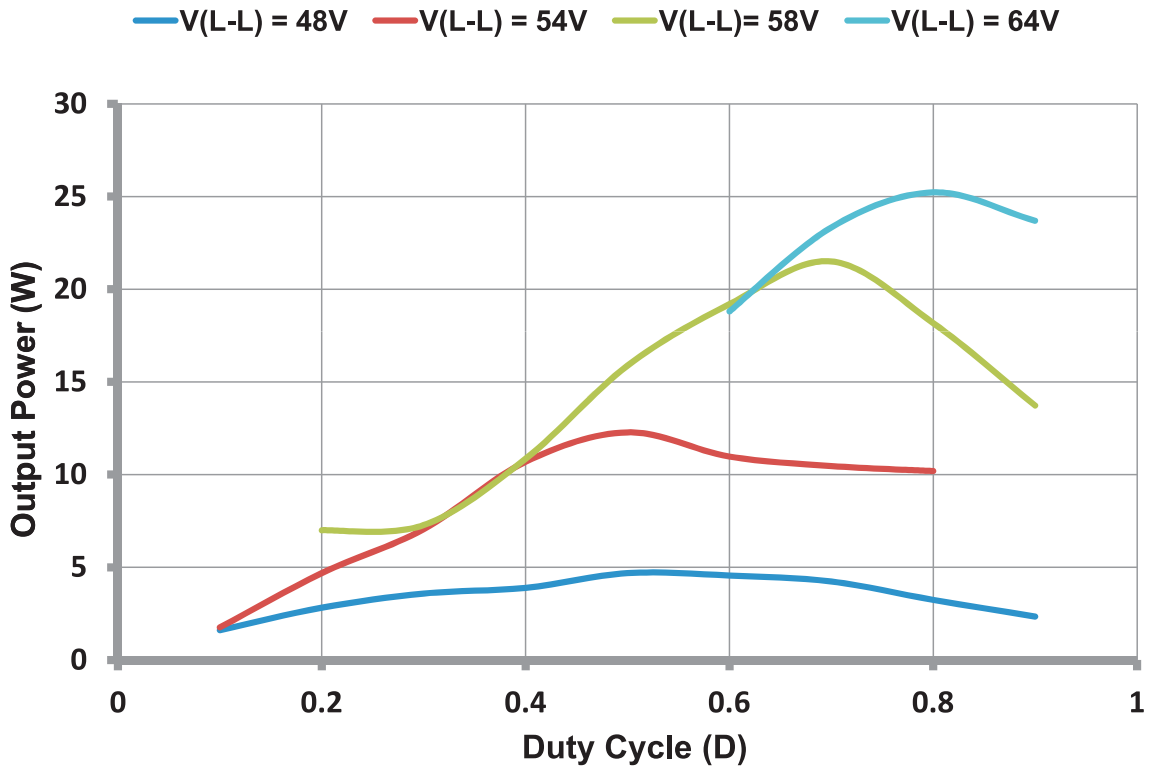

Figure 5.14 Induction motor output power versus duty ratio of the buck converter at various three phase supply voltages

induction motor is changed.

5.5 CONCLUSIONS

Design procedures for the boost rectifier and buck converter are presented. Induction motor is characterized such that it behaves as a wind turbine. MPPT algorithm is implemented and is checked against different supply voltages for the motor. Result shows that duty ratio of the buck converter can be used to change the output power of small wind turbine.

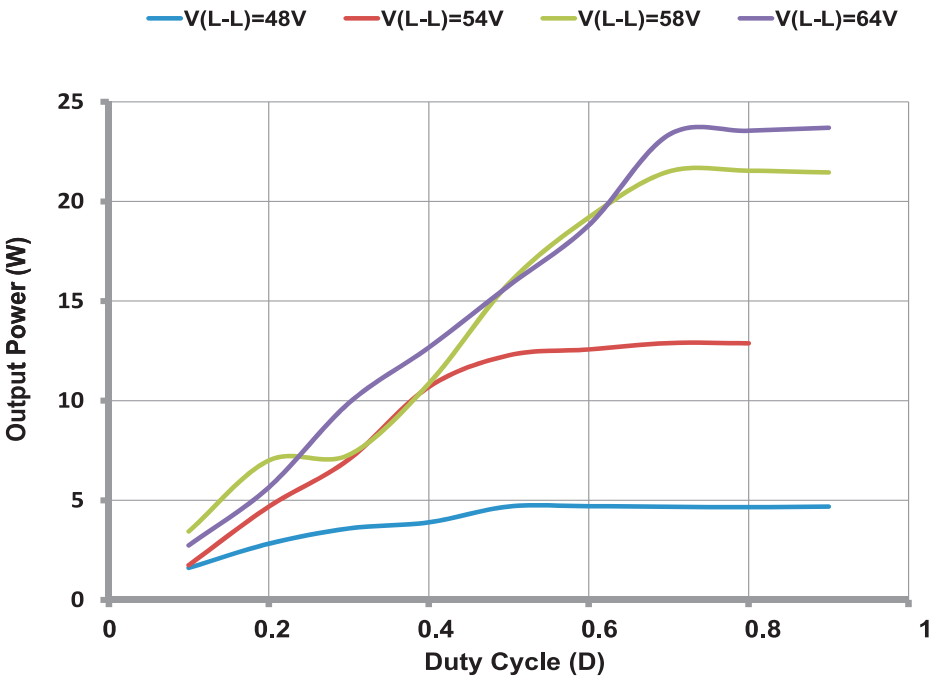

Figure 5.15 Maximum Power reached for different supply voltages of the induction motor after implementing MPPT algorithm

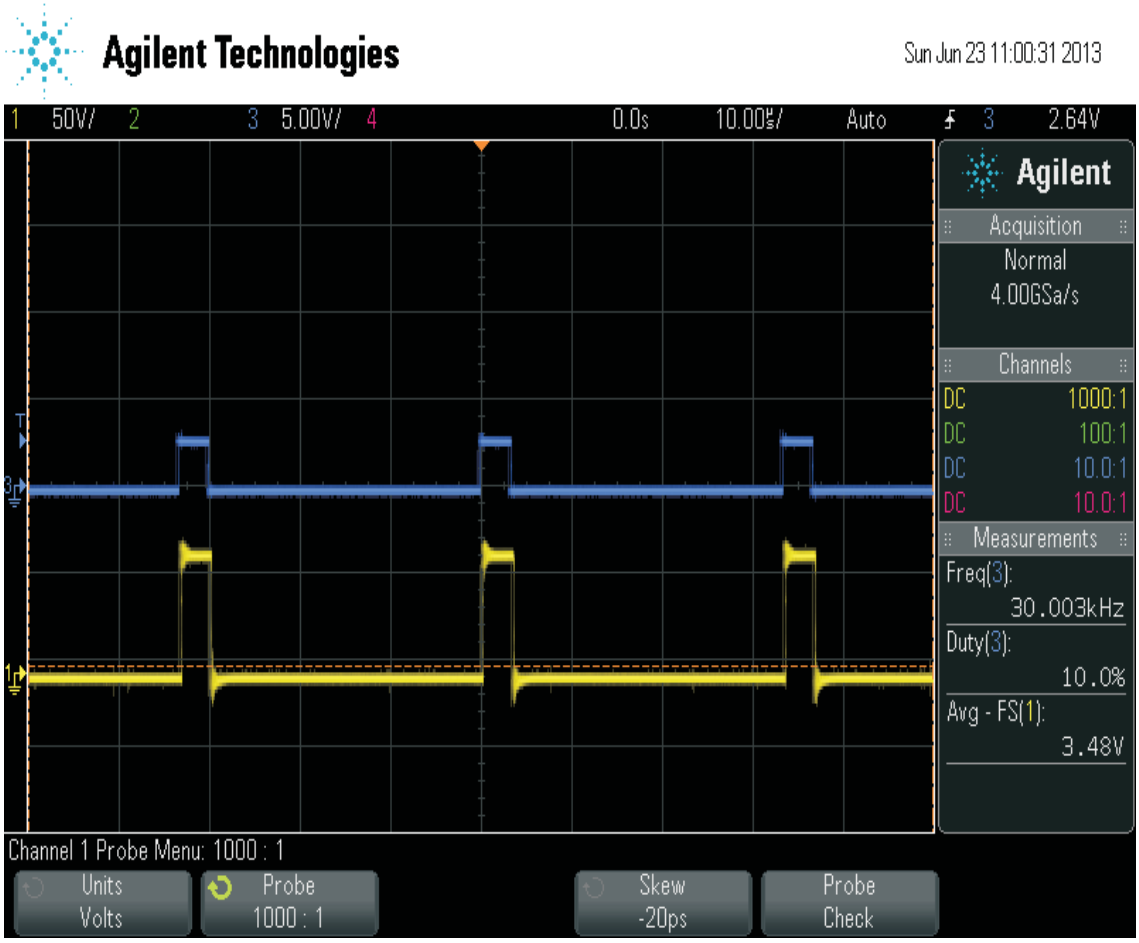

Figure 5.16 PWM signals from microcontroller for MPPT starting from lowest duty ratio (10%) with switching frequency 30kHz (blue) and at the MOSFET gate for buck converter (yellow)

Chapter 6

CONCLUSIONS AND FUTURE WORKS

A system consisting of a three phase rectifier with UPF and boost properties, and a buck converter with MPPT property, was proposed for small scale generating systems. Individual models of wind turbine, PMSG, rectifier and buck converter were developed. Generic aerodynamic equations were used to model small wind turbine. Similarly, a PMSG model was developed in a $d-q$ reference frame. The proposed boost rectifier model is based upon the DPC-SVM strategy. This strategy is chosen as it is based upon the instantaneous active and reactive control loops. Output DC voltage is controlled by controlling the active power and the UPF is achieved by controlling the reactive power. The calculation of instantaneous active power can be used for the MPPT controller at the buck converter side. A buck converter, with MPPT controller that does not require any mechanical sensors was identified. Simulation results for the rectifier showed that UPF can be achieved for variable wind speeds with a constant boosted DC voltage. A 48V battery bank is connected across the buck converter. A battery bank model block developed in Matlab/Simulink was used for observing performance of the overall system. An initial transient in the output voltage and current was observed on the DC side of the boost rectifier. This transient can be reduced by pre-charging the capacitor. For a fixed load, phase voltage out of the generator increases at higher wind speeds while the phase current decreases such that the reference active power is achieved. Simulation result of the boost rectifier based upon DPC-SVM shows that the output active power can be changed by varying either the reference DC voltage or the output load. Varying the reference DC voltage creates a transient in the output DC voltage, active power and reactive power as shown in Figure **??**. While changing the output load shows a smooth variation in the active power and low amplitude transients in the output DC voltage and reactive power. Hence, variation of the load strategy was used to change the active power and achieve UPF along with boosted DC voltage.

The proposed system was designed and built such that it is suitable for 50W to 1kW turbine size. All the components were selected to match this turbine size. Micro-controller programming was done to generate three signals for the top switches of the rectifier based upon DPC-SVM strategy. A dead time control chip was used to generate six signals for the boost rectifier. A

laboratory setup consisting of 4 kW induction motor and 1 kW PMSG (to represent an example WG) to test the controller was developed. The speed-torque characteristics of the induction motor was determined to generate the peak power curves of the motor. The MPPT algorithm was implemented to obtain these peak power points by varying the duty ratio of the buck converter.

Only three phase voltage and current sensors will define the DPC-SVM and MPPT controller parameters. A simple and low cost op-amp as a voltage sensor is implemented. Similarly, LEM transducer is used for current sensing such that accuracy and reliability can be achieved. Beside this, LEM transducer is also easily available. Similarly, low cost MOSFET and opto-coupler driver IC is used within the design.

Beside using three phase voltage and current signals, only two current sensors can be used to estimate the active and reactive powers according to the switching states of the rectifier and the output DC voltage as explained by equation 4.9 and 4.10. A smart charger can be built such that it operates in constant current charging mode when the battery voltage is below its nominal rating and in constant voltage charging mode when the battery voltage is at its rated value. The MPPT controller can be operated according to the battery status. The instantaneous calculation of active and reactive powers require to sense voltage and current signals with minimum noise. Hence, an appropriate low pass filter can be designed and implemented to minimize the signal noises. The buck converter section can also be used for implementing MPPT controller for PV arrays. Since the controller is based upon the instantaneous values of active and reactive power, increasing the sampling time and averaging after every few milliseconds can help to reduce the output transient. The functionality of the controller prototype can be achieved by appropriately tuning the PI controller as well as by suitably choosing the correct switches according to the instantaneous power differences.

REFERENCES

Al-Amoudi, A. and L, Z. (1996), 'Maximum power point regulator for 4 kw solar cell array connected through invertor to the ac grid', In *31st Intersociety Energy Conver. Eng. Conf*, pp. 1669–1672.

Aquamedia Publications, S. (2009), 'International journal of hydropower and dams: World atlas 2009'.

Aulich, H. (1996), 'Small economical pv power generation systems to provide lighting,communication and water supply to rural areas', *The World Renewable Energy Congress*, June, pp. 44–50.

Awards, A. (2009), 'Micro-hydro'.

Bartmann, D. (2008), 'Homebrew wind power'.

Bhide, R. and Bhat, S. (1992), 'Modular power conditioning unit for photovoltaic applications', In *IEEE Power Electronics Conference*, pp. 708–713.

Blake, C. and Bull, C. 'Igbt or mosfet: Choose wisely'.

Blejis, J. and Gow, A. (2001), 'Fast maximum power point control of current fed dc-dc converter for photovoltaic arrays', *Electron Lett.*, Vol. 37, pp. 5–6.

Carvalho, P., Pontes, R., Oliveira, R. and Mesquita, S.B. (2004), 'Control method of a photovoltaic powered reverse osmosis plant without batteries based on maximum power point tracking', *IEEE/PES Transmisson Distribution Conf. Expo*, pp. 137–142.

Chiang, S. and chang, K. (1998), 'Residential photovoltaic energy storage system', *IEEE Trans.Ind.Electron*, Vol. 45, No. 03, pp. 385–394.

Datta, R. and Ranganathan, V. (2003), 'A method of tracking the peak power points for a variable speed wind energy conversion system', In *IEEE Transactions on Energy conversion*, March, pp. 163–168.

Dolara, A., Farand, R. and Leva, S. (2009), 'Energy comparision of seven mppt techniques for pv system', *J. Electromagnetic Analysis and Applications*, Vol. 3, pp. 152–162.

Energy, I. (2009), 'World energy outlook: Executive summary'.

Esram, T. and Chapman, P. (2007), 'Comparison of photovoltaic array maximum power point tracking techniques', *IEEE Transactions on Energy Conversion*, Vol. 22, No. 02, June, pp. 439–449.

Fang, H., Chen, L., Dlakavu, N. and Shen, Z. (2008), 'Basic modeling and simulation tool for analysis of hydraulic transients in hydroelectric power plants', *IEEE Transactions on Energy Conversion*, Vol. 23, pp. 834–841.

Femia, N., Petrone, G., Spagnuolo, G. and Vitelli, M. (2005), 'Optimization of perturb and observe maximum power point tracking method', *IEEE Trans. Power Electron.*, Vol. 20, pp. 963–973.

Go, S.I., Ahn, S., Choi, J., Jung, W., Yun-Yun, S. and song, I.K. (2011), 'Simulation and analysis of existing mppt controol methods in a pv generation system', *International Council on Electrical Engineering*, Vol. 1, pp. 456–451.

Gohnson, G. (2001), *Wind Energy System*, November.

Heier, S. (2006), *Grid integration of wind energy conversion systems*, Wiley.

Hillowala, R. and Sharaf, A. (1992), 'A rule-based fuzzy logic controller for a pwm inverter in photo-voltaic energy conversion scheme', In *IEEE Ind.Appl.Soc. Annual Meeting*, pp. 762–769.

Hiyama, T., Kouzuma, S. and Imakubo, T. (1995), 'Identification of optimal operating point of pv modules using neural network for real time maximum power tracking control', *IEEE Trans. Energy Convers.*, Vol. 10, No. 02, June, pp. 360–367.

Hou, C.L., Wu, J. and Zhang, M. (2004), 'Application of adaptive algorithm of solar cell battery charger', In *IEEE Int. conference*, pp. 810–813.

Hsiao, Y. and Chen, C. (2002), 'Maximum power tracking for photovoltaic power system', pp. 1035–1040.

Hua, C.C. and Lin, J. (2001), 'Fully digital control of distributed photovoltaic power systems', In *IEEE Int. Symp. Ind. Electron*, pp. 311–315.

Hua, C. and Shen, C. (1998), 'Study of maximum power tracking techniques and control of dc-dc converters for photovoltaic power system', pp. 86–93.

Hui, J. and Bakhshai, A. (2008), 'A new adaptive control algorithm for maximum power point tracking in wind energy conversion systems', In *IEEE PESC*, June, pp. 4003–4007.

Hussein, K. and Mota, I. (1995), 'Maximum photovoltaic power tracking: An algorithm for rapidly changing atmospheric conditions', *IEE Proc. Generation Transmission Distribution*, pp. 59–64.

Hussein, A., Hirasawa, K., Hu, J. and Murata, J. (2002), 'The dynamic performance of photovoltaic supplied dc motor fed from dc-dc converter and controlled by neural networks', In *Int. Joint Conference Neural Network*, pp. 607–612.

Iuga, D. 'Small wind turbines'.

Kesraoui, M., Korichi, N. and Belkadi, A. (2011), 'Maximum power point tracker of wind energy conversion system', *Reenewable Energy*, Vol. 36, No. 2, pp. 2655–2662.

Khaeintung, N., Pramotung, K., Tuvirat, B. and Sirisuk, P. (2004), 'Risc-microcontroller built-in fuzzy logic controller of maximum power point tracking for solar-powered light flasher applications', In *30th Annual Conference IEEE Ind. Elect. Society*, pp. 2673–2678.

Kim, T., Ahn, S., Park, S. and Lee, Y.K. (2001), 'A novel maximum power point tracking control for photovoltaic power system under rapidly chnaging solar radiation', *IEEE int.Symp Ind. Electron*, pp. 1011–1014.

Koutoulis, E., Kalaitzakis, K. and Voulgaris, N. (2001), 'Development of a microcontroller-based photovoltaic maximum power point tracking control system', *IEEE Trans. Power Electron*, Vol. 16, No. 1.

Koutroulis, E. and Kalaitzakis, K. (2006), 'Design of a maximum power tracking system for wind-energy-conversion applications', *IEEE Transactions on Industrial Electronics*, Vol. 53, No. 2, pp. 486–494.

Krause, C. (2002), *Analysis of Elecric Machinery*, Wiley, second ed.

Kumari, S. and Babu, C. (2011), 'Comparison of maximum power point tracking algorithms for photovoltaic system', *International Journal of Advances in Engineering & Technology*, November, pp. 133–148.

Kuo, Y.C., T.-J.Liang and Chen, J.F. (2001), 'Novel maximum-power-point-tracking controller for photovoltaic energy conversion system', *IEEE Trans. Ind. Electron*, Vol. 48, No. 3, June, pp. 594–601.

Lo, K. and Chen, Y. (2011), 'Mppt battery charger for stand-alone wind power system', *IEEE Transactions on Power Electronics*, Vol. 26, No. 6, pp. 1631–1638.

Marquez, J., Molina, M. and Pacos, J. (2010), 'Dynamic modeling, simulation and control design of an micro-hydro power plant for distributed generation applications', *International Journal of Hydrogen Energy*, Vol. 35, pp. 5772–5777.

Midya, P., Krein, P., Turnbull, R., Reppa, R. and Kimball, J. (1996), 'Dynamic maximum power point tracker for photovoltaic systems', In *27th Annual IEEE Power Electron Spec. Conf.*, pp. 1710–1716.

Molina, M. and Mercado, P. (2008), 'A new control strategy of variable speed wind turbine generator for three-phase grid connected applications', In *IEEE/PES*, August, pp. 1–8.

Noguchi, T., Togashi, S. and Nakamoto, R. (2002a), 'Short-current pulse based maximum power tracking method for multiple photovoltaic-and-converter module system', *IEEE Trans. Ind. Electron*, Vol. 49, pp. 217–223.

Noguchi, T., Tomiki, H. and Kondo, S. (2002b), 'Direct power control of power converter without power source-voltage sensors', *IEEE TRANSACTIONS ON INDUSTRY APPLICATIONS*, Vol. 34, No. 3, pp. 473–479.

Paish, O. (Ed.) (2002), *Micro-hydropower: status and prospects*, Instn Mech Engrs.

Patcharaprakiti, N. and Premrudeepreechacharn, S. (2002), 'Maximum power point tracking using adaptive fuzzy logic control for grid-connected photovolrtaic system', *IEEE Power Eng. Soc. Winter Meet*, pp. 372–377.

Patsios, C., Chaniotis, A. and Kladas, A. (2008), 'A hybrid maximum power point tracking system for grid connected variable speed wind generators', In *IEEE PESC*, June, pp. 1749–1754.

Rashid, M.H. *Power Electronics Circuits, Devices and Applications*, Prentice Hall of India, third ed., Chap. Five, p. 189.

Ro, K. and Rahman, S. (1998), 'Two-loop controller for maximizing performance of a grid-connected photovoltaic-fuel cell hybrid power plant', In *IEEE Trans.Energy Convers.*, September, pp. 276–281.

Senjyu, T. and Uezato, K. (1994), 'Maximum power point tracker using fuzzy control for photovoltaic arrays', In *Int. conf. Ind. Technology*, pp. 143–147.

Shmilovitz, D. (2005), 'On the control of photovoltaic maximum power point tracker via output parameters', In *Elect.Power Applications*, pp. 239–248.

Silwal, K., Mishra, S., Bhatta, A. and Ghimire, P. (2012), 'Design construction and measurement of small wind turbine system in nepal', *Rentech Symposium Compendium*, Vol. 2, December, pp. 76–80.

Simoes, M., Franceschetti, N. and Friedhofer, M. (1998), 'A fuzzy logic based photovoltaic peak power tracking control', In *IEEE Int.Symp.Ind.Electron*, pp. 300–305.

Sugimoto, H. and Dong, H. (1997), 'A new scheme for maximum photovoltaic power tracking control', In *Power Conversion Conference*, pp. 691–696.

Sun, X., Li, W. and Zhao, Q. (2002), 'A research on photovoltaic energy controlling system with maximum power point tracking', In *Power Conversion Conference*, pp. 822–826.

Tafticht, T., Agbossou, K. and Cheriti, A. (2006), 'Dc bus control of variable speed wind turbine using a buck-boost converter', In *IEEE Power Engineering Society General Meeting*, June.

Technology, M. (2004), 'Matching mosfet drivers to mosfets'.

Thongam, J. and Ouhrouche, M. (2012), 'Mppt control methods in wind energy conversion systems'.

Trzynadlowski, A.M. *Modern Power Electronics*, John Wiley and Sons, second ed., Chap. four, p. 172.

Tsai, H., Tu, C. and Su, Y. (2008), 'Development of generalized photovoltaic model using matlab/simulink', *World Congress on Engineering and Computer Science*, October.

Veerachary, M., Senjyo, T. and Uezato, K. (2003), 'Neural-network-based maximum-power-point-trackingof coupled-inductor inerleaved-boost-converter-supplied pv system using fuzzy controller', *IEEE Trans.Ind.Electron.*, Vol. 50, No. 4, August, pp. 749–758.

Wai, R., Lin, C. and Chang, Y.a. (2007), 'Novel maximum-power extraction algorithm for pmsg wind generation system', In *IET Electric Power Applications*, March, pp. 275–283.

Wang, Q. and Chang, L. (2004), 'An intelligent maximum power extraction algorithm for inverter-based variable speed wind turbine systems', *IEEE Tras. Energy Convers.*, Vol. EC-8, No. 05, pp. 1242–1249.

Wang, S., Qi, Z. and Undeland, T. (2009), 'State space averaging modeling and analysis of disturbance injection method of mppt for small wind turbine generating systems', *APPEEC*.

Wasynczuk, O. (1983), 'Dynamic behavior of a class of photovoltaic power systems', *IEEE Trans. Power App. Syst*, Vol. 102, pp. 3031–3037.

Won, C.y., Kim, D.H., Kim, W.S. and Kim, H.S. (1994), 'A new maximum power point tracker of photovoltaic arrays using fuzzy controller', In *25th Annual IEEE Power Electron. Spec. Conference*, pp. 396–403.

Wu, W., Pongratananukul, W., Qiu, K., Rustom, K. and Kasparis, T. (2003), 'Dsp-based multiple peak power tracking for expandable power system', *Eighteenth Annual IEEE Application Power Electronics Conferece Expo.*, pp. 525–530.

Wu, B., Lang, Y., Zargari, N. and Kouro, S. (2011), *Power Conversion and Control of Wind Energy Systems*, Wiley.

Xiao, W. and Dunford, W. (2004), 'A modified adaptive hill climbing mppt method for photovoltaic power systems', In *35th Annu. IEEE Power Electron. Spec. Conf*, pp. 1957–1963.

Yaoqin, J., Zhongqing, Y. and Binggang, C. (2002), 'A new maximum power point tracking control scheme for wind generation', In *International Conference on Power System Technology*, October, pp. 144–148.

Yu, G.J., Jung, Y.S., Choi, J.Y., Choy, I., Song, J.H. and Kim, G.S. (2002), 'A novel two-mode mppt control algorithm based on comparative study of existing algorithms', pp. 1531–1534.

Zhang, L., Bai, Y. and Al-Amoudi, A. (2002), 'Ga-rbf neural network based maximum power point tracking for grid-connected photovoltaic systems', In *Int. Conf. Power. Electron.,Macchines and Drives*, pp. 18–23.

Appendix A

THREE PHASE BOOST RECTIFIER MODEL BLOCKS

This appendix section provides different blocks used for the Boost rectifier model development in Matlab/Simulink. Figure A.1 provides the instantaneous calculation of the active and reactive powers as given by equation 4.7 and equation 4.8. Similarly, a hysteresis control loop for the active power is as shown in Figure A.2. A lookup table for generating the PWM signals for the boost rectifier is as shown in Figure A.3. Simulink blocks for generating the gate signals are as shown in Figure A.4.

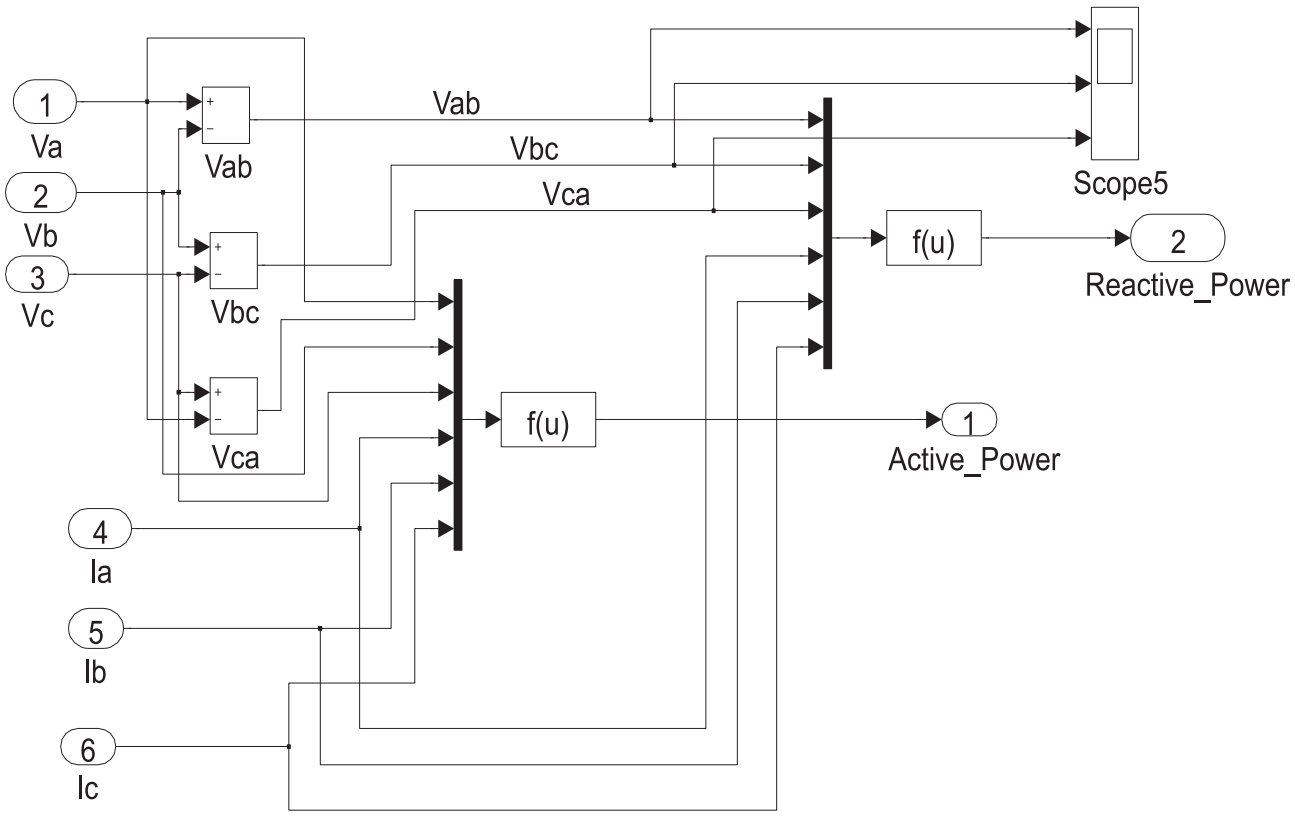

Figure A.1 Instantaneous active and reactive power calculation

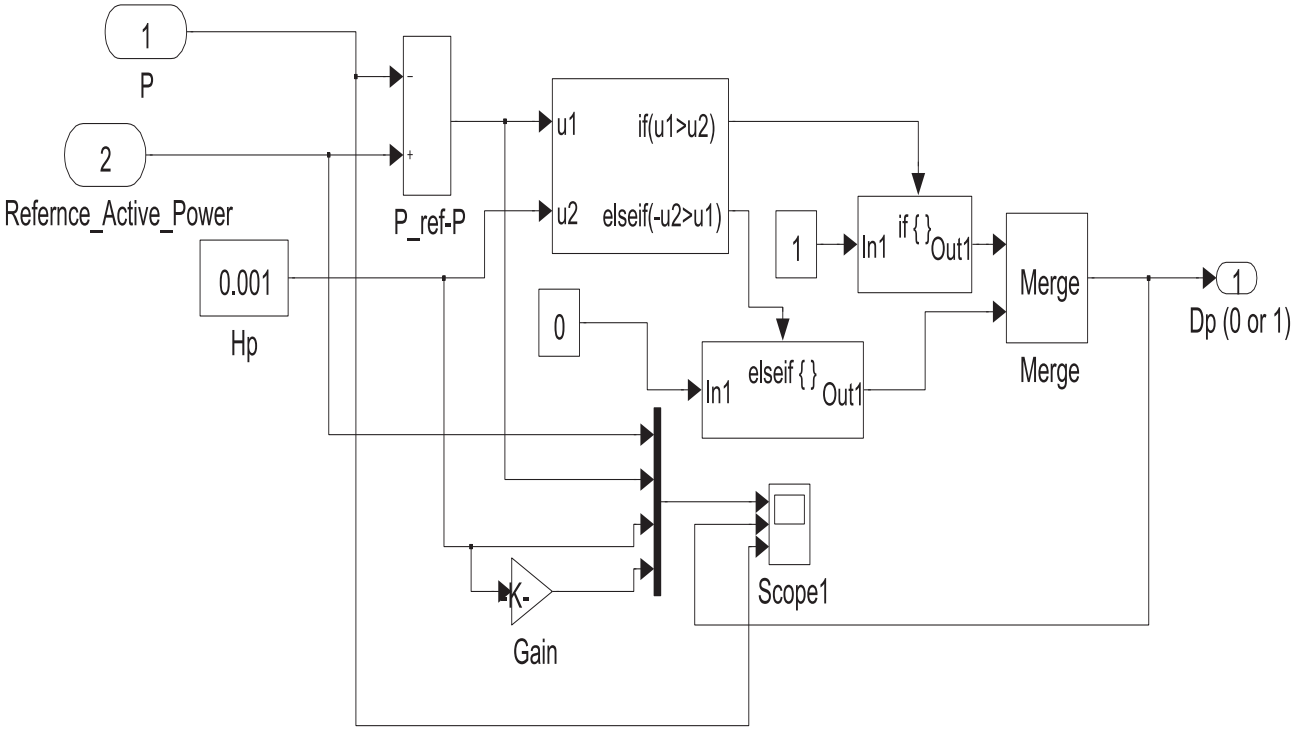

Figure A.2 Hysteresis control loop for active power

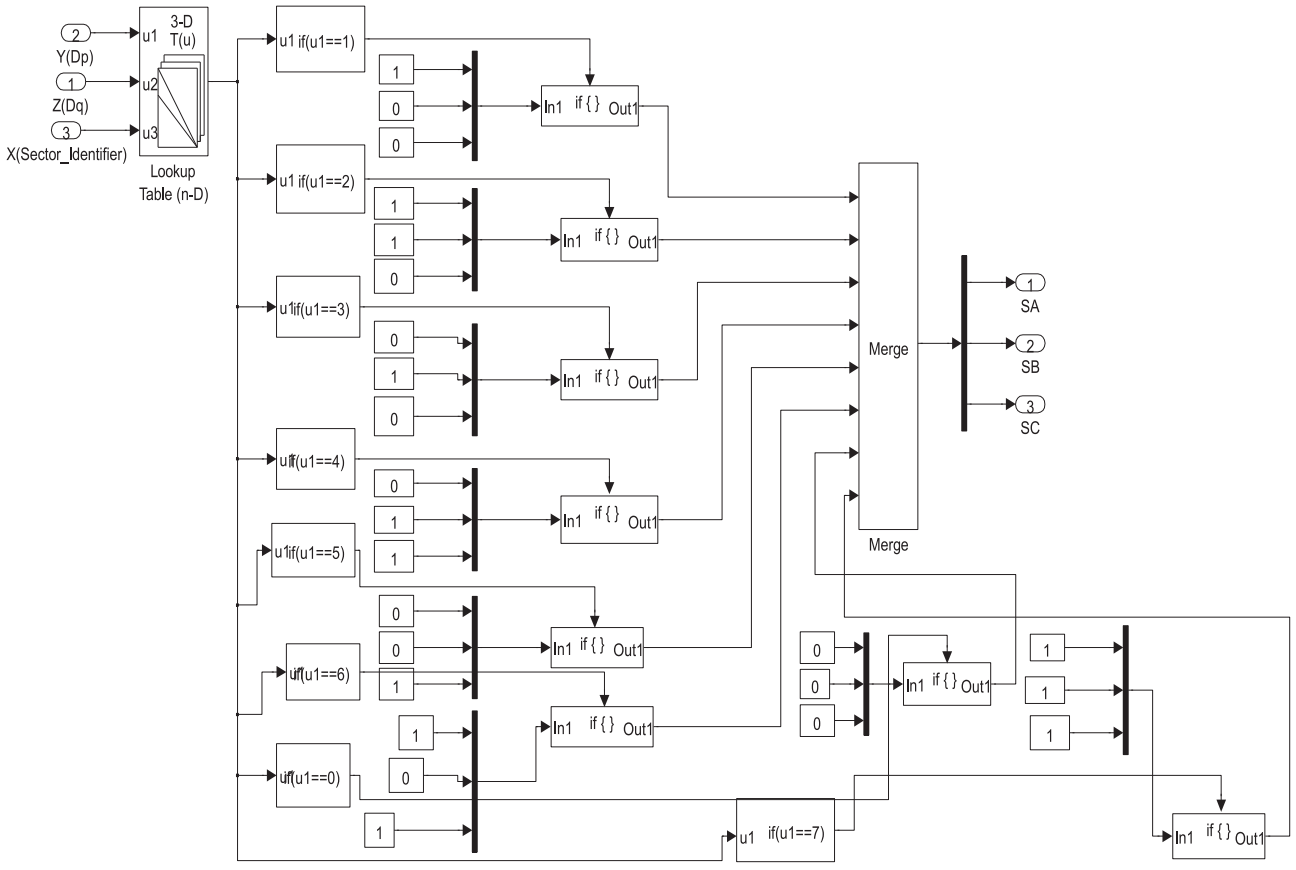

Figure A.3 Lookup table for generating gate signals

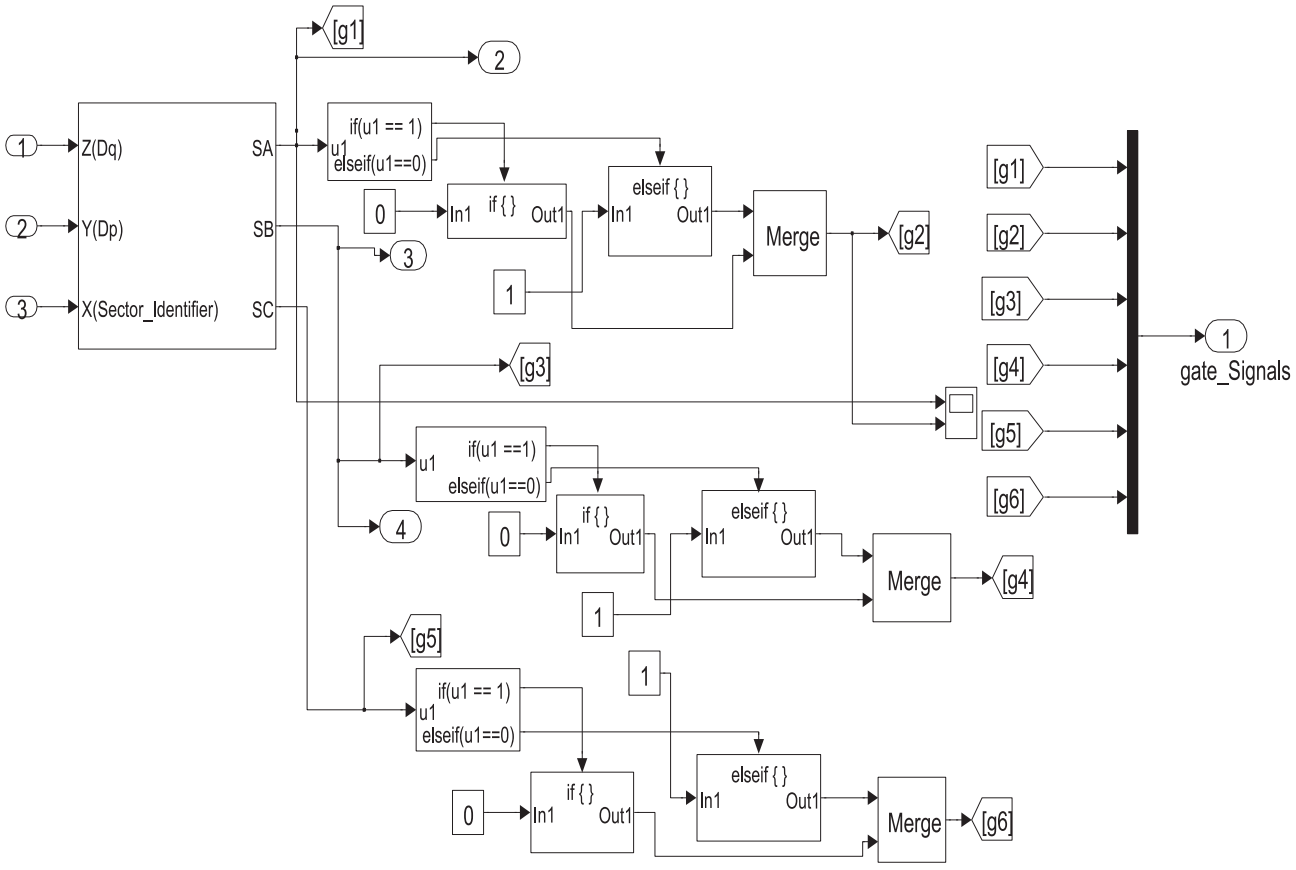

Figure A.4 Gate Signals for three phase Rectifier